Summary

Drilling with a limited operational mud margin through karstified carbonate formations, consisting of fractures and cavities with a floater offshore, can potentially lead to lost circulation and gas influx. Conventional well control procedures can be inadequate in resolving these challenges. To reduce or avoid non-productive time, the unconventional drilling and contingency method called controlled mud level drilling (CML) and controlled mud cap drilling (CMCD) can be implemented.

If the well experiences total losses in a karstified formation, the drilled cuttings along with the drilling fluid will be lost to the formation. When applying controlled mud cap drilling (CMCD) to a total loss situation, the influx gas is prevented from migrating to the surface, by a continuous injection of mud cap fluid into the wellbore annulus from a top-fill pump. The mud injection is achieved by keeping the downward velocity of the mud cap fluid greater than the estimated gas migration velocity. The gas migration velocity is an important parameter to have a good and precise estimate of, to maintain proper well control. Estimating the gas migration velocity has been the main focus of this Master's thesis.

Several authors have studied the phenomena of gas migration velocity under ambient surface pressures in stagnant liquid columns with water, which is a function of the terminal rise velocity. Few have made correlations with respect to the effect of pressure level and the presence of viscous fluid. Downhole in a well, the conditions are characterized by high pressures, so the current correlations based on ambient conditions might be inadequate.

The experiments have been performed by injecting Nitrogen gas into a cylinder containing a stagnant liquid column. The elapsed time it took the gas bubbles to reach the top of the cylinder has been determined visually by using frame-by-frame imaging analysis, and the corresponding gas migration velocity has been calculated. The experiments have been performed with three different test liquids with different viscosity levels; distilled water at 0.79 cP, 67wt% glycerol-water at 12.3 cP and 75wt% glycerol-water at 21.5 cP, to investigate the effect of different viscosity levels on the gas migration velocity for gas bubbles. The experiments have also been performed for pressure regimes ranging from 10-60 $barg$. 60 $barg$ was the pressure limitation of the set-up. The Nitrogen gas has been continuously fed into the bottom of the column at gas volume rates of 20 ml/min and 60 ml/min.

Results from the experiments showed that the viscosity level of the liquid has a large impact on the gas migration velocity. An increase in liquid viscosity level led to a significant reduction of the gas migration velocity compared to distilled water. For a pressure of 15 $barg$ for bubbles with a diameter of 1.49 mm, the gas migration velocity vary from 0.30 m/s for distilled water at 0.79 cP, down to 0.074 m/s for the 67 wt% glycerol-water solution with a viscosity of 12.3 cP and down to 0.042 m/s for the 75 wt% glycerol-water solution with a viscosity of 21.5 cP.

The gas migration velocity obtained from the experiment tends to decrease for all three test liquids for increasing pressure levels. The greatest reduction in gas migration velocity due to pressure level increase was obtained for the experiments performed with distilled water. The velocity for two different bubble sizes in distilled water did also decrease for increasing operating pressures above 30 $barg$. The gas migration velocity was reduced from 0.34 m/s to 0.26 m/s for pressures ranging from 0-60 $barg$ for bubbles with diameter of 1.86 mm.

The gas migration velocity obtained from the experiments with distilled water deviated some from the correlations from the reviewed literature. The terminal rise velocity presented by Lin et al. (1998) correlated fairly well with the gas migration velocity obtained from the experiments with the viscous liquids. By adding 0.024 m/s as a constant to the correlation, the correlation overlaps with the gas migration velocity from the experiments.

Future recommended work on the high-pressure transparent cell includes upgrading the setup so that the experiments can be performed with higher pressure regimes. Future experiments should include test liquids with properties which are more similar to the properties of drilling fluid. The experiments could also be performed with a pipe present in the cylinder to simulate the presence of a drill pipe. If this pipe could rotate, then the effect of rotation on the gas migration velocity could be investigated.

Sammendrag

Boring med begrenset operativ slam-margin gjennom karstifiserte karbonatformasjoner som består av sprekker og hulrom fra en flyter offshore, kan potensielt føre til tapt sirkulasjon og gassinnstrømning. Konvensjonelle brønnkontroll prosedyrer kan være utilstrekkelig til å løse disse utfordringene. For å redusere eller unngå ikke-produktiv tid, kan ukonvensjonelle bore- og beredsskapsmetoder som "controlled mud level drilling" (CML) og "controlled mud cap drilling" (CMCD) implementeres.

Dersom brønnen opplever totale tap under boring av en karstifisert formasjon innebærer det at alt av borevæske og borekaks tapes til sprekker og hulrom i formasjonen. Ved anvending av CMCD i en total tapssituasjon med gassinnstrømning, vil gassen bli forhindret fra å migrere til toppen av brønnen ved kontinuerlig injeksjon av viskøst slam inn i ringrommet fra en pumpe på overflaten. Injeksjonen av slam oppnås ved å holde nedadgående hastighet av viskøst slam høgere enn den estimerte migrasjonshastigheten til gass. Migrasjonshastigheten til gass er en viktig parameter for å opprettholde brønnkontroll og et godt og presist estimat av denne er derfor viktig. Dette har vært hovedfokus i denne masteroppgaven.

Flere forfattere har studert migrasjonshastighet til gass i stillestående vannkolonner under atmosfæriske forhold. I slike tilfeller er migrasjonshastigheten kun en funksjon av den terminale stigehastigheten til gassen. Få har kommet med korrelasjoner hvor effekten av trykk og viskøse væsker er tatt hensyn til. Betingelsene i borehullet er preget av høye trykk, slik at dagens korrelasjoner basert på atmosfæriske forhold kan være utilstrekkelige.

Forsøk har blitt utført ved å injisere nitrogengass inn i bunnen av en gjennomsiktig sylinder som inneholder en stillestående væske. Den tiden det tar gassboblene å nå toppen av sylinderen er bestemt visuelt ved å bruke bildeanalyse, og den tilsvarende stigehastigheten er beregnet. Forsøkene har blitt utført med tre forskjellige testvæsker med forskjellige viskositetsnivå; destillert vann med viskøsitet på 0.79 cP, 67 wt% glycerol-vann løsning med viskøsitet på 12.3 cP og 75 wt% glycerol-vann løsning med viskøsitet på 21.5 cP, for å undersøke effekten av forskjellige viskositetsnivåer på migrasjonshastigheten til en gassboble. Forsøkene har også blitt utført med trykkregimer som varierer fra 10-60 $barg$. 60 $barg$ var trykkbegrensningen på oppsettet. Nitrogengass har kontinuerlig blitt matet inn i bunnen av kolonnen ved gassvolum på 20 ml/min og 60 ml/min.

Resultater fra forsøkene viste at viskositetsnivået på væsken har stor innvirkning på migrasjonshastigheten til gassbobler. En økning i viskositet på testvæsken førte til en signifikant reduksjon i migrasjonshastighet sammenlignet med destillert vann. For et trykk på 15 $barg$ varierer migrasjonshastigheten til gassbobler med diameter på 1.49 mm fra 0.30 m/s for destillert vann, 0.074 m/s for 67 wt% glycerol-vann løsning på 12.3 cP til 0.042 m/s for 75 wt% glycerol-vann løsning med viskositet på 21.5 cP.

Migrasjonshastigheten til gassbobler fra forsøkene har en tendens til å reduseres for alle tre testvæsker for et økende trykkregime. Den største reduksjonen i hastighet som resultat av trykkøkning ble oppnådd for gassboblene i forsøkene utført med destillert vann. Hastigheten for to forskjellige boblestørrelser i destillert vann ble redusert for trykk over 30 $barg$. Migrasjonshastigheten til gassbobler med en diameter på 1.86 mm ble redusert fra 0.34 m/s til 0.26 m/s for økende trykk fra 0-60 $barg$.

Resultatene fra forsøkene med destillert vann avviker fra korrelasjonene fra den gjennomgåtte litteraturen. Den terminale stigehastigheten presentert av Lin et al. (1998) korrelerte nokså godt med migrasjonshastigheten til gassbobler fra forsøkene med de viskøse væskene. Ved å legge til 0.024 m/s til korrelasjonen, overlapper den justerte korrelasjonen med gass-migrasjonshastigheten fra forsøkene.

Fremtidig anbefalte forsøk med den gjennomsiktige sylinderen inkluderer oppgradering av oppsettet slik at forsøkene kan utføres for høyere trykkregimer enn 60 $barg$. Fremtidige eksperimenter bør inkludere testvæsker med egenskaper som ligner borefluidets egenskaper. Forsøkene kan også utføres med et rør tilstede i sylinderen for å simulere tilstedeværelsen av et borerør. Dersom røret kan roteres, kan effekten av rotasjon på gass-migrasjonshastigheten undersøkes.

Acknowledgement

Tonje Garpestad Tønnessen
Trondheim, 11.06.2019

Table of Contents

List of Tables

List of Figures

Nomenclature

Symbols

ρ	Density	$[\frac{kg}{m^3}]$
σ	Surface tension	$[\frac{N}{m}]$
P	Gauge pressure	$[barg]$
P	Absolute pressure	$[bara]$
T_K	Temperature	$[K]$
T_C	Temperature	$[°C]$
n	Mole	$[Mole]$
V	Volume	$[m^3]$
Q	Volumetric flow rate	$[\frac{m^3}{min}]$
g	Gravity	$[\frac{m}{s^2}]$
r	Radius of bubble-cap	$[m]$
D	Pipe diameter	[m]
M	Molar mass	$[\frac{g}{mole}]$
ID	Inner diameter	[mm]
OD	Outer diameter	[mm]
$\bar{\epsilon}$	Void fraction	
C_0	Constant	
C_D	Drag coefficient	
R_b	Radius of curvature	$[m]$
R	Boltzmann constant	[J/mol K]

t	Time	$[min]$
θ	Diameter ratio	
d	Bubble diameter	[m]
k	Diffusion constant	
A	Filter exposure area	[m^2]
H	Henry's constant	$[\text{g}\frac{}{kgbar}]$
$\dot{V}$	Volume flow	[ml/min]
$\dot{m}$	Mass flow	[g/min]
C_ρ	Density correction factor	
v	Velocity	$[\frac{m}{s}]$
Re	Reynolds number	
Eo	Eotvas number	
Mo	Mortons number	
Fr	Froude number	
μ	Dynamic viscosity	[Pas]

Subscripts

$'$	Dimensionless	
b	Bubble	
D	Drag	
d	Droplet	
DP	Drill pipe	
e	Equivalent	
$frac$	Fracture	
g	Gas	
$hole$	Hole	
inj	Injection	
l	Liquid	

$lower$	Lower line
m	Mixture
mud	Mud column
$pore$	Pore fluid
t	Terminal
$upper$	Upper line
w	Wake

Abbreviations

BHP	Bottom hole pressure
BOP	Blow out preventer
BPR	Back pressure regulator
$CMCD$	Controlled mud cap drilling
CML	Controlled mud level
DPT	Differential pressure transmitter
ECD	Equivalent circulation density
GOR	Gas oil ratio
gpm	Gallons per minute
$HPHT$	High pressure high temperature
$LAMCD$	Light annular mud cap drilling
$LARS$	Launch and recovery system
LCM	Lost circulation material
lpm	Liters per minute
MCD	Mud cap drilling
MPD	Managed pressured drilling
MRJ	Modified riser joint
MRL	Mud return line
MWD	Measurement while drilling
$NTNU$	Norwegian University of Science and Technology

OBM	Oil-based mud
RCD	Rotating control device
RIV	Riser isolation valve
SD	Standard deviation
SF	Safety factor
sg	Specific gravity
$SICP$	Shut-in casing pressure
$SIDPP$	Shut-in drill pipe pressure
SPM	Subsea pump module
WBM	Water-based mud

1 | Introduction

1.1 Motivation

A gas kick is an unintentional influx of gas due to a higher formation pressure than the bottom hole well pressure. Gas entering the well will start to migrate up towards the surface due to the density and pressure differences in the well and can evolve into an uncontrolled situation if not managed in a controlled manner.

The velocity that the rising gas has is an important parameter to estimate when exerting well control. Well control procedures in place are utilized to minimize the problems related to unwanted formation influx and to restore control of the well. This has a high priority for the operator companies. This could include shut-in of the well and by controlled methods, circulating out the formation influx. If a well experiences a gas influx, this can often be related to lost circulation. Drilling operations performed in formations where there is a high risk of lost circulation requires a well-planned contingency method for handling this situation. Often can unconventional drilling methods be more favourable for these kinds of drilling operations. This includes unconventional drilling methods like managed pressure drilling, where the bottomhole pressure in principle is controlled and managed at the surface to balance the formation pore pressure and formation fracture pressure at the bottom of the well. In some extreme cases with very weak formation, taking the return of drilled cuttings to surface can be a challenge without risking gas influx. Methods have been developed to maintain control of the well even if the drilled cuttings do not return to the surface but are bullheaded back into the formation. The rate of bullheading needs to be adjusted to above the potential gas migration velocity to also maintain well control under such a situation.

The well control method of bullheading can be favourable when the well experiences lost circulation and gas influx during an unconventional drilling operation. Bullheading involves pumping down mud in the annulus at a pump rate which is sufficient to overcome the gas migration rate and pushes the gas influx back into the formation. By having a precise estimate of the gas migration velocity, the pump volume that is required to bullhead the gas down into the formation can be adjusted accordingly. Bullheading can be a contingency method for unconventional drilling methods offshore from floaters that controls the bottomhole pressure in the well by regulating the mud level in the marine riser. These unconventional drilling methods include controlled mud level drilling (CML) and controlled mud cap drilling (CMCD); two types of managed pressured drilling techniques from a floater offshore.

A focus area for operators in Norway is exploration from floaters in the Barents Sea and

utilization and production of this area if possible. Karstified carbonate formations that consist of fractures and cavities are known to be one of the geological formations that are present in the area. These formations can act as thief zones when drilled through. This means that the drilling fluid is lost to the formation, which reduces the hydrostatic column in the well. If the formation contains gas, there is a high risk that the well will experience gas influx, which potentially can result in a well control situation. Utilization of a conventional drilling method where cuttings are transported to surface in these formations involves a high risk of lost circulation and a well control situation creating an inefficient, unsafe and costly operation. The methods of CML and CMCD have already proven to be a reliable process to handle these karstified formations.

To determine the gas migration velocity under pressure and in the viscous fluids have been the main focus for my lab work in this thesis, emphasized at bubble flow with small dispersed bubbles continuously fed into a vertical transparent pipe.

1.2   Objective

This Master thesis is based on the work presented in the Project report "An Experimental Study of Gas Migration in Pressurized Fluids" by Tønnessen (2018). The theory from this Project report has also been presented in this thesis. The objective of this Master thesis has been to study how pressure and liquid viscosity can affect the gas migration velocity by experimental testing. A literature review on relevant topics will be performed in addition to the experimental testing. The literature review will be focusing on:

- Principles of gas kick

- Well control procedures including methods of shut-in and circulating out a kick

- Drilling problems related to formations containing karstified carbonates

- Utilization of controlled mud level drilling and controlled mud cap drilling

- The phenomena of gas migration velocity

Several authors have studied the phenomena of gas migration velocity under ambient surface pressures in stagnant liquid columns with water, which is a function of the terminal rise velocity. Few have made correlations with respect to the effect of pressure level and the presence of viscous fluid. Conditions downhole are characterized by high pressures, so the current correlations based on ambient conditions might be inadequate.

Experiments will be performed by injecting Nitrogen gas into the bottom of a cylinder cell containing a stagnant liquid column to simulate gas entering a well for different pressure regimes. The elapsed time it takes the gas bubbles to reach the top of the cell will be used to determine the gas migration velocity for these gas bubbles. Different test liquids will be used in the experiment to determine how liquid properties like viscosity affect the gas migration velocity. The experimental results will be compared to velocities obtained from the reviewed literature.

1.3   Working Methodology

- Chapter 1: Presents the introduction, including the motivation and objective of this thesis.

- Chapter 2: This chapter includes related background theory and literature review on gas kick, different types of well control, problems related to drilling through karstified carbonates, the unconventional drilling techniques of controlled mud level and controlled mud cap drilling and gas migration velocity.

- Chapter 3: The experimental methodology is presented in this chapter. The experiment has been performed for two different setups. Both have been illustrated and explained in this chapter along with their procedure, limitations and future improvements.

- Chapter 4: The results from the experiments with a high-pressure transparent apparatus are presented and discussed in this chapter. A comparison of the results to the terminal rise velocity calculated with correlations from the reviewed literature is also included. Recommendations for further work are discussed.

- : Chapter 5: The conclusion is given.

2 | Background and Literature Review

2.1 Gas Kick

A gas kick is a situation that can occur when unwanted gas enters the well during a drilling operation. The mud weight used to drill a well is determined based on a mud window. This window is determined and limited by the pore pressure and the fracture pressure at the depth that is being drilled.

$$P_{pore} < P_{mud} < P_{frac}$$

Since fluid tends to flow from high-pressure zones to lower pressure zones, the mud weight of the drilling fluid needs to be higher than the pressure of the pore fluid. If this is not satisfied, fluid from the formation can enter the well. It is important to ensure that the mud weight stays within the mud window limit when the well is in a static condition, but also when it is in a dynamic condition. The well is in a static condition when the liquid column in the well is stagnant. This situation occurs when making up connections. In that case, the bottom hole pressure in the well is determined by the hydrostatic column. Circulating is an example of when the well is in a dynamic condition. A dynamic condition leads to pressure losses in the system due to friction. A mud weight that is just above the pore pressure is usually chosen. When the well is being circulated the equivalent circulation density, ECD, is still below the limit for fractures in the formation to occur.

2.1.1 Causes for a Gas Kick

The fundamental principle that leads to a gas kick is that the formation pressure exceeds the hydrostatic bottom hole pressure in the well. There are several things that can cause that, and some of them are listed below:

- Insufficient mud weight

- Improper hole fill-up

- Swab pressure

- Lost Circulation

If the estimate of the formation pressure is wrong, the mud weight that has been chosen can be either too high or too low.

The hydrostatic pressure might be reduced due to insufficient mud volume in the well. When the drill string is pulled out of the hole, the mud level drops. To maintain the hydrostatic pressure, the space that is now available due to the removal of steel needs to be filled with more mud. If the mud volume that is supplied to the well is insufficient, an underbalanced situation occurs, which can result in a kick.

The hydrostatic pressure can also be reduced due to swabbing. Swab pressures occur when the drill string is pulled out of the hole and reduces the effective hydrostatic pressure at the bottom of the well. The swab pressure is a function of the pipe pulling speed, mud viscosity, hole configuration and balled equipment. Balled equipment is when formation rock attaches to the pipe or the bottom hole assembly and makes the outer diameter of the hole larger, which increases the effect of swabbing (Waldeland, 2016).

When drilling through formations with fractures, mud from the well can enter the fractures and lost circulation occurs. This reduces the height of the mud column in the well and the corresponding bottom hole pressure, making it possible for formation fluid to enter the well.

2.1.2   Gas Kick in an Open Well

If the hydrostatic bottom hole pressure in the well for some reason is lower than the formation pressure, formation fluid such as gas will enter into the well. The amount of formation fluid entering the well is dependent on the hydrostatic column in the well. When the hydrostatic pressure balances the formation pressure the influx will stop. The bottom hole pressure is higher than the surface pressure due to the hydrostatic column of mud and this results in gas migrating to the surface. The well is assumed to be open, which will be the case before any well control actions are performed. Gas starts to migrate up towards the surface, and as Boyle's law states, when the pressure is reduced, the gas will expand. Assuming that the temperature difference between surface and bottom hole is constant, Boyle's law states that the product of pressure and volume is constant for a given mass of confined gas. The relationship is given in Equation 2.1.

$$P_1 V_1 = P_2 V_2 \qquad\qquad (2.1)$$

The further up the gas migrates, the more it expands. An illustration of this situation is presented in Figure 2.1. When it is halfway to the top, the volume of the gas is double what it was when entering the well. The more the gas expands, the more drilling fluid will be pushed out of the well. This means that the hydrostatic pressure is being reduced and can result in more gas flowing into the well.

(a) Gas entering the well.   (b) Gas expanding when moving upwards.

(c) Gas has reached the BOP.
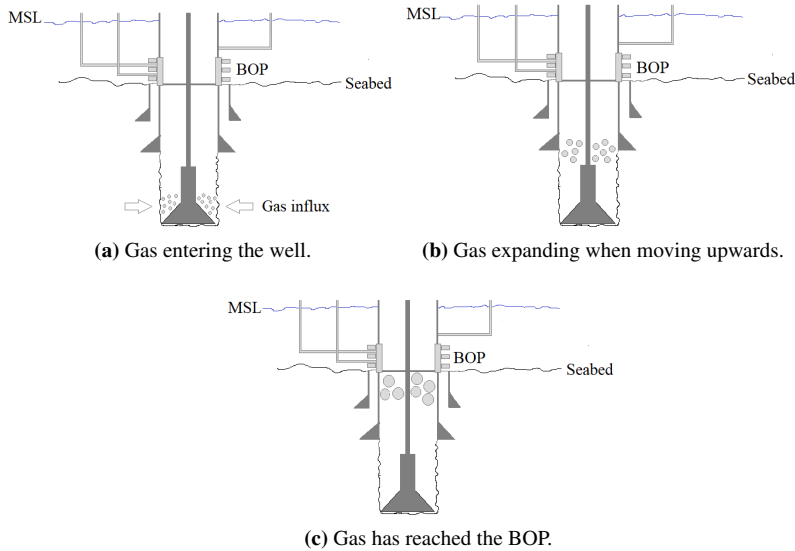
Figure 2.1: Gas migration in an open well.

2.1.3 Gas Kick in a Closed Well

Well control procedures need to be performed when realizing that the well is subjected to a gas kick. This includes a shut-in of the well by closing the BOP. Gas will still be flowing into the well until the formation pressure and bottom hole pressure have equalized. The pressure required at the surface to shut-in the well (SIDPP) is equal to the formation pressure minus the hydrostatic pressure the mud column exerts on the bottom of the well as given by Equation 2.2. This is called pressure build-up. Gas will now start migrating to the surface due to density differences between the fluids in the well. Since the well is closed, the gas can not expand and the volume of gas remains constant. The pressure will increase as gas rises and result in a higher shut-in pressure when reaching the surface. The high surface pressure that gas migration adds in addition to the hydrostatic pressure the drilling fluid exerts on the bottom of the well, can fracture the formation or burst the casing. The casing should be designed and tested to handle this pressure.

$$P_{formation} = P_{shutin@surface} + P_{mudcolumn} = SIDPP + \rho_{mud}gh \qquad (2.2)$$

2.1.4 Gas Kick in Different Drilling Fluids

Drilling fluids are normally water-based or oil-based. Oil-based mud is more compressible than water-based mud, which means that the volume of fluid can change more when exposed to higher pressures. The volume of influx downhole can therefore be greater than expected at the surface when using oil-based mud.

Oil-based mud can be contaminated by the gas during drilling due to the solubility of gas into the mud. For higher specific gravity, the gas solubility increases for intermediate pressures as presented by Patrick Leon (1985). The viscosity of the oil-based mud is reduced when gas is dissolved into it. This is due to a reduction of shear stresses as a result of the dissolved gas (Torsvik et al., 2016). The dissolved gas also has an effect on the density. According to results by O'Bryan et al. (1987), the density of the mud decreases when gas dissolves into oil-based mud.

Gas that is dissolved into oil-based mud does not migrate but can reach the surface with the circulated mud. When the mud travels towards the surface, the gas can flash out due to the reduced pressure and have a large expansion (Waldeland, 2016). Gas does not dissolve in water-based mud and will start migrating towards the surface as free gas when entering a well drilled with water-based mud.

2.1.5   Gas Solubility in Oil-Based Mud

Gas hardly dissolves in water-based muds, but travel to the surface as free gas (Skogestad et al., 2017). Gas can, on the other hand, dissolve in oil-based muds depending on the gas loading capacity of the drilling fluid. Oil-based muds are often used to drill deeper sections on the Norwegian Continental Shelf due to better lubrication, shale inhibition and high-pressure high-temperature (HPHT) tolerance (Skogestad et al., 2017). Dissolved gas will boil out of the drilling fluid mixture when the pressure is reduced below the bubble point pressure. If the well pressure at all depths is above the bubble point pressure, the magnitude of the pressure is limited due to no free gas (Alcantara Santos et al., 2017). Until the point where gas starts to boil out of the mixture, the gas kick may go undetected. If the boiling starts high up in the well, there may be little time to react and start shut-in procedures (Skogestad et al., 2017).

2.1.5.1   Phase Envelopes

A phase diagram can be used for the purpose to determine for what combinations of pressure and temperature a mixture of hydrocarbon and water will exist as a pure liquid, a gas mixture or as a two-phase. Figure 2.2 is an example of a phase diagram for a refined base oil and methane (Linga et al., 2017). The two-phase region is enveloped by a bubble point curve and a dew point curve, which is connected at the critical point. The mixture is a liquid for combinations of pressure and temperature that lies above the bubble point curve. For combinations of pressure and temperature that lies below the dew point curve, the mixture will exist as a gas. Different combinations of pressure and temperature inside the two-phase region result in different relative fractions of gas and liquid. The dense phase region lies above the critical point.
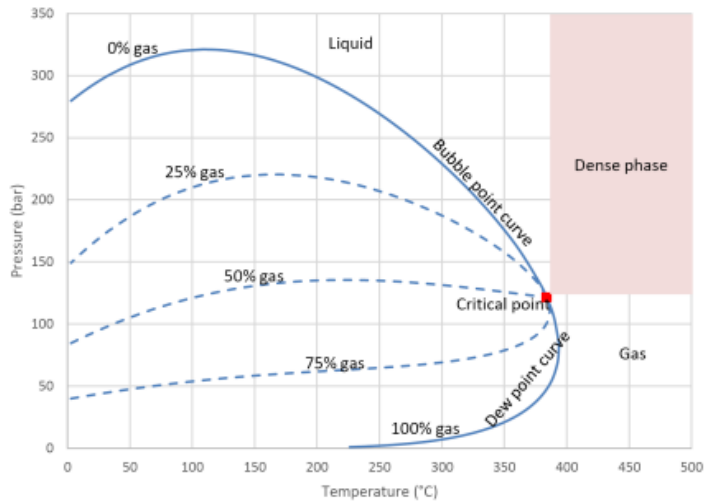
Figure 2.2: "Phase diagram for methane - refined base oil" (Linga et al., 2017).

2.1.5.2   Gas Loading Capacity

Different oil-based drilling fluids have different gas loading capacity. The maximum load-ing capability of gas in a drilling fluid at a given temperature and pressure will depend on the phase distribution for that particular mixture. In addition to the phase envelope, the gas loading is also a function of the residence time of the drilling fluid in the influx zone and the filter cake performance (Skogestad et al., 2017).

Knowledge of the interaction between natural gas and drilling fluid is important to reduce the severity of potential gas kick situations. Gas influx can occur due to an underbalanced situation in the well, but it can also occur when the well is in overbalance and left without circulation for a period of time. In the latter situation, the drilling fluid is likely to have a high gas loading capacity. The drilling fluid is exposed to the influx gas when the well is left undisturbed for a time period by diffusivity through the mud invaded zone and the filter cake (Bradley et al., 2002). The more shallow the fluid invasion zone is, the greater the gas diffusion rate from the formation into the well will be.

If a well is to be left undisturbed for a period of time, it would be beneficial to have a deep fluid invasion zone, which corresponds to a slower diffusion rate of gas into the wellbore. This means that an effectively functioning drilling fluid filter cake would give a greater gas diffusion into the well.

Fluid invasion of drilling mud into the formation is assumed to consist of pure base oil (Bradley et al., 2002). The pure base oil can consist of invert emulsions, where water is the internal phase and oil is the continuous phase. These water droplets will plug pore throats at the interface between the well and the formation. If the plugging of the pore

throats are inadequate, fluid invasion of drilling fluid into the formation will continue due to the overbalance. This process will go on until a filter cake is made by particles and polymers in the drilling mud and the mud invasion can be reduced. This would result in a deeper mud invasion zone, corresponding to a slower diffusion rate of gas into the well.

The driving mechanism for diffusion of gas through the fluid layer created by the mud invasion into the well is the partial pressure difference between the methane in the formation and the methane in the wellbore. The diffusion of methane into the well can continue until the partial pressure difference has equalized (Bradley et al., 2002).

Linga et al. (2016) investigate two types of oil-based muds (OBM), one where the base-oil is normal mineral oil and the other has linear paraffin as its base-oil. Both drilling fluids share the same volumetric fraction of base oil and the density has been adjusted with barite to the same value. Gas solubility is given by mass dissolved per mass unit of the base of the liquid. Figure 2.3a and 2.3b show the gas solubility characteristics for the two base oils and the corresponding drilling fluids. The results show that the gas solubility is more or less identical for the base oil and the corresponding drilling fluid, hence the gas loading capacity of a drilling fluid is dominated by the base oil that the drilling fluid mixture contains. Figure 2.3a and 2.3b also show that as long as the trend is linear, the temperature does not affect the gas loading capacity. Both base oils have a gas solubility that is linear up to a certain pressure, which corresponds to the transition from the liquid phase region to the dense phase region. The gas solubility capacity is infinite in the dense phase region.
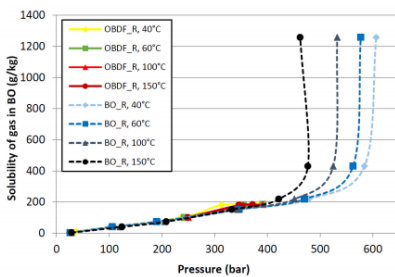
(a) "Gas solubility characteristics for the refined "normal" mineral base oil and the corresponding drilling fluid. Data recalculated from Torsvik et al. (2016)" Linga et al. (2016).
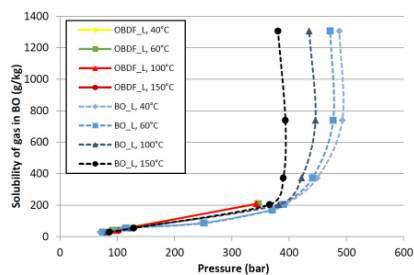
(b) "Gas solubility characteristics for the linear paraffin base oil and the corresponding drilling fluid. Data recalculated from Torsvik et al. (2016)" Linga et al. (2016).

Both bases have a similar maximum gas loading capacity that follows Henry's law up to a given pressure. Henry's law is a linear relation between maximum gas loading capacity in the liquid vs pressure and is given by Equation 2.3. The linear paraffin base oil reaches the dense phase at a lower pressure than the normal mineral base oil, hence the linear base oil can absorb much more gas compared to the normal base oil. The gas loading for the dense phase region is given by Equation 2.4 and is a time linear relation, which is infinite.

$$m_g = HPm_l \left[1 - e^{-\frac{Ak}{m_l}t} \right] \tag{2.3}$$

where H is Henry's constant of 0.414 $\frac{g}{kgbar}$, P is pressure in $bara$, t is the exposure time in seconds, m_g and m_l is the gas mass loading and the drilling fluid liquid mass loading for the gas influx area, respectively. A is the exposed area in m^2 where the gas influx occurs and k is the diffusion constant related to the filter cake characteristics (Linga et al., 2016).

$$m_g = AkHPt \tag{2.4}$$

When the maximum gas loading capacity of the drilling fluid is reached after a continuous gas influx, a distinct expansion of the free gas in the well will occur. This distinct volume expansion response does not occur when operating in the dense phase, which means that an influx of natural gas can be masked if the drilling fluid is operating in the dense phase region (Skogestad et al., 2017).

Density sensitivity vs pressure increases when reaching the two-phase region at the bubble curve. The sensitivity increases for lower gas-oil ratios (GOR). When the maximum loading capacity has been reached, free gas in equilibrium with liquid will appear. A mixture that has reached the dense phase for a given pressure will remain in this phase even if the GOR is increased. This means that a mixture in the dense phase can accumulate an unlimited amount of gas (Linga et al., 2017).

Figure 2.3 shows a phase envelope for the refined mineral base oil and methane together with a brown line that corresponds to the pressure versus temperature profile of a given well. The intersections of the bubble point curves for different GOR and the P/T profile indicates the well depth where free gas will start boiling out of the two-phase mixture. According to Figure 2.3, gas will start boiling out deeper in the well for higher GOR mixtures. For a GOR of 480, gas will start boiling out at a pressure of 500 bar and a temperature of 130 °C. This data can be compared to a pressure vs depth table, so the actual well depth in which this occurs can be obtained.
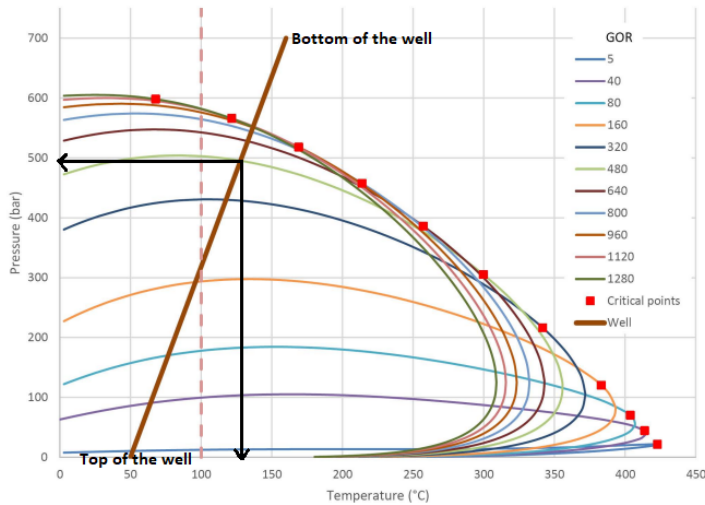
Figure 2.3: Phase diagram for methane and refined mineral base oil. The brown curve represents pressure and temperature data vs depth for a given well (Linga et al., 2017).

It is important to have knowledge about the gas loading capacity of the drilling fluid that will be used in operation and for what operating conditions the drilling fluid enters the dense phase region prior to operation. This information makes it possible to avoid moving into the dense phase operating conditions and thereby limit the amount of influx gas entering the well if it is left without circulation for some time. If possible, the operational procedures should be adjusted based on what kind of oil-based mud that will be used in the operation (Linga et al., 2016).

2.2   Well Control

Well control procedures are utilized to minimize problems related to formation influx and to restore control of the well. It is important to detect a kick as early as possible to reduce consequences and avoid a dangerous situation.

2.2.1   Indicators of a Gas Kick

Some indicators of a gas kick are presented below: (International, 2015) and (Sørskår, 1984)

- Pit volume increase

- Return flow rate increase

- Flowing well with pumps off

- Variations in pump pressure

- Improper hole fill up during trips

- Drilling break

- Gas detected in mud on the surface

If the volume of return mud is greater than the volume of mud pumped into the well, a gain in the pit tank is experienced. This means that the gas influx downhole displaces an equal volume of mud which can be seen as a pit gain on the surface. A kick might be detected earlier if the rate of return is constantly measured. An increase in return flow rate corresponds to an influx downhole.

Another good indicator of a kick is if the well continues to flow when the pumps are turned off. If the pump pressure increases it means that there is some sort of obstacle in the well working against the flow or an increase in viscosity. Some types of influx can flocculate the drilling mud causing an increase in viscosity and also a resistance to flow. If the pump pressure is reduced during drilling it can indicate that a low-density fluid has entered the well annulus and replaced the mud, resulting in a U-tube-effect.

When pulling out the drill string, more mud needs to be added to avoid a drop in the mud level. If the calculated amount of fill-in mud is not entering the well, it can be an indicator of a gas kick.

The rate of penetration is a function of the pressure difference between the formation and the hydrostatic pressure in the well. A large pressure difference corresponds to a low ROP. If all other parameters are held constant and the well suddenly experiences an increase in the drilling rate, it can indicate that a new formation has been entered with a different pressure regime. This sudden increase in ROP is known as a drilling break. To make sure that the new formation does not kick, a flow check should be performed. In general, if there is a sign of influx, a flow check should be performed to determine if it is a false alarm or a kick in progress.

2.2.1.1   Flow Check

A flow check includes raising the top drive to a predetermined height and space out, stop rotating the drill string, turning off the pumps, wait for the well to stabilize and if it is possible, observe the annulus. It is a strong indication of a kick if the well continues to flow when there is no circulation of drilling fluid. If a kick is confirmed after performing a flow check, an additional influx has been allowed into the well while performing the flow check. The well must be closed immediately if a kick is detected and procedures to regain well control has to be implemented.

2.2.2   Methods of Shut-In

There are two principal methods of executing a shut-in. These are called hard shut-in and soft shut-in. The fastest way to shut-in the well is by using the hard shut-in, but this method also potentially includes a fluid hammer effect. The difference in methods is that the soft shut-in leaves the choke-line open during the closure of the BOP. After the BOP has been shut-in, the choke manifold is closed, resulting in a completely closed in well. According to International Association of Drilling Contractors (2015), the pressure pulse generated by the hard shut-in is not that much larger than the one generated by the soft shut-in. The kick needs to be very large to develop a problematic hammer pressure. The pressure pulse that occurs will be exerted at the BOP and have a minimal effect on the critical point in the well, which normally is the casing shoe.

The driller can choose which shut-in approach to use, either closing the annular preventer or the BOP pipe ram. When shutting the BOP ram, the driller needs to make sure that the ram is not closing in on a tool joint and that the space out is correct. If not, this could damage the primary barrier. Closing the BOP pipe ram takes less time than closing the annular preventer, but there are advantages to using either approach. Once the BOP is closed, the choke manifold has to be lined up properly and stay closed. The two shut-in pressures need to be recorded periodically. This includes the shut-in drill pipe pressure (SIDPP), shut-in casing pressure (SICP) and shut-in casing pressure on both choke and kill lines. The monitoring of the mud pit is also necessary. Figure 2.4a illustrates how a gas influx into the well affects the volume in the trip tank. In Figure 2.4b the BOP has been closed as a reaction to the measured gain in the trip tank indicating that gas has entered the well. After the well is shut-in, the gas contamination needs to be removed. There are different methods for maintaining well control and circulating out the gas kick.

(a) Gas influx situation with mud gain in the trip tank.   **(b)** Gas kick detected - BOP is closed.
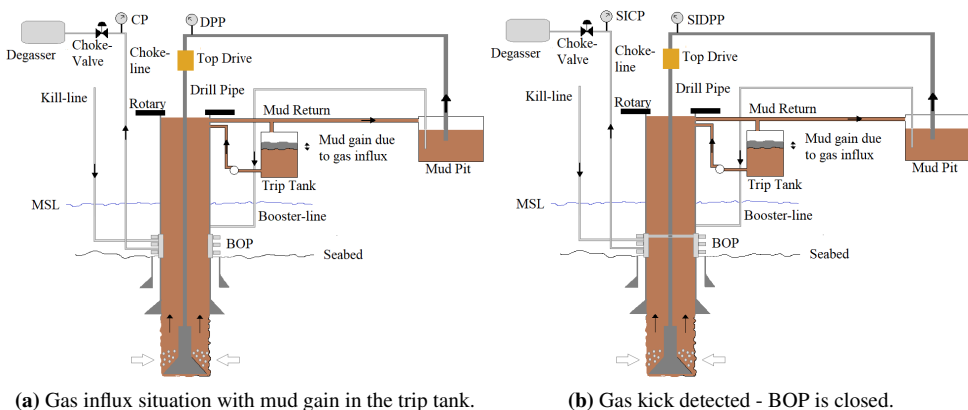
Figure 2.4: Well responding to a gas kick.

2.2.3   Methods for Circulating Out a Gas Kick

2.2.3.1   Drillers Method

Drillers method is a two circulations method. When the gas has reached the closed BOP as illustrated in Figure 2.5a, the present mud in mud pits is pumped down the drill pipe to displace the kick volume. The influx volume is bled out through the choke-line into the poor boy degasser by adjusting the choke-valve. This is performed with constant drill pipe pressure and is shown in Figure 2.5b. When the whole kick volume has been removed from the well, the second circulation starts. Kill mud is pumped down the drill string while following a drill pipe pressure schedule, illustrated in Figure 2.5c. This drill pipe pressure is held constant while the kill mud is circulated to the surface. Drillers method has the advantage of allowing more time to get representative measurements of shut-in pressures and calculate the required kill weight, by removing the influx with the present mud (International Association of Drilling Contractors, 2015).

(a) Gas influx situation with mud gain in trip tank.

(b) Gas kick detected - BOP is closed.

(c) Gas kick detected - BOP is closed.
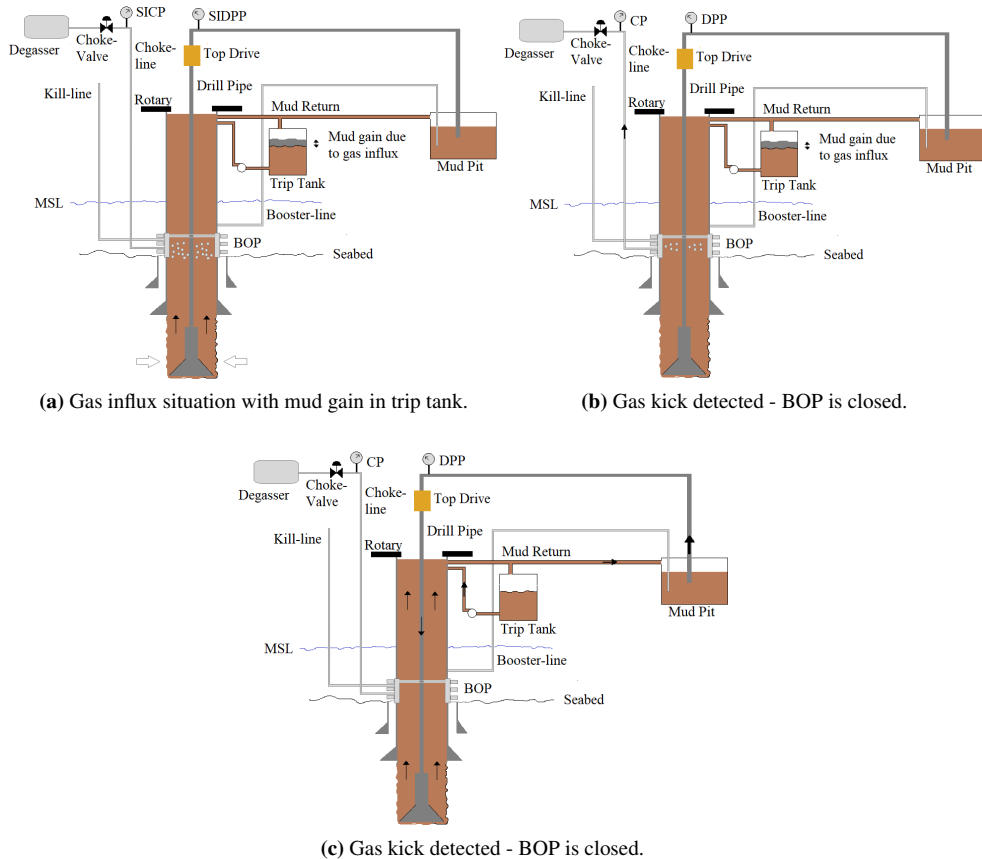
Figure 2.5: Drillers method of circulating out a kick.

2.2.3.2 Wait and Weight

The other conventional method is called Wait and Weight, and this method only requires a single circulation. After the well is closed, kill mud is directly pumped into the drill string to displace the gas contamination and fill up the well, also following a drill pipe pressure schedule. When the mud enters the annulus, the circulating drill pipe pressure is held constant while the kick fluid is displaced to surface. This method needs immediate access to kill mud. The surface pressure is less for this method compared to the driller's method.

2.2.3.3 Volumetric Method

If the drill string is out of the well or for some reason normal circulation from the bottom of the well is not possible, the volumetric method can be a solution to regain well control if a gas influx occurs. The principle behind the method is that the influx volume of gas is allowed to expand as it travels toward the surface at the same time as a given volume of mud is let out from the top to reduce the bottom hole pressure (Halle, 2001).

Gas influx enters the well and the well is shut-in. The gas will now start to migrate upwards without being able to expand. This causes the well pressure to increase. The pressure increase can be read off at the surface. The choke valve is opened and a fixed volume of mud is let out, which allows the gas to expand. The volume of mud that is let out corresponds to a loss of hydrostatic pressure in the well that is necessary to reduce the bottom hole pressure to the initial one (Hauge, 2013). The well is closed in again, and the pressure will continue to increase as the gas influx moves towards the surface. After a given pressure build-up, the choke valve will open again and the procedure is repeated. This process will continue until the entire gas volume has reached the surface and the pressure build-up will stop. The well is now stable. Mud is pumped through the drill string or kill-line to displace the gas. When the whole influx volume has been displaced out of the well, the drill string is lowered to the bottom and the well can retain overbalance by circulating heavy kill mud.

2.2.3.4 Bullheading

Another way of getting rid of the gas contamination is by using bullheading. This method is a good alternative if the expected surface pressure during a conventional circulation, as the methods mentioned above, is expected to be very high. Mud is pumped down the annulus at a pump rate sufficient to overcome the gas migration velocity and pushes the influx back into the formation.

2.3   Problems Related to Drilling Karstified Carbonates in the Barents Sea

Drilling operations in karstified carbonates involves a high safety risk due to a higher probability of lost circulation, which weakens the primary barrier. Awareness has been raised to these kinds of drilling operations due to enhanced exploration in carbon-formations in the Barents Sea. The carbon-dominated formations in the Barents Sea are from the geological period named Permian (Acona, 2017).

This chapter elaborates why karstification can be a problem while drilling, what mitigating actions operator companies need to take and how the unconventional drilling and contingency method of CML and CMCD can be used to successfully drill these wells.

2.3.1   Karstified Carbonates

Carbonates are a common term for rocks where the main component is the carbonate ion, CO_3^{-2}. The most common carbonate minerals in Norway is calcite, dolomite and magnetite (NGU, 2015). The character and properties of carbon deposits are originally affected by the depositional environment and the palaeogeography. If the deposits have been subjected to erosion, karstification, hydrothermal impact and/or dolomitization, it can result in changes in character and properties making it difficult to declare/decide the original ones (Acona, 2017).

The technical report by Acona (2017) explains karstification and cave formation as a degradation phenomenon where freshwater flows along weakness zones, cracks and faults and gradually expand the cracks and cavities. For karstification to occur the formation must have been above sea level or groundwater level. The rate of this process depends on the mineralogy and the solubility of the rock. Evaporite minerals are more soluble than carbonates, so the process of karstification will occur faster for these minerals.

Figure 2.6: "Network of cracks and root marks in the epikarst, source: M.Bakalowicz" (Encyclopedia, 2019).

The Loppa High in the southern Barents Sea consists of karstified carbonates in the Ørn and Falk formations. During late Permian, the Loppa High have been raised above sea level for 10 million years and subjected to both erosion and chemical dissolution of minerals (karstification) before beeing buried again in middle Triassic. Similar processes apply for the Utsira High in the North Sea and the northern part of "Nordlandsryggen" in the Norwegian Sea (Acona, 2017). In the structures Alta, Neiden and Børselv on the Loppa High, comprehensive karstification has been found from seismic mapping and well drilling. The wells have been drilled by Lundin, a Swedish operator company (Acona, 2017).

2.3.1.1   Drilling Problems

Most caves and cavities will collapse subsurface due to the weight of the overburden. Exceptions exist, which is why drilling operations in karstified carbonates can be problematic. Cracks in the overburden will be created when open caves in the layers below collapse, resulting in an additional risk of lost circulation when drilling through the overlaying rock layers. Since the porosity and permeability are often preserved between collapse breccia and cracks, the amount of lost circulation can be large (Acona, 2017).

When drilling through these karsts or open caves, the drill string may fall freely through the void space continued by a rapid loss of mud. The amount of lost circulation depends on the degree of interconnection between caves and channels.

2.3.1.2   Risk Assessment and Contingency Measures

The most important tool for detecting and identifying karstified formations and potential thief zones are 3D seismic with optimal acquisition and processing parameters. By calibrating the seismic observations against petrophysical logs or cores from neighbouring wells, a more accurate picture of the subsurface and the karstified formation can be made, resulting in safer well operations (Acona, 2017). However, due to limitations with seismic the resolution, only large karst features are able to be observed on seismic.

Some drilling fluid will be lost to the formation during drilling until a filter cake has been made on the bore-hole wall. This filter cake will block the pores and stop the loss of drilling fluid. When planning wells in areas like the Loppa High where there is a high chance of karstified carbonates, the associated risk should be elaborated thoroughly. When drilling through rocks with collapsed or partly collapsed caves, the cracks will be too big for the drilling fluid to be able to make a filter-cake on the bore-hole wall (Acona, 2017). These caves or cavities can be so large and connected that lots of drilling fluid can be lost in a short period of time. If the lost circulation is not stopped early enough, it can result in an underbalanced well that can be exposed to formation influx leading to a well control situation.

The risk of lost circulation is accounted for in all types of drilling operations. Lost circulation material, LCM, is always available on the rig in case of a lost circulation situation. A

detailed plan for how to pump the LCM down the well and at what time is always updated on the rig. Additional volumes of LCM is always present on the rig or on boats nearby if large volumes of mud are suddenly lost. These measures are upgraded when drilling through karstified formations due to the risk of larger drilling fluid losses. Different types and particle sizes of LCM for both drilling fluid and cement will be present on the rig in addition to even larger volumes of LCM and drilling fluid (Acona, 2017). This leads to greater challenges with handling logistics, especially for drilling rigs in the Barents Sea that might be located remotely and fare from a base.

An unconventional method of drilling that has been utilized in some wells in the Barents Sea is controlled mud level drilling (CML) and controlled mud cap drilling (CMCD), see section 2.3.2.3.

2.3.2 Mud Cap Drilling

The unconventional method of drilling called mud cap drilling has been developed as a contingency method when drilling into formations where severe losses occur. Mud cap drilling deviates from the traditional way of drilling a well by having no returns to the surface. This requires that the formation fractures or karsts (vugs, caverns) are able to receive the cuttings and the drilling fluid used to drill the section.

2.3.2.1 Principles of Mud Cap Drilling

What characterizes mud cap drilling is the mud cap fluid that the annulus contains. The mud cap fluid in the annulus is a viscous fluid that acts as a barrier for the migration of gas to surface.

If gas starts to migrate up the annulus, the choke pressure at the surface will increase due to gas lowering the annular fluid density. Annular mud cap fluid is then injected into the annulus with a rate that is greater than the gas migration rate, which results in gas being bullheaded back into the formation. The different mud cap drilling (MCD) techniques have different ways of controlling the gas migration.

A sacrificial fluid is used as the drilling fluid and is usually seawater for offshore operations due to the availability. This is used to cool and lubricate the bit in addition to bringing the drilled cuttings into the fractures called the interaction zone. To get a proper hole cleaning, high viscosity pills can be pumped down the drill string to sweep the area of cuttings (Wilson et al., 2014). The interaction zone often has high effective permeability and a high capacity for allowing big volumes of sacrificial fluid and cuttings into the fracture (Goodwin et al., 2014).

Some mud cap drilling methods typically use a value of 0.2-0.4 sg higher than the pore pressure. There are different types of MCD techniques, where some use a rotating control device (RCD) and others have an open annulus. In floating mud cap drilling, the annulus

is open to the atmosphere and the liquid column is free to move. Injection of mud cap fluid is performed when needed. Dynamic mud cap drilling is similar to floating mud cap drilling but has a continuous injection of mud cap fluid into the annulus instead of a periodic injection (Goodwin et al., 2014). This is to avoid the possibility of some formation gas migrating to surface. This technique uses a high mud weight to control the fluid level in the annulus and balances it against the pore pressure. Injection can be performed in parallel while drilling and tripping and non-productive time can be reduced.

Figure 2.7 shows the principle of how dynamic mud cap drilling is performed. Sacrificial drilling fluid is pumped down the drill string from the mud pit and is pushed into the formation along with the drilled cuttings. Another mud pit supplies the annulus with viscous mud cap fluid that is continuously injected to balance the pore pressure and keep the gas from migrating to surface. The ideal case is to continuously inject mud cap fluid to ensure that the gas will not migrate upwards by using heavier mud weight and a low level in the riser so that it is possible to control the fluid injection into the annulus.
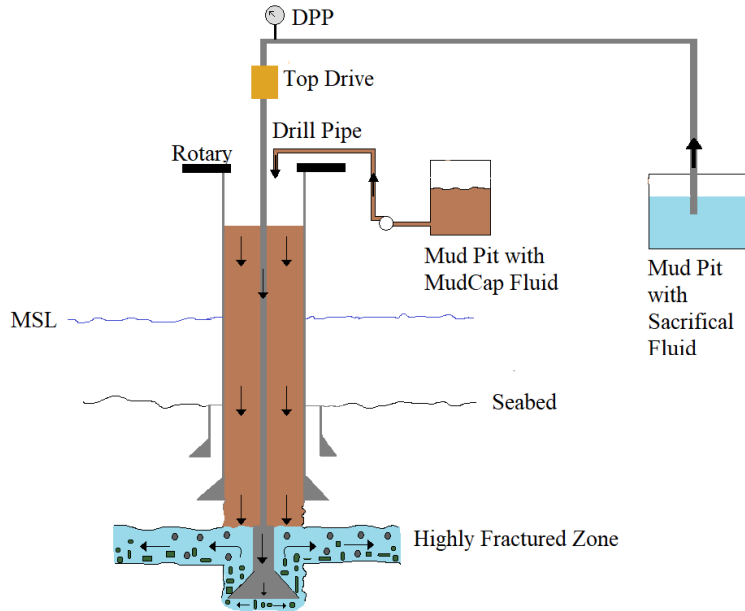
Figure 2.7: Dynamic mud cap drilling.

Estimating the required annular injection volume and rate of mud cap fluid is important for this unconventional method of drilling. The annular injection rate and volume are given by Equation 2.5 and Equation 2.6, respectively. The injection rate is a function of the gas migration velocity, v_t (Colbert et al., 2002).

$$Q_{inj} = \frac{60 S F v_t \pi (ID_{Hole}^2 - OD_{DP}^2) 10^{-6}}{4} \qquad (2.5)$$

Where Q_{inj} is the injection rate in m^3/min and SF is a safety factor.

$$V_{inj} = Q_{inj}t \qquad (2.6)$$

where t is the time in minutes it takes to drill the fractured section.

According to Colbert et al. (2002) there is a rule of thumb for the migration velocity of gas. For gas migration in oil-based mud the velocity is between 7-15 ft/min corresponding to 0.036-0.076 m/s, and the "old drillers rule of thumb" says that gas migrates in oil-based mud with a velocity of 1000 ft/hr corresponding to 0.085 m/s. Chapter 2.4 highlights some other estimates of the gas migration velocity.

2.3.2.2 Case Study: Conventional Drilling of a Karstified Reservoir in the Barents Sea

When drilling exploration and appraisal wells in the Barents Sea, there is a potential risk of encountering karstified carbonates. Due to remote locations and lack of infrastructures, these wells will be drilled from floaters and the BOP will be located subsea. To be capable of year-round operations in the Arctic area, the floater should be winterized (Bysveen et al., 2017).

In the summer of 2015, an appraisal well was drilled in the Barents Sea from a semi-submersible rig, by Lundin Norway. It was assumed that the karstified part of the reservoir had collapsed or was filled with sediments, but large mud volumes and quantities of different LCM and cement material were available on the rig as a contingency measure.

When taking a core sample from the $8^{1/2}$" hole in the carbonate reservoir section, the core bit dropped 2 m, which resulted in a massive mud loss (Bysveen et al., 2017). The riser level dropped and it was not possible to maintain a riser full of mud, so contingency measures were needed resulting in a shut-in of the BOP located subsea. The well was periodically kept full with seawater. Different measures were performed in an attempt to cure the loss zone but without luck. When the SICP increased, it was an indicator that gas was migrating up the annulus. Whenever the SICP reached 100 bar, the annulus was bullheaded with a high viscosity mud pill, chased with water. This reduced the SICP. To enable pumping of cement, the BHA was shot off resulting in the bottom part of the assembly to drop down into the loss zone, which incidentally caused the mud loss to stop (Bysveen et al., 2017). More than 2000 m^3 of fluid were pumped and displaced into the well together with 23 LCM pills to try and stop the losses.

To avoid a similar situation like the one described above, Lundin wanted to explore different methods that could be used in the future to drill similar wells where there was a potential risk of penetrating karstified carbonates (Bysveen et al., 2017). Reservoirs with karstified carbonates are present in the Barents Sea and due to the remote location, metocean conditions such as low- pressure polar storms, rules and regulations and environmental aspect, a zero tolerance policy of hydrocarbons entering the wellbore and migrating to

the surface was introduced (Bysveen et al., 2017). Continuous injection down the annulus was decided the best viable option to control the reservoir gas. This solution was utilized with controlled mud level drilling and controlled mud cap drilling.

2.3.2.3   CML and CMCD

Controlled mud level (CML) technology is designed to drill post-BOP sections and can be used for all operations once the riser is run (Fossli et al., 2014). CML drilling is a type of managed pressured drilling (MPD) that controls the bottom hole pressure and the equivalent circulating density by manipulating the fluid level in the riser (Elahifar et al., 2017). The optimal water depth for use of this technology is around 300 metres or deeper, but CML technology has also been used for wells with water depths of around 100 metres. The location of the subsea pump module (SPM) on the riser decides the amount of pressure reduction available for the operation.

The pressure inside the riser is measured accurately by pressure sensors located inside the marine riser and used to calculate the fluid level inside the riser. Below these pressure sensors, an outlet to a subsea pump module (SPM) is located. Annulus fluid can be pumped back to the rig through the SPM and a mud return line (MRL) when needed to control the fluid level in the riser and the corresponding bottom hole pressure to maintain inside the mud window. The control system adjusts the SPM pump and decreases or increases the BHP as wanted based on the measurements from the pressure sensors (Smaaskjar et al., 2018).

The operator company, Lundin, have since 2016 used Enhanced Drillings EC-Drill System to enable CML drilling in the Barents Sea (Smaaskjar et al., 2018). This equipment was implemented on the semi-submersible rig Leiv Eriksson in June 2016. It took 3 months to upgrade the riser and the rest of the EC-Drill System. This equipment consists of a subsea pump module (SPM), an SPM launch and recovery system (LARS), modified riser joint (MRJ), umbilical winch and umbilical, mud return line (MRL), topside MRL flow meter, top-fill pump and the CML control system. The different components are presented in Figure 2.8.

1	Wellhead
2	Blow Out Preventer
3	Modified Riser Joint
4	Pressure Sensors
5	Riser Isolation Valves
6	Subsea Pump Module
7	Mud Return Line
8	Umbilical
9	Umbilical Winch
10	Launch and Recovery System
11	Top Fill Mud Pit
12	Diverter
13	EC Drill Operator Station
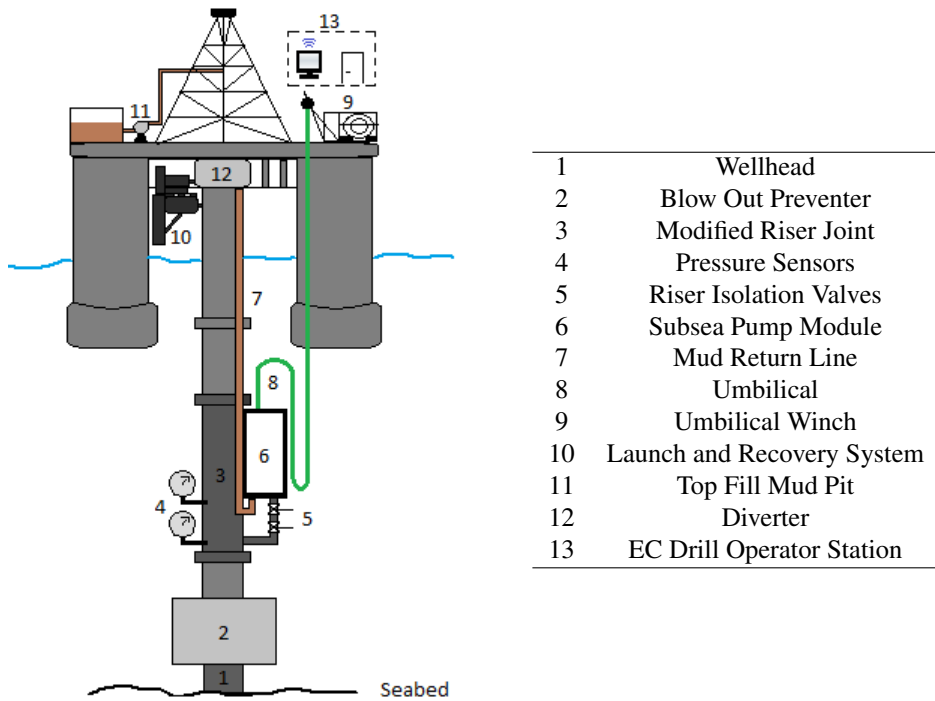
Figure 2.8: CML system (based on Smaaskjar et al. (2018)).

A riser joint was modified to enable drilling fluid to be extracted from the riser at some depth between the BOP located subsea and the sea level. The modified riser joint has also been equipped with pressure sensors to calculate the fluid level in the riser and valves to isolate the SPM that is connected to this outlet from the riser if necessary. The SPM consists of a series of pumps that is able to pump up to 6000 lpm and lift the mud from the riser to surface through the MRL. The MRL is 6" and can either be installed separately or integrated into the riser (Fossli et al., 2014).

The operator work station that runs the computer-based control system is located on the drill floor. The control system manipulates the fluid level in the riser to make sure the bottom hole pressure is within the operational drilling window (Fossli et al., 2014). The system has three different modes; manual mode, constant riser pressure mode and automatic mode. The operator controls the pump speed of the SPM manually based on the readings from the riser pressure sensors in manual mode. During constant riser pressure mode, the pump will automatically adjust to maintain a pre-determined riser pressure that is set by the operator. In automatic mode, the pump is also set to maintain a pre-determined riser pressure, but this pressure is found from an ECD lookup table to compensate for ECD variations (Fossli et al., 2014).

There is a continuous injection of mud into the riser at the diverter housing from the top-fill pump, but also from the booster line. The top-fill pump is designed to supply between 400-2000 lpm directly from the active mud pits. The speed can be regulated with a variable speed controller (Smaaskjar et al., 2018) and the pump is controlled remotely from the EC-Drill control system.

Another benefit with the EC-Drill system and CML technology is faster and improved kick detection when tripping and drilling. In conventional drilling, the kick detection depends on monitoring the mud level in the mud pits and monitoring of the return flow. A limitation with monitoring mud pits is that rig heave can influence the mud level. This limitation is avoided when operating with the EC-Drill system. This system also monitors the hydrostatic pressure in the riser and the speed of the SPM. By monitoring the SPM speed, the hydrostatic pressure in the riser and the flow in and out of the well together, it is easier to detect an influx. The MRL will always be full of mud which means continuous flow measurements. The control system has as mentioned different operating modes. By keeping the SPM at a constant speed, any influx will be seen as an increase in the riser pressure due to increased volume in the riser. If operating with constant riser pressure, an increase in the speed of the SPM in rpm or $amperage$ (power) can be an indication of an influx (Elahifar et al., 2017). Results gained from performing kick drills shows that volume instabilities can be detected earlier with the EC-system compared to conventional drilling (Godhavn et al., 2016). Figure 2.9 presented in Elahifar et al. (2017), shows how the parameters mentioned above respond to a kick drill performed in the Gulf of Mexico. As Figure 2.9 shows, both the riser pressure and the SPM increases instantly, indicating a kick after 10 s. The flow out measured by the Coriolis flow meter also installed on the rig gives the second indicator after 48 s.

Figure 2.9: Immediate kick detection during kick drill with the use of CML technology (Elahifar et al., 2017).

According to Godhavn et al. (2016), a real kick with a very low flow rate of approx 10

gpm was not detected with the CML parameters but was seen on the pit volume after some minutes. This implies that there is a limitation with the system for influx with a flow rate less than the measurement accuracy of the flow meter. In this scenario, observing the accumulated pit volumes will be the only possible solution for detecting the kick.

The EC-Drill system is equipped with a fingerprinting functionality which improves well monitoring during connections and other repeatable events during offshore operations (Elahifar et al., 2017). The software monitors gain and loss when U-tubing from the drill pipe to the annulus occurs. This happens when making connections or stopping circulation with a low riser level (Fossli et al., 2014). The current trend during a connection will be compared to a baseline from the previously recorded connection. For this fingerprinting to work, the driller needs to follow the same pump ramp schedule on every connection (Fossli et al., 2014). During a connection, the different parameters that are measured are not stable and can change. The baseline from a previous connection can help detect any deviation from the connection procedure and indicate loss or gain (Elahifar et al., 2017). Figure 2.10 shows how the parameters behave in a normal connection operation where the current connection parameters overlap the baseline. Figure 2.11 shows how the parameters behave during a connection with influx present. The EC-Drill system detects the kick 35 s earlier than the conventional method by viewing the mud level in the mud pits. Both the SPM speed and the riser pressure deviates from their corresponding black baseline.
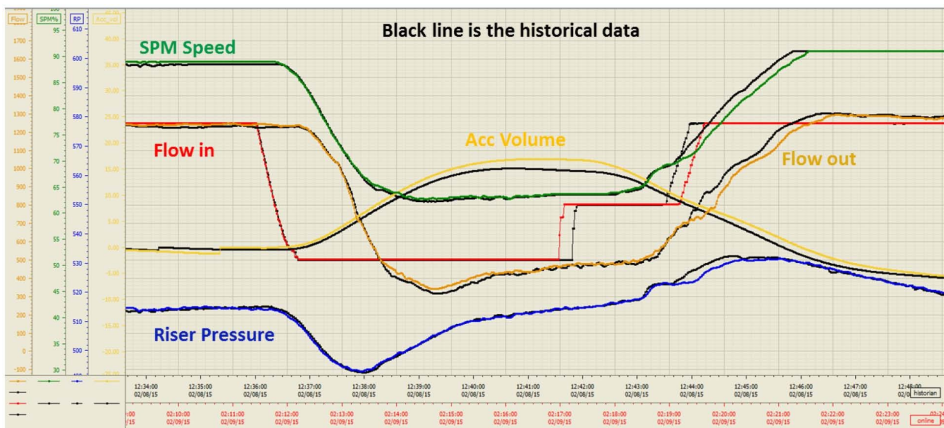
Figure 2.10: How fingerprint looks like for a normal connection (Elahifar et al., 2017).
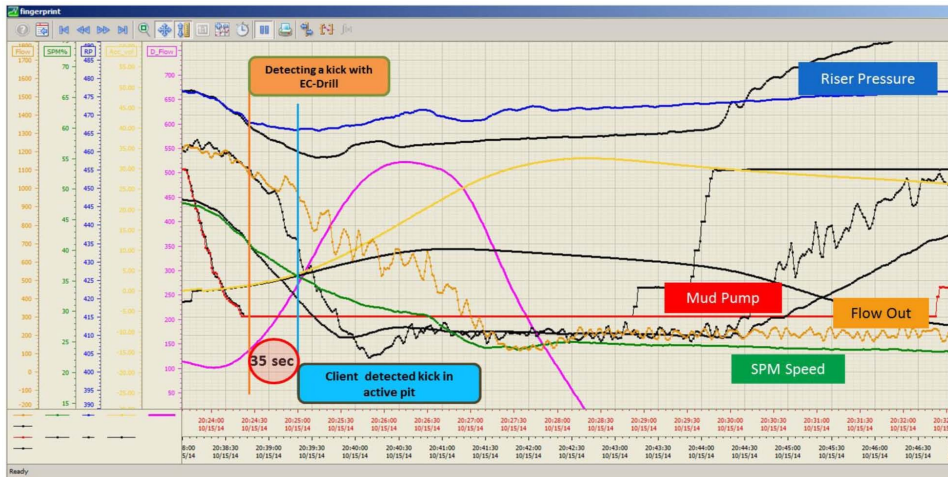
Figure 2.11: How fingerprint looks like for a connection with an influx present (Elahifar et al., 2017).

As a contingency measure if total mud losses were to occur, the rig was also equipped so that controlled mud cap drilling (CMCD) could be introduced. The top-fill pump would supply the riser with viscous mud cap fluid from the top of the riser. The boost line would also supply the riser with mud cap fluid with a higher injection rate than required (Bysveen et al., 2017). Figure 2.12 shows a sketch of how the CMCD system can look like. The mud cap fluid level in the riser is the controlling parameter for the injection rate. Since there is a zero-tolerance of gas in the wellbore, the minimum required injection rate of mud cap fluid down the annulus needs to be greater than the gas migration rate. The injection rate can be adjusted with the SPM. The injection rate needed to overcome the gas migration rate is a function of the mud cap fluid level in the riser, the friction pressure caused by the injection rate and formation injectivity (Bysveen et al., 2017). Currently, regulations on the Norwegian Continental Shelf (NCS) does not allow drilling to be continued for more than one stand with the CMCD technique if total losses occur and there are no returns to the surface. In theory, it should be possible to continue to drill with continuous injection into the annulus even if there are no returns to the surface.
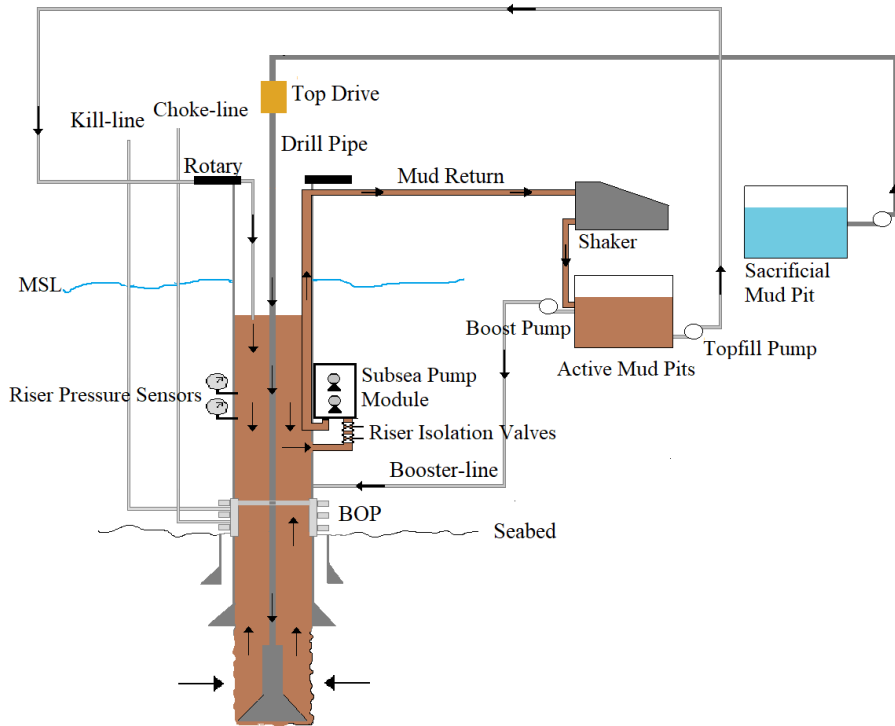
Figure 2.12: How a principle setup of the CMCD system can look like (inspired by Bysveen et al. (2017)).

The injection rate is dependent on the gas migration rate. According to Bysveen et al. (2017) the estimates of the gas migration rate varies depending on the method used to evaluate it. This paper presents different estimates for the same well. Actual observations from pressurized mud cap drilling (PMCD) operations estimated the gas migration rate to be 0.03 m/s using a 1.55 sg mud in a 6" hole and with a $3^{1/2}$" DP. The Olga-Well-Kill simulator estimates it to be 0.65-0.75 m/s for a $8^{1/2}$" hole. Different bubble rise models estimate it to lie between 0.12-0.75 m/s. Chapter 2.4 elaborates on different gas migration models and their estimates. The estimates above are based on the drilling fluid properties given in Table 2.1.

Table 2.1: Drilling fluid properties used to estimate gas migration rate for a CMCD system (Bysveen et al., 2017).

Property	Symbol	Value	Unit
Mud density	ρ_{mud}	1.15	sg
Gas density	ρ_{gas}	0.23	sg
Surface tension gas-mud	σ	0.077	$\frac{N}{m}$
Absolute viscosity from Fann data	μ_l	25	cP

Both CML and CMCD uses the same EC-Drill system. The difference between the two operating techniques is that CMCD is a spontaneous reaction. CMCD is a drilling technique with no returns to the surface. Losing the drilling fluid and cuttings to the formation is a spontaneous reaction when drilling into a zone where total losses occur. Hence, when drilling with CMCD, the only thing that can be controlled is the amount of viscous mud cap fluid to inject into the annulus from the top-fill pump at the surface and the riser booster pump and the use of the SPM to adjust the level in the riser. The injection rate will be determined by the riser pressure sensors and the SPM will adjust the pump speed based on these measurements. The bottom hole pressure can not be controlled with the CMCD technique due to infinite injectivity into the void space leading to a constant bottom hole pressure on top of the loss zone (Smaaskjar et al., 2018).

The CML technology operates with an open system, which means that it is open to the atmosphere when operating. This differs from the closed MPD systems, which uses a rotational control device (RCD) to adjust the pressure downhole by adding a back pressure to the fluid column. Operating with an RCD involves faster control and regulation of the bottom hole pressure compared to CML technology. Moving large fluid volumes in and out of the riser to adjust the pressure will take more time than to adjust a choke (Godhavn et al., 2016). RCD, chokes and subsea equipment like the subsea pump disks are vulnerable for wear. The EC-Drill technology is designed to be more flexible and have the ability to regulate pressure instabilities compared to conventional drilling techniques, but at the same time have the same well barrier and well control principles (Fossli et al., 2014). To be able to run all types of tubular and equipment into the well, the system needs to be open. The primary barrier will still be the drilling fluid and the secondary barrier is the subsea BOP, wellhead, casing and cement. In a well control event, the subsea BOP will be closed and the EC-Drill system will be isolated.

Health, safety and environment (HSE) are of great importance to the operator companies, so well integrity needs to be maintained. A barrier schematic of the mud cap drilling principle is presented in Figure 2.13. The primary barrier consists of the sacrificial drilling fluid and the backpressure valve (BPV) on the drill string. The secondary barrier includes the previous casing and cement, the casing seal assembly, the high-pressure wellhead, SS BOP and the BPV on the drill string.
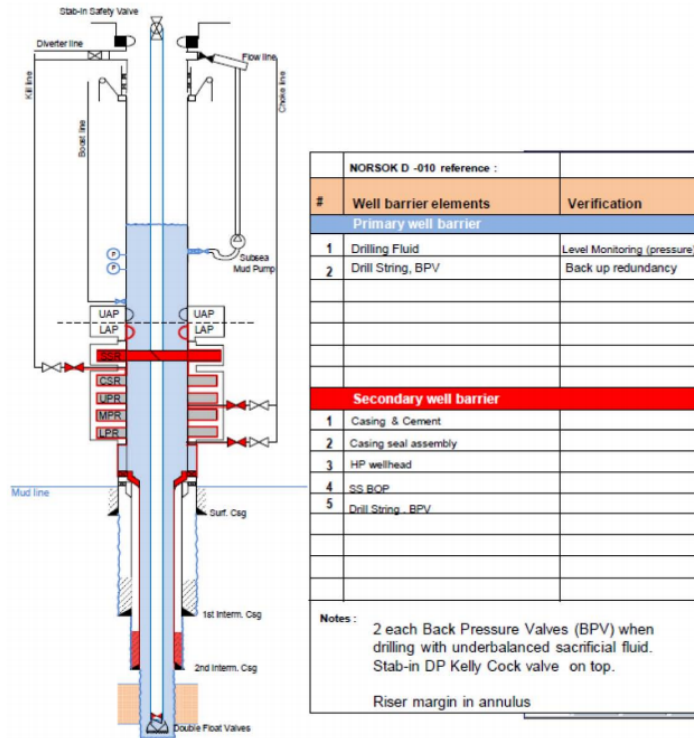
Figure 2.13: Well barrier schematic for the CMCD principle (Bysveen et al., 2017).

The fluid level in the riser will drop when drilling into karsts and open fractures since circulation of mud will stop. Amount of overbalance, annulus friction and injectivity are the parameters deciding at what rate the riser level drops (Bysveen et al., 2017). When total losses occur, the pump system will be shut down and the riser isolation valves (RIV) will close and isolate the CML system. The CML control system can still measure accurate pressure in the riser due to the pressure sensors, which can be used to determine the loss rate (Bysveen et al., 2017). The level in the riser is then increased to a point where the injection rate of mud cap fluid equals the minimum rate that gives a gas-free annulus, in addition to a safety factor. The RIV have opened again so that the SPM can be used to adjust the injection rate to the desired one.

2.3.2.4   Case Study: Drilling a Horizontal Well in Karstified Carbonates in the Barents Sea with the CML Technology

In 2017, Lundin made a decision to drill a horizontal well in the same carbonate reservoir as the appraisal well that was drilled in 2015 with the EC-Drill technology. An extended production test of the well over a 60 day period would also be performed (Tangen et al., 2019). The operator company had successfully drilled seven exploration wells and a num-

ber of geological sidetracks since the Leiv Eriksson was upgraded in 2016, so the rig crew had experience with the CML system and also gained confidence in it (Tangen et al., 2019).

The horizontal well was designed to consist of a conductor of size 36" x 30", a 20" surface casing and a $10^{3/4}$" production casing above the carbonate reservoir section. To eliminate the risk of gas migration from the reservoir gas cap when drilling the horizontal section of the oil leg, this section was planned to be isolated with an $8^{5/8}$" expandable liner. The 700 m horizontal section was planned to be drilled as an $8^{1/2}$" open hole (Tangen et al., 2019). A schematic of the well design is presented in Figure 2.14.
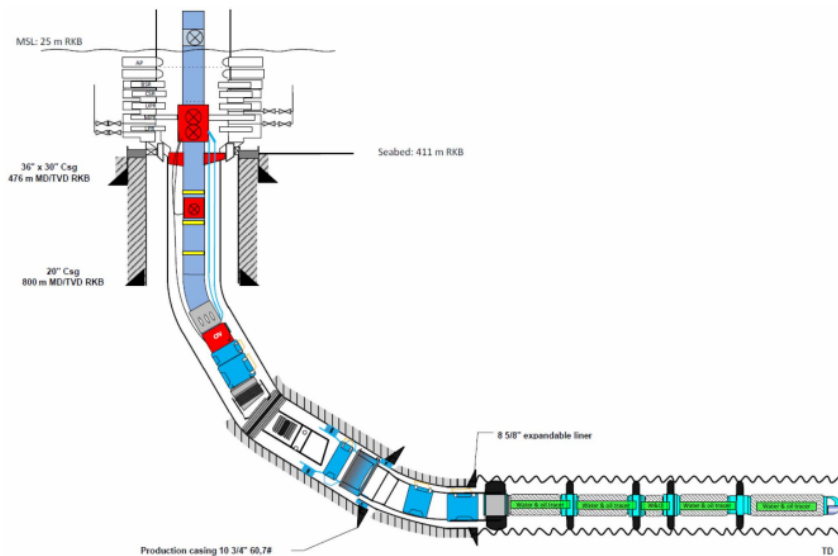
Figure 2.14: "Well and completion design" by Tangen et al. (2019).

The bottom hole assembly was upgraded with lessons learned from the incident in 2015. To be able to achieve optimal space out for installing wireline pressure control equipment if necessary, a drilling stand with 3 full opening safety valves (FOSV) were a part of the string design for the reservoir sections. Two double floats above a circulation sub were also a part of the new BHA. The circulation sub would provide an unrestricted flow path for LCM and the double floats were installed to mitigate the float leakage. These were pressure tested before each run in hole. The rig was also equipped with a wired drill pipe so that the pressure in the well could be measured both in a dynamic mode, but also in a static mode. Usually, there is a pressure sensor in the measurement while drilling (MWD) tool, but this only records the pressure while the pump is in working mode meaning that there is no pressure measurements when the pump is stopped and the well is static (Tangen et al., 2019). The wired pipe gives a constant pressure measurement and together with the pressure sensors in the riser, accurate pressure control was possible at all times during operation.

The modified riser was run with the BOP and the riser after the surface casing was installed. It took 4 hours to install and test the CML system. The Alta field in the Barents Sea has a water depth of 386 metres and the SPM on the riser was located 260 metres from the RKB (Tangen et al., 2019). Both the intermediate section and the reservoir gas cap section were drilled with a reduced riser level and no losses were encountered. The operation of running, cementing and expanding the $8^{5/8}$" liner went smoothly with the CML technique which allowed the liner to be pressure tested by reducing the riser level to 194 m below RKB.

The mud weight used to drill the reservoir section, including the gas cap section, was 1.15 sg. This was the mud weight that would provide optimal mud level for both the CML mode and the CMCD mode, if a total loss scenario were to happen. While drilling the reservoir section, the top-fill pump and the booster pump continuously supplied the well with 400 lpm and 1000 lpm, respectively. 2000 lpm was in addition circulated down the drill string. The pumps were lined this way to ensure that the pumps would be able to maintain control over the riser level in a CMCD scenario. During drilling, the mud level was reduced to 163 m below RKB so that the BHP had an overbalance of 3.5 $bara$.

When drilling the $8^{1/2}$" section there was a big risk of encountering large voids and fractures so large volumes of mud, LCM and thixotropic cement was present on and near the rig. There were three major loss zones when drilling the reservoir section, which is presented in Figure 2.15.
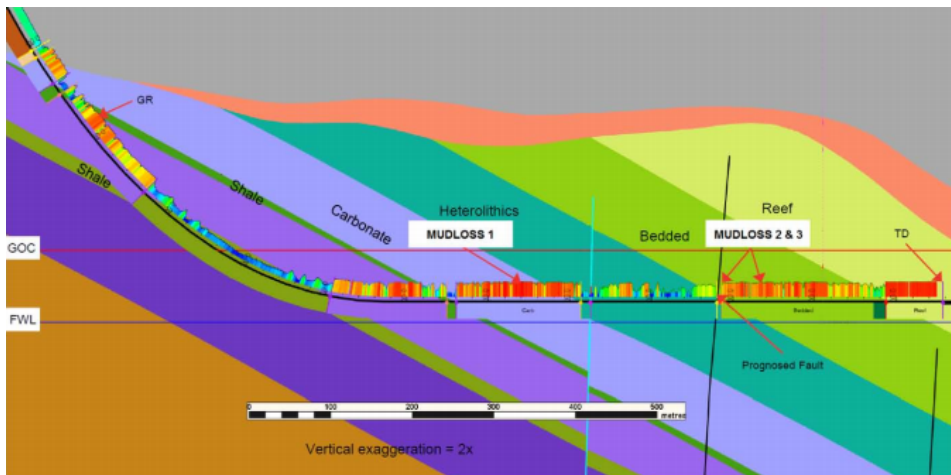
Figure 2.15: Well profile with loss zones by Tangen et al. (2019).

Drilling was stopped when a dynamic loss of 70 m^3/h was recorded while drilling through the first loss zone. The drill string was picked off bottom and spaced out. After drilling an additional 4 m with a dynamic loss of 36 m^3/h to log the loss zone with a resistivity imaging tool, the bit was pulled off bottom and the planned LCM strategy executed. This involved pumping down a LCM pill. This did not prove to be successful and it was de-

cided to pump and displace 8 m^3 of thixotropic cement slurry through the bit. Waiting on cement took 12 hours and when drilling resumed the high loss rates were reduced, which indicated that the void had successfully been plugged. Drilling resumed with a reduced circulation rate of 1500 lpm. The mud weight was increased to 1.16 sg due to adding LCM material to the mud system and the circulation rate increased to 1800 lpm. The riser level was reduced from 163 m to 180 m below RKB to maintain overbalance.

The next loss zone was encountered 245 m further down the well. A dynamic and static loss rate of 27 m^3/h and 6 m^3/h, respectively, was observed. The LCM strategy consisted of pumping down 3 thixotropic cement pills. The static loss rate reduced from 6 m^3/h to 2.3 m^3/h when pumping the second pill. Prior to pumping the third pill, a water glass pill consisting of 4.5 m^3 sodium silicate, followed by a spacer and 4.5 m^3 calcium chloride was pumped down the well. This method reduced the static loss rate to zero enabling further drilling. The dynamic loss rate was reduced from 15 m^3/h to 2 m^3/h while drilling.

After 51 m, the third loss zone was encountered. The dynamic loss rate was 24 m^3/h and the static loss rate was 14 m^3/h. Drilling continued without curing the losses for 47 m so that the loss zone could be logged with the resistivity imaging tool. A thixotropic cement pill of 12 m^3 was pumped down the well followed by a water glass pill and 8.7 m^3 of thixotropic cement plug. It took 6 hours for the static losses to reduce to 3 m^3/h and drilling to continue. The riser level was reduced from 163 m to 173 m for the last drilling section to TD to try to reduce the dynamic loss rate from 5-10 m^3/h to zero.

The drilling operation performed after installation of the EC-Drill System in the Barents Sea did only use the CML technique and not the CMCD technique since total losses were avoided. Severe losses, on the other hand, were encountered, but there were still some returns of cuttings to surface enabling further drilling. The dynamic mud losses ranged from 1-70 m^3/h resulting in a total loss of 2400 m^3 of 1.15 and 1.16 sg mud. Lundin managed to keep an overbalance of 3.5 bar when the well was static and dynamic by using the EC-Drill System during the whole operation making it possible to drill the reservoir section. The pressure control of automatic ECD compensation when moving from static mode to dynamic mode was tested during a connection giving a result of $\pm$ 0.75 bar pressure control. The flow test ended up lasting 70 days and the results showed that there were no skin and infinite permeability (Tangen et al., 2019). The temperature of the fluid arriving at the production choke was so low due to a cool riser that excessive waxing occurred. To avoid waxing when producing through the riser, the riser level was reduced to 250 m below RKB so that the arrival temperature was high enough (Tangen et al., 2019).

If this well had been drilled with a conventional method, a total loss situation would most likely have occurred at the first loss zone and further drilling would probably not be possible.

2.3.2.5   NORSOK

There has been successful experience with the unconventional drilling technique, CML, and the contingency method, CMCD, over the last years. Based on the development of these methods, there is reason to believe that these mud cap drilling methods will be accepted and included in the new NORSOK-D-010 standard in 2019.

2.4   Gas Migration Velocity

When gas enters a well in an underbalanced situation, it will start to migrate to the surface due to density and pressure differences in the well. The velocity that the rising gas has is an important parameter when exerting well control. If the migration velocity is known, the time it takes the gas kick to reach the BOP and creating a well control problem can be calculated. By knowing the migration velocity, the pump volume (l/min) that is required to bullhead the gas down into the formation can also be calculated.

Factors that will govern gas migration rate includes density difference between the drilling fluid and the influx fluid, type of drilling fluid, viscosity of the fluid, surface tension, flow regime and the size and shape of the influx fluid.

The theory on gas migration velocity is wide and there are a number of different approaches to estimate the gas migration velocity. The industry has developed a dynamic multiphase flow simulator called OLGA-WELL-KILL which can be used to predict the gas migration velocity for a specific well.

2.4.1   Flow Regimes

The type of flow regime is based on how the different phases are distributed in the flow, and Figure 2.16 illustrates flow regimes in vertical pipes that gas bubbles rising in a stagnant liquid can experience.

Ideally-separated bubble flow is when gas bubbles are dispersed or suspended in a continuous liquid, but the bubbles do not interact with each other (Kataoka and Serizawa, 2010). Other flow regimes that are characterized as bubble flow is interacting bubble flow, churn turbulent bubble flow and clustered bubble flow.

Dispersed flow is characterized by smaller bubbles being distributed in the continuous phase. For the scenario of air and water, air bubbles are the distributed phase and water is the continuous phase. The dispersed flow regime depends on the density ratio for the two phases, $\frac{\rho_d}{\rho_c}$, where ρ_d represents the density of the distributed phase and ρ_c for the continuous phase (Brennen, 2005). A dispersed flow pattern can be caused by turbulence.

Characterization of slug flow is sections of liquid separated by long bubbles of gas. According to Clift et al. (2005) when the diameter ratio, $\frac{d_e}{D}$, where d_e is the equivalent diameter of a bubble and D is the pipe diameter, exceeds a value of 0.6, the diameter of the pipe becomes the controlling length influencing the velocity of the bubble and the shape of it. These types of bubbles travel as slugs. Smaller bubbles tend to follow in the wake of the slug due to the lower pressure in this region.
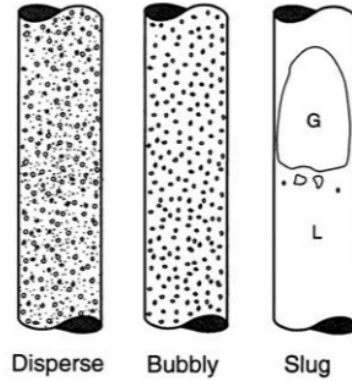
Figure 2.16: Different vertical flow regimes (Brennen, 2005).

2.4.2   Size and Shape of a Bubble

The shape and size of the gas bubbles affect the gas migration velocity and depends on fluid properties such as densities, viscosity and surface tension and operational conditions like velocity, temperature and pressure. The flow regime is based on how the different phases are distributed in the flow.

Bubbles in free rise in infinite media under the influence of buoyancy are according to Clift et al. (2005) divided into three categories: spherical, ellipsoidal and spherical- or ellipsoidal-cap. Figure 2.17 defines the different shape categories as functions of Reynolds number and Eötvös number. Reynolds number and Eötvös number are given by Equations 2.7 and 2.8, respectively,

$$Re = \frac{\rho d_e v_t}{\mu} \tag{2.7}$$

$$Eo = \frac{g(\rho_l - \rho_g)d_e^2}{\sigma} \tag{2.8}$$

where ρ is density, d_e is the equivalent spherical diameter, v_t is the terminal rise velocity, μ is the viscosity, σ is the surface tension between the fluids and $\Delta\rho$ is the density difference between the fluids.

According to Figure 2.17, low Reynolds numbers gives spherical bubbles. Ellipsoidal bubbles have high Reynolds numbers and intermediate values of Eötvös number. For

spherical-cap bubbles the Reynolds number is greater than 1.2 and the Eötvös number needs to be greater than 40. Clift et al. (2005) highlight that these properties are usually seen for bubbles with volume greater than 3 cm^3, which corresponds to an equivalent diameter greater than 1.8 cm. This was seen in experiments where air bubbles were photographed when rising freely through water under normal conditions.
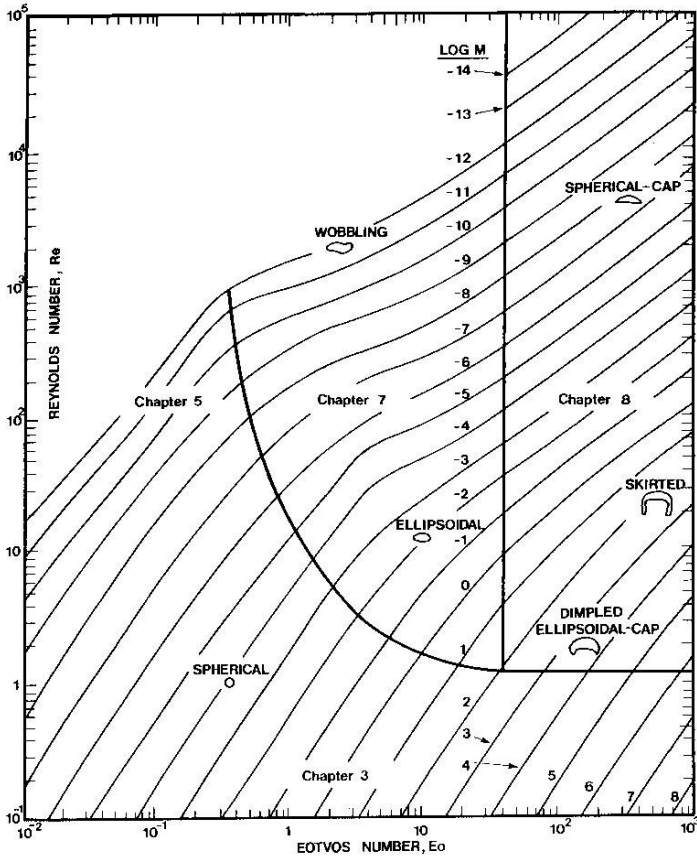
Figure 2.17: "Shape regimes for bubbles and drops in unhindered gravitational motion through liquids" (Clift et al., 2005).

Wichterle et al. (2009) refers to Clift et al. (2005) and Figure 2.17 and states that medium-sized bubbles of ellipsoidal shape have an equivalent diameter ranging from 1 mm to 15 mm based on previous air-water experiments. This suggests that spherical bubbles have d_e <1 mm and spherical/ellipsoidal cap bubbles have d_e >15 mm. These limits are presented in Table 2.2.

Table 2.2: Size and shape of bubbles according to Wichterle et al. (2009).

Size of Bubble	d_e [mm]	Shape
Small	> 1	Spherical
Intermediate	1-15	Ellipsoidal
Large	< 15	Spherical/Ellipsoidal Cap

A Taylor bubble is located in the spherical-cap region in Figure 2.17. What characterizes a Taylor bubble is that it occupies a big part of the cross-section of the pipe and has a bullet shape, with a spherical cap and a flat bottom. A sketch of a Taylor bubble is presented in Figure 2.18b. If the equivalent diameter is reduced, both Reynolds number and Eötvös number will decrease, so according to Figure 2.17, smaller bubbles often have a spherical shape, which is illustrated in Figure 2.18a.

(a) Small, spherical bubbles.   **(b)** Taylor bubble.
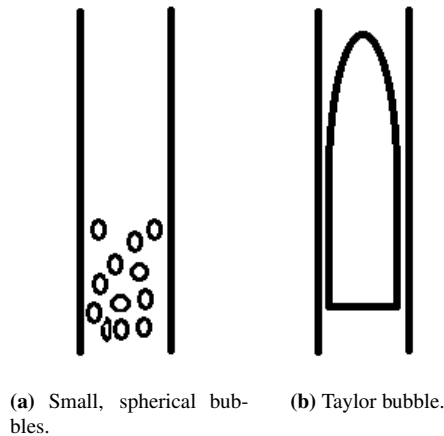
Figure 2.18: Different bubble shapes.

For Reynolds numbers greater than 150 the base of the bubble is quite flat, and the wake angle, θ_w, is about 50 °. For Reynolds numbers lower than 150, the wake angle is larger. Wake angle can be given by Equation 2.9 for bubbles in the spherical- or ellipsoidal cap region (Clift et al., 2005).

$$\theta_w = 50 + 190e^{-0.62Re^{0.4}} \tag{2.9}$$
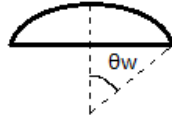
Figure 2.19: Wake angle, θ_w, for spherical-cap bubbles.

2.4.2.1   Factors Affecting the Bubble Shape

The shape of the bubble is affected by surface tension between the liquid and the gas, viscosity of the liquid, densities of the fluids, inertia and buoyancy. Small isolated bubbles that have a spherical shape is dominated by surface tension effects, according to Clift et al. (2005).

The density difference between the two phases affects the shape of the bubble. If there were to be no density difference, there would be no tendency of the bubble to rise and the shape of the bubble would only be a function of interfacial tension (Rader et al., 1975). Rader et al. (1975) refer to both Dumitrescu (1943) and Davies and Taylor (1950a) when stating that "a low-density bubble must assume a shape that allows the pressure everywhere on the surface of the bubble to be about the same. A large bubble rising in an extended liquid was found to have a lenticular shape, with a spherical cap and a flat bottom." Viscous characteristics would also affect the shape of the bubble. The bubble had a more streamlined shape when the viscosity of the liquid increased (Rader et al., 1975).

2.4.3   Terminal Rise Velocity

Skalle et al. (1991) present the expression that Zuber and Findlay (1965) and Hasan et al. (1988) came up with for the gas velocity as a function of the mixture velocity and the terminal rise velocity in stagnant fluid. This relationship is given by Equation 2.10.

$$\bar{v}_g = C_0 v_m + v_t \qquad (2.10)$$

where $\bar{v}_g$ = mean gas velocity, v_t = terminal rise velocity/ terminal rise velocity in a stagnant fluid and v_m = mixture velocity and is given by Equation 2.11. C_0 is a constant that depends on the velocity profile in front of the bubble nose.

$$v_m = \frac{(q_l + q_g)}{A} \qquad (2.11)$$

where q_L is the liquid flow rate, q_g is the gas flow rate and A is the cross-sectional area of the pipe. In the case of a stagnant liquid phase, there is no mixture velocity and the first term in Equation 2.10 is then neglected. Hence, the gas velocity in a stagnant liquid is just a function of the terminal rise velocity.

There are many correlations for the bubble-rise velocity and authors refer to it as both bubble rise velocity and terminal rise velocity. Terminal rise velocity will be used in this paper. The correlations used to calculate the velocity are functions of different parameters

such as bubble size, the density difference between the different fluids, surface tension, viscosity and pipe diameter.

The forces that affect the terminal velocity of a bubble in a stagnant liquid column have been presented by Talaia (2007) and includes the gravity, buoyancy and drag force that the bubble is subjected to. When gas is immersed in a liquid fluid it will be subjected to an upward buoyancy force. Since the gas has a lower density than the surrounding fluid, the gas will rise upwards due to a greater buoyancy force than the weight of the immersed gas. The drag force works in the opposite direction together with the gravity force. The drag force includes the drag coefficient which is a function of the shape of the bubble and the Reynolds number. Other factors like liquid density, cross-sectional area and terminal rise velocity also affect the drag force. Drag force is given by Equation 2.12. The drag coeffecient C_D differs for different Reynolds number, and can be estimated for intermediate-sized bubbles with Equation 2.13.

$$F_D = \frac{1}{2}\rho v_t^2 C_D \frac{\pi}{4} d_e \qquad (2.12)$$

$$C_D = 0.365 Re^{0.143}(1 + 0.095 E_o)^{0.75}, for\, 1 < E_o < 20, Re > 30 \qquad (2.13)$$

According to Shi et al. (2017), the drag coefficient, C_D =48/Re or C_D =32/Re for bubbles with Re >1. For Re >1000, C_D =0.45. For low Reynolds number, Re <1, C_D =16/Re.

The velocity of the gas migrating to surface depends on how the bubbles are moving. There are two theories that must be evaluated. The large Taylor bubble theory assumes that the gas migrates as big slugs that almost fill the cross-section of the tube. Smaller trailing bubbles will get sucked into the wake of the larger leading bubble and coalescence occurs. These large bubbles can according to Krishna et al. (1999) have migration velocities approaching 2 m/s. If the bubbles get large enough, they tend to break up and the drag force on the bubble will increase resulting in a reduced migration velocity.
The other theory is that the bubbles will migrate to the surface as a bubble swarm consisting of different sizes of bubbles.

The literature study presented in this project has looked at the terminal rise velocity for bubbles moving through a Newtonian fluid such as water in a closed environment, so expansion of the bubbles can be neglected.

2.4.3.1   Terminal Velocity for Small Bubbles

The shape of the bubble is affected by surface tension between the liquid and the gas, viscosity of the liquid, inertia and buoyancy. Small isolated bubbles that have a spherical shape is dominated by surface tension effects and due to its low Reynolds number, there will be no wake at the rear of the particle. Stokes et al. (1901) solution for the terminal

velocity, v_t, of a small bubble with Reynolds number <2 is given by Equation 2.14, and is based on the drag coefficient from Stoke's law, C_D =24/Re.

$$v_t = \frac{1}{18} \frac{g d_e^2 (\rho_l - \rho_g)}{\mu_l} \tag{2.14}$$

d_e is the diameter of a volume equivalent sphere, g is gravity, ρ_l and ρ_g is the liquid and gas density and μ_l is the liquid viscosity.

Skalle et al. (1991) presented an empirical relationship for the in situ gas velocity for dispersed bubble flow given by Equation 2.15.

$$v_g = 1.2 v_m + 0.75 \tag{2.15}$$

where the gas velocity is given in ft/sec. The terminal rise velocity represents the last term in the equation, which corresponds to a velocity of 0.22 m/s. Skalle et al. (1991) concluded that for normal kick conditions when drilling underbalanced through a gas reservoir the dispersed bubble flow pattern will occur.

2.4.3.2 Terminal Velocity for Intermediate Bubbles

The Mendelson (1967) Equation for terminal velocity which is based on the wave analogy is given by Equation 2.16. This equation is valid for d_e >1.3 mm and low viscous liquids and it correlates well with the terminal velocity found in an air-water experiment at 20 °Celcius presented in Clift et al. (2005).

$$v_t = [\frac{2.14\sigma}{\rho_l d_e} + 0.505 g d_e]^{0.5} \tag{2.16}$$

where σ is the surface tension between the two phases.

The terminal velocity is defined differently for different flow regimes. Zuber and Findlay (1965) and Harmathy (1960) have two similar expressions for the terminal rise velocity for a bubble flow which have been presented in Skalle et al. (1991). These are given by Equation 2.17 and 2.18, respectively.

$$v_t = 1.41 \sqrt[4]{\frac{g\sigma(\rho_l - \rho_g)}{\rho_l^2}} \tag{2.17}$$

$$v_t = 1.53 \sqrt[4]{\frac{g\sigma(\rho_l - \rho_g)}{\rho_l^2}} \tag{2.18}$$

As can be seen from Equation 2.17 and 2.18, the only difference is the constant dimensionless Froude number. These equations differ from Equation 2.22 by including surface tension, σ, as a parameter and neglecting the effect of the pipe diameter. The equation

of Harmathy (1960) predicts a terminal velocity of 0.25 m/s for an air-water experiment performed with 1 bar presented in Johnson et al. (1991).

Kjølaas et al. (2017) have derived a model for the slip velocity of small bubbles in stagnant liquid, which corresponds to the terminal rise velocity of small bubbles. The model is based on the Harmathy (1960) model and represents the dashed line in Figure 2.20. The modified model accounts for bubble hindrance and attractive wake effects at low Reynolds number (Kjølaas et al., 2017). Figure 2.20 compares the modified Harmathy model to terminal rise velocities obtained from experiments performed with Nitrogen gas and Exxsol D60 at 45 and 70 bara presented in Kjølaas et al. (2017).
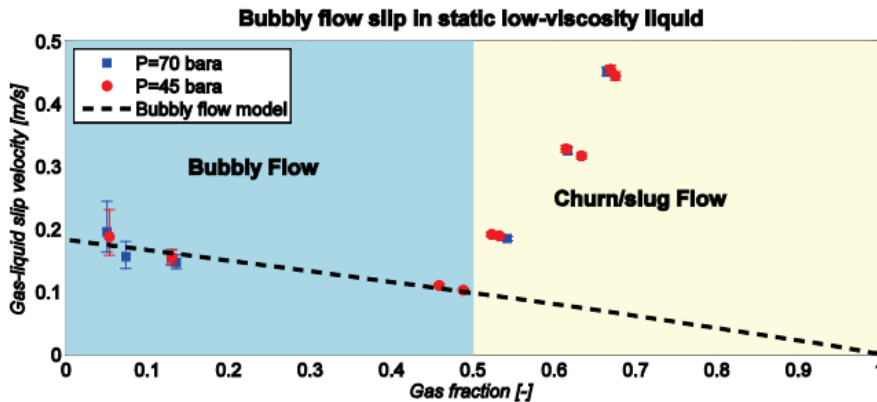
Figure 2.20: Gas-liquid slip velocity versus total gas volume fraction (Kjølaas et al., 2017).

The modified Harmathy model corresponds well to the data in the bubbly flow region. The model can not be used to describe the slug flow region.

2.4.3.3   Terminal Velocity for Taylor Bubbles

The so-called Taylor bubble velocity expresses the velocity for a Taylor bubble that moves through an inviscid liquid. The terminal velocity for this large, bullet-shaped bubble has been estimated by many.

Talaia (2007) have presented the terminal rise velocity for spherical cap bubbles estimated by Davies and Taylor (1950b). It is given by Equation 2.19 and both surface tension and viscosity are neglected. This equation is assumed to illustrate the velocity for a theoretical flow near the front of a complete sphere in an inviscid fluid.

$$v_t = \frac{2}{3}\sqrt{gR_b} = \frac{\sqrt{2}}{3}\sqrt{gd_e} \tag{2.19}$$

where R_b is the radius of curvature.

Davies and Taylor (1950b) performed an experiment to see how bubbles migrated through a tank with volume 2 ft x 2 ft x 2 ft, 6 in. Nitrobenzene was used as the liquid phase. The bubbles were photographed so that the radius of the bubble and the time it took the bubbles to reach the top of the tank could be determined. It was observed that the "top of the bubble was spherical and that is was more or less flat beneath".

14 bubbles were photographed and the volumes ranged from 1.48 to 33.8 cm^3. The radius of curvature, R_b, differed from 2.41 to 4.84 cm. The velocity obtained from the experiment correlated well with the calculated velocity when using Equation 2.19. This can be seen in Figure 2.21, where the terminal velocity obtained from the experiment is plotted against the calculated one. Since the experimental results correlate well with the results from Equation 2.19, the flow near the front of the bubble must be close to the flow in front of a complete sphere, even if the bubble is flat beneath.
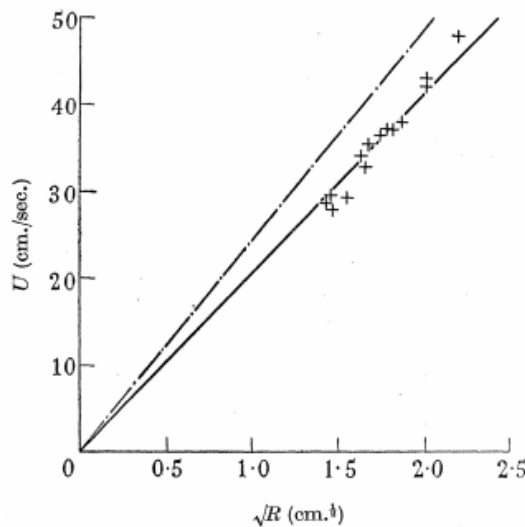
Figure 2.21: The relationship of the velocity of rise, U=v_t, and the square root of the radius of curvature, $\sqrt{R_b}$. + ; experimental results, — —; $v_t = 0.78\sqrt{gR_b}$ and ___ ; $v_t = \frac{2}{3}\sqrt{gR_b}$ (Davies and Taylor, 1950b).

Both Dumitrescu (1943) and Nicklin (1962) estimated the Froude number, Fr, which is the ratio of inertial to gravitational forces. It is a dimensionless number that varies with different flow regimes and it is presented in Equation 2.20.

$$Fr = \frac{v_t}{\sqrt{gd\frac{\rho_l - \rho_g}{\rho_l}}} \tag{2.20}$$

When the density of the gas is low, the term $\frac{\rho_l - \rho_g}{\rho_l}$ is equal to 1. This constant has a big impact on the terminal velocity of the bubble. Dumitrescu (1943) estimated the Froude number to be 0.351 for Taylor bubbles, which correlates with the value Nicklin (1962)

found from his air/water experiments. The equation for the terminal velocity for a Taylor bubble in a circular tube is given by Equation 2.21 and the only term that differs from Equation 2.19 since the diameter of a Taylor bubble is approximately the same as the diameter of the cross-section is the shape factor or Froude number.

$$v_t = 0.351\sqrt{gD} \tag{2.21}$$

When pipe diameter, D increase, so does the terminal velocity.

Others have also derived values for the Froude number, which are presented in Table 2.3.

Table 2.3: Estimated Froude number by different authors (Clift et al., 2005).

Reference	Fr_D
Damon et al. (1966)	0.33
Darby and Haque (1973)	0.35
Lando and Oakley (1967)	0.36
Davies and Taylor (1950b)	0.37

Both Equation 2.19 and 2.21 assumes that the pipe diameter is the only factor that affects the terminal rise velocity for "perfect" spherical cap bubbles and Taylor bubbles. Both Davies and Taylor (1950b) and Dumitrescu (1943) agreed that it was the need for the surface of the bubble to be isobar that decided the shape of the bubble (Viana et al., 2003).

Laird and Chisholm (1956) found similar terminal rise velocities as Davies and Taylor (1950b) when experimenting with gas bubbles moving through water in a 2 in diameter tube, but they saw a 10 % increase in the velocity when the bubble length increased from 2 to 25 diameters (Viana et al., 2003). The result suggests that the terminal rise velocity for Taylor bubbles are independent of the length of the bubble when exceeding a bubble length corresponding to a few pipe diameters.

Davies and Taylor (1950a) derived an expression for the Taylor bubble velocity given by Equation 2.22 that has been presented by Johnson et al. (1991). This equation only applies to gas rising in a pipe and not an annulus. Experiments performed in this paper indicates a Taylor velocity of 0.49 m/s for an air-water flow.

$$v_t = 0.35\sqrt{\frac{g(\rho_l - \rho_g)D}{\rho_l}} \tag{2.22}$$

As Equation 2.22 shows, the velocity of a bubble moving towards the surface varies with the density difference between the phases and the pipe diameter. The constant of 0.35 is the dimensionless Froude number.

Tung and Parlange (1976) studied large gas bubbles rising through a liquid in a vertical cylinder of large enough diameter resulting in a Reynolds number greater than 50 and neglected viscosity effects. The solution for the terminal rise velocity was a function of

surface tension, pipe diameter, gravity and liquid density and is presented as a Froude number given by Equation 2.23.

$$Fr = \frac{v_t}{\sqrt{gD}} = \left(0.136 - 0.944\frac{\sigma}{\rho g D^2}\right)^{1/2}$$

(2.23)

If interfacial tension effects are neglected, Equation 2.23 reduces to Fr=0.369, which is similar to the Froude numbers presented in Table 2.20.

Joseph (2003) came up with an equation for the terminal velocity for a spherical cap bubble in a vertical flow that also included viscosity, surface tension and the shape of the bubble-nose. The effect of surface tension is neglected if the bubble nose is spherical since the surface tension balances the static pressure difference in a sphere or spherical cap. The bubble-rise velocity given by Joseph (2003) is presented in Equation 2.24 for $\sigma = 0$. For increasing liquid viscosity that is larger than the value of gravity, the terminal rise velocity will decrease.

$$v_t = -\frac{4}{3}\frac{\mu}{\rho_l r} + \sqrt{\frac{4}{9}gr + \frac{16}{9}\frac{\mu^2}{(\rho_l r)^2}}$$

(2.24)

where r is the radius of the bubble-cap.

According to Jeyachandra et al. (2012) it is observed from experiments that the radius of a Taylor bubble is around 0.55 to 0.6 times the radius of the pipe. Jeyachandra et al. (2012) also states than an increase in pipe diameter gives an increase in the terminal velocity.

When operating in the churn-turbulent flow regime, the bubble swarm flowing can consist of both small and large bubbles. This is presented in Figure 2.22. The size of the small bubbles are in the range of 3-6 mm and can be either spherical or ellipsoidal depending on the properties of the liquid the swarm is moving through (Krishna et al., 1999). The large bubbles have a size between 20-80 mm and vary with coalescence and break-up.
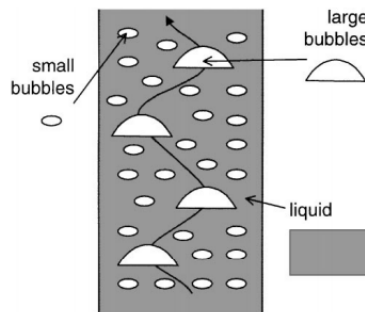
Figure 2.22: Churn-turbulent flow regime (Krishna et al., 1999).

According to Krishna et al. (1999), the bubble swarm consisting of large bubbles can have a velocity that is 3-6 times higher than that of a single isolated bubble. This velocity has

been estimated by introducing two correction factors to the terminal rise velocity for an isolated spherical cap bubble estimated by Davies and Taylor (1950b). The experimental data used to validate this estimate had Eötvös numbers greater than 40, which means that the bubble shape has a spherical cap.

$$V_b = 0.71\sqrt{gd_e}(SF)(AF) \tag{2.25}$$

where (SF) is the scale correction factor that takes the column diameter into account and (AF) is the acceleration factor that accounts for the velocity increase caused by the interaction with the wake (Krishna et al., 1999). The scale correction factor is a function of the bubble diameter to the column diameter given by Equation 2.26.

$$\lambda = \frac{d_e}{D} \tag{2.26}$$

Collins (1967) gives a relation for the scale correction factor and different values of λ, which is presented below.

$$SF = 1 \, for \, \frac{d_e}{D} < 0.125$$

$$SF = 1.13e^{\frac{-d_e}{D}} \, for \, 0.125 < \frac{d_e}{D} < 0.6$$

$$SF = 0.496\sqrt{D/d_e} \, for \, \frac{d_e}{D} > 0.6$$

The drag force acting on the bubble will be greater in a column of smaller width due to higher liquid velocity near the bubble (Krishna et al., 1999) meaning that the bubbles will rise faster in a wider column.

Collins (1967) relation is in agreement with Clift et al. (2005), but is more conservative with the limits of λ. Clift et al. (2005) states that for small bubbles resulting in values of $\lambda <0.3$, the wall causes minor deformation of the bubble. For larger bubbles giving values of λ greater than 0.6 the wall has a dominant effect on the shape of the bubble and reduces the terminal velocity.

The acceleration factor was found by analysing video recordings of two bubbles interacting to linearly increase as the vertical distance between two bubbles decreases (Krishna et al., 1999). The trailing bubble will get sucked into the wake of the leading bubble and experience an accelerated rise velocity. Figure 2.23 shows how two bubbles starting at two different vertical and horizontal positions interact before coalescing. The trailing bubble will align vertically with the leading bubble before merging. The closer the trailing bubble gets to the leading bubble, the acceleration effect will increase. This effect is weaker for bubbles in highly viscous fluids.
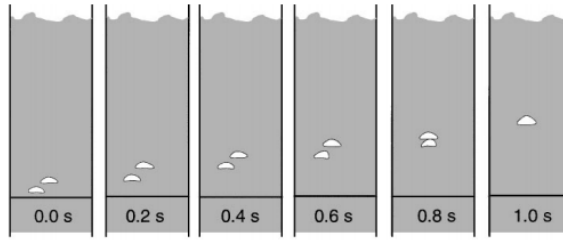
Figure 2.23: The rise trajectory of two bubbles with a diameter size of 47 mm which are initially separated 0.1 m horizontally and 0.07 m vertically. D=0.63 m. (Krishna et al., 1999).

Flow and physical properties of the surrounding liquid and interfacial properties between the gas and the liquid phase affect the rise characteristics of a bubble. Surface tension and viscosity of the liquid affects the rise velocity for small bubbles and have little effect on larger bubbles according to Fan (1998). For larger bubbles, the density difference between the liquid phase and the gas phase plays an important role when determining the rise velocity.

For bubbles with Eo >40 and Re >1.2, the interfacial tension forces are ignored and the flow is only considered in the area around the nose of the bubble. According to Clift et al. (2005) the terminal velocity for skirted bubbles with Re >40 is given by Equation 2.27, where r is the radius of the sphere or spherical cap.

$$v_t = \frac{2}{3}\sqrt{\frac{gr(\rho_l - \rho_g)}{\rho_l}} \tag{2.27}$$

Clift et al. (2005) also presented a terminal velocity for Taylor bubbles with Reynolds number larger than 150 and Eötvös number greater than 40, presented by Equation 2.28.

$$v_t = 0.711\sqrt{\frac{gd_e(\rho_l - \rho_g)}{\rho_l}} \tag{2.28}$$

According to Lyons et al. (2015), gas migration in a shut-in well can be estimated with Equation 2.29.

$$R_{GM} = 12e^{-0.37\rho_{mud}} \tag{2.29}$$

where R_{GM} is the rate of gas migration in ft/s and ρ_{mud} is the mud density in ppg.

2.4.4 Gas Migration Velocity as Function of Pressure and Temperature

The ideal gas law is given by Equation 2.30.

$$PV = nRT_K \tag{2.30}$$

P is pressure in Pascal, V is volume in m^3, n is mole, R is the Boltzmann constant of 8.314 $J/molK$ and T_K is the temperature in Kelvin.

Volume is given by:

$$V = \frac{m}{\rho}$$

Mole is given by:

$$n = \frac{m}{M}$$

where M is the molar mass in $kg/mole$.

By manipulating Equation 2.30 and using the relationships above to substitute volume and mole, an equation for calculating the density of an ideal gas for different pressures can be made, see Equation 2.31.

$$\rho_g = \frac{PM}{RT_K} \tag{2.31}$$

Gas density increases for increasing pressures and is reduced for increasing temperatures.

Krishna et al. (1994) used data from Figure 2.24 to study the pressure effect on the terminal rise velocity and came to the conclusion that for gas densities over the interval of 0.1-30 kg/m^3, the terminal rise velocity does not depend on the gas density. The data in Figure 2.24 is based on work by Krishna et al. (1994), Krishna (1992), Koetsier et al. (1976) and Wilkinson (1991). The conclusion is presented in Figure 2.25 and is for a limited range of pressures. Data from Krishna et al. (1994), Krishna (1992), Koetsier et al. (1976) are for a pressure of 1 $bara$, while the data from Wilkinson (1991) are for pressures of 10, 15 and 20 $bara$.

Exp. Data Source	Column Dia. (m)	Liquid Phase	Ungassed Liquid Height (m)	Gas Phase	Pre. (bar)	Gas Distributor
This work	0.1 (0.05)	water	2.4 (1.2)	He	1	sintered plate
This work	0.05	water	1.2	50% He + 50% Air	1	sintered plate
This work	0.1 (0.5)	water	0.6, 1.2, 2.4 (1.2)	Air	1	sintered plate
This work	0.1 (0.05)	water	1.2 (1.2)	50% Air + 50% Ar	1	sintered plate
This work	0.1 (0.05)	water	1.2 (1.2)	Ar	1	sintered plate
This work	0.1 (0.05)	water	1.2 (1.2)	SF_6	1	sintered plate
Krishna (1992)	0.63	water	4	N_2	1	sparger
Koetsier et al. (1976)	0.05	water	0.6	He	1	sintered plate
Koetsier et al. (1976)	0.05	water	0.6	Ar	1	sintered plate
Wilkinson (1991)	0.16	water	1.5	N_2	10	sparger
Wilkinson (1991)	0.16	water	1.5	N_2	15	sparger
Wilkinson (1991)	0.16	water	1.5	N_2	20	sparger

Figure 2.24: Experimental data (Krishna et al., 1994), (Krishna, 1992), (Koetsier et al., 1976) and (Wilkinson, 1991).
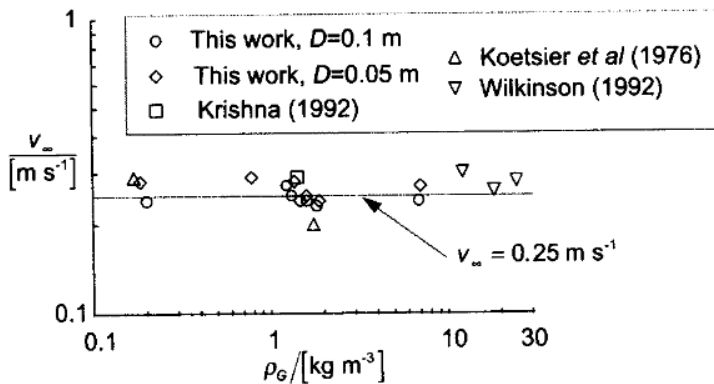
Figure 2.25: Single bubble rise velocity as a function of gas density (Krishna et al., 1994).

Lin et al. (1998) performed experiments where the pressure and temperature effect on the terminal rise velocity were investigated. Nitrogen was used for the gas phase and the stable organic liquid, paratherm NF heat transfer fluid was used as the liquid phase. This liquid has a high density (880 kg/m^3 for a temperature of 15.5°C) and a viscosity of 17 cP.

Pressure and temperature change the physical properties of the fluids. Properties like density, viscosity and surface tension were measured in-situ by using different methods. The operating condition included pressures ranging from 10-194 bar for three different temperatures; 27°C, 47°C and 78°C. Direct visualization was used to investigate the bubble behaviour and the terminal rise velocity was calculated using the time it took the bubble to travel a certain distance. The results from the experiment showed that the liquid density increased when the pressure increased but decreased for increasing temperature for the

entire pressure range. The viscosity increased by 65% for increasing pressures with constant temperature of 293 K. When the temperature increased to 373 K, the viscosity only increased by 10% for the same pressure increase. The results show that temperature have a greater effect on viscosity than pressure. The results also showed that temperature has a greater effect on the surface tension compared to pressure. The surface tension decreases with approximately 4% for every temperature increase of 10 K.

The terminal rise velocity was calculated for pressures ranging from 10-194 bar and temperatures of 27°C, 47°C and 78°C and the results are presented in Figure 2.26.

(a) Terminal rise velocity for 27°C.   (b) Terminal rise velocity for 78°C.
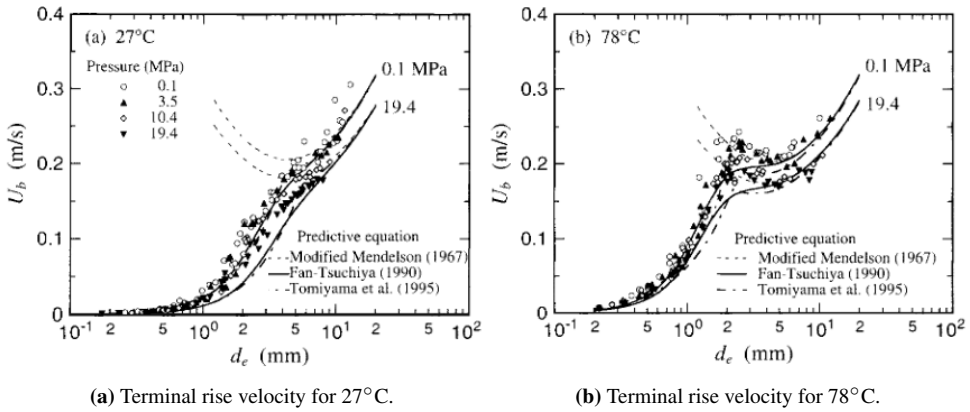
Figure 2.26: Effect of pressure on the terminal rise velocity of single bubbles in paratherm NF heat-transfer liquid for 27°C and 78°C (Lin et al., 1998).

Both Figure 2.26a and 2.26b show that the terminal rise velocity decreases for increasing pressures. The figure also includes three predictive equations that is used to compare the experimental result. These include the Mendelson's wave-analogy equation for gas bubbles rising in low-viscosity liquids, Mendelson (1967) modified by Maneri (1995), the Fan-Tscuchiya correlation (Liang-Shih and Tsuchiya, 2013) and the Tomiyama correlation (Tomiyama, 1995). The Fan-Tscuchiya correlation presented in Equation 2.32 which is written in dimensionless form correlates well with the experimental results.

$$v_{t'} = v_t \left(\frac{\rho_l}{\sigma g}\right)^{1/4} = \left\{ \left[\frac{Mo^{-1/4}}{K_b}\left(\frac{\Delta\rho}{\rho_l}\right)^{5/4}d_b'^2\right]^{-n} + \left[\frac{2c}{d_b'^2} + \left(\frac{\Delta\rho}{\rho_l}\right)\frac{d_b'^2}{2}\right]^{-n/2} \right\}^{-1/n}$$

(2.32)

The dimensionless bubble diameter is given by Equation 2.33 and the Morton is given by Equation 2.34.

$$d_b' = d_b\sqrt{\left(\frac{\rho_l g}{\sigma}\right)}$$

(2.33)

$$Mo = \frac{g\Delta\rho\mu_l^4}{\rho_l^2\sigma^3}$$

(2.34)

Equation 2.32 uses three empirical parameters, n,c and K_b. These parameters reflect three factors that influence the terminal rise velocity. n relates to the contamination level of the liquid phase, c relates to the varying dynamic effects of surface tension and K_b represents the viscous nature of the surrounding medium and is presented in Equation 2.35 (Lin et al., 1998). The parameters are presented below.

$$n = \begin{cases} 0.8 & \text{for contaminated liquids} \\ 1.6 & \text{for purified liquids} \end{cases}$$

$$c = \begin{cases} 1.2 & \text{for monocomponent liquids} \\ 1.4 & \text{for multicomponent liquids} \end{cases}$$

$$K_b = max(K_{b0}Mo^{-0.038}, 12) \tag{2.35}$$

where

$$K_{b0} = \begin{cases} 14.7 & \text{for aqueous solutions} \\ 10.2 & \text{for organic solvent/mixtures} \end{cases}$$

2.4.4.1   The Effect of Viscosity on the Terminal Rise Velocity

Jeyachandra et al. (2012) state that a reduction in viscosity gives an increase in the terminal rise velocity. The resistance of the gas bubble to intrude into the stagnant liquid increases with increasing liquid viscosity and results in a lower rise velocity. According to Jeyachandra et al. (2012) a lot of the correlations for the terminal velocity of a bubble is neglecting effects of surface tension and viscosity. Viscosity,in particular, is known to play a huge impact on the terminal velocity. It is especially important to include the effect of viscosity when using other liquids than water.

Kjølaas et al. (2017) have another opinion on how the viscosity affects the migration velocity. In high-viscosity liquids, swarms of small bubbles can according to Kjølaas et al. (2017) migrate faster than in a low-viscosity liquid ($\mu < 2cp$). Bubbles coalescence more easily in a high-viscosity fluid compared to a low-viscosity fluid resulting in a lower drag force acting on the bubble which will result in a higher terminal rise velocity.

2.4.5   The OLGA Simulator

The first version of the dynamic two-phase-flow model OLGA was working in 1983 and was used to simulate transient flow in pipeline systems. Further development of OLGA was carried out as a joint research program between The Institute of Energy Technology at NTNU (IFE) and SINTEF, supported by different oil companies. The empirical basis of the model was extended and several new applications were added to the simulator (Bendiksen et al., 1991). The core of the two-phase model is based on conservation equations for mass and momentum that are discretized using finite difference formulation with

a staggered mesh (Rygg et al., 1992).

Saga Petroleum had a complicated underground blowout project in the North Sea in 1989 which required thorough planning of the kill strategy. At the time, no tool existed that dynamically could estimate kill fluid volumes and times for different kill points. This raised the need for an improved flow simulator (Rygg et al., 1992). The research team at Saga Petroleum used the two-phase flow model OLGA as a basis and specifically adapted it to well flow kill applications. The new simulator was named OLGA-WELL-KILL (Rygg et al., 1992). Today, the dynamic multiphase flow simulator OLGA-WELL-KILL is managed by Add Energy. The simulator has been applied on several blowout and well control incidents and is also used for contingency planning. Data from real incidents are used to verify and upgrade the simulator to ensure reliable and accurate results (Energy, 2019).

The simulator can be used to predict the gas migration velocity for a specific well and the corresponding pumping schedule that is necessary to overcome this velocity if gas influx occurs. The gas migration velocity depends on factors like flow regime, the density difference between the gas and the liquid in the well, the liquid viscosity, the surface tension, the size of the gas bubbles and the well inclination.

The simulator has built-in functions for the terminal rise velocity for different flow regimes since the velocity depends on the type of flow regime. To predict the flow regime, flow parameters need to be specified in the simulator. According to Bendiksen (1984), the terminal rise velocity for fully developed turbulent slug flow where the length of the Taylor bubbles is greater than 10D is given by Equation 2.21 for a vertical pipe. For pure bubble flow in vertical pipes, the terminal rise velocity is given by Equation 2.36 according to Malnes (1979) (Bendiksen et al., 1991).

$$v_t = 1.18 \sqrt[4]{\frac{g\sigma(\rho_l - \rho_g)}{\rho_l^2}} \tag{2.36}$$

The simulator is also fed with well data from the operator company such as PVT tables (drilling fluid and gas composition), thermodynamic properties of the well, formation properties like porosity and fracture pressure and operational data.

3 | Experimental Methodology

3.1 Introduction to the Experiments

In the project report "An Experimental Study of Gas Migration in Pressurized Fluids" by Tønnessen (2018) the experiments were performed with a high-pressure non-transparent steel cylinder tank. The apparatus used in the experimental setup was designed to represent a length-interval of a closed well downhole without the presence of a drill pipe. Water was used as the drilling fluid and the gas kick was simulated by injecting nitrogen gas in the bottom of the cylinder tank. The objective was to estimate the gas migration velocity of the injected gas for different pressure regimes. To be able to calculate the gas migration velocity from these experiments, the time it took the first bubbles to reach the top of the tank had to be measured. This was done by interpreting the pressure response from the setup. Due to uncertainty in this interpretation, it was decided to perform the initial experiments in this thesis with a low-pressure transparent apparatus to visually verify when the first bubbles had reached the top of the apparatus and what kind of pressure response this would give. The intention was to continue with experiments in the non-transparent high-pressure cylinder tank after the pressure response had been verified, but due to difficulties with some setup components, this was not possible. The Department of Chemistry had a similar set-up with a high-pressure transparent cylinder tank that was pressure rated to 60 $barg$, which this thesis got permission to use. Section 3.2.1 elaborates about the experiments performed with the low-pressure transparent cylinder tank, what challenges that arose, modifications of the setup, interpretation of the pressure response and simulation results. Section 3.2.2 presents the high-pressure transparent cylinder cell and its setup and includes the procedure and test conditions.

Figure 3.1 illustrates the initial setup with the non-transparent high-pressure cylinder tank presented by Tønnessen (2018).
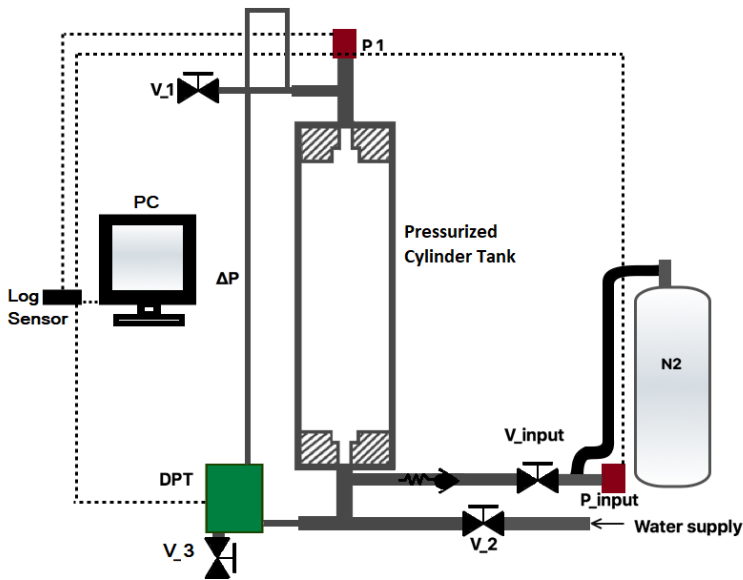
Figure 3.1: Schematic of high-pressure non-transparent apparatus.

Several modifications on the experimental setup have been performed in addition to changing the cylinder tank to a transparent one. These modifications include adding an additional pressure sensor to the setup and inserting a meshed gas bubble distributor slightly above the bottom of the tank. The low-pressure transparent setup is illustrated in Figure 3.2 in section 3.2.1.

3.2   Experimental Setup

3.2.1   Low-Pressure Transparent Apparatus

The experimental setup consists of a nitrogen gas tank that supplies a low-pressure transparent cylinder tank containing water with pressurized gas bubbles. The first experiments were performed with the setup illustrated in Figure 3.2. The low-pressure transparent apparatus was supposed to be as similar as possible to the non-transparent high-pressure apparatus illustrated with Figure 3.1 in dimensions and setup. Figure 3.3 shows a schematic of the low-pressure transparent cylinder with its dimensions. During the process, it has been necessary to make modifications of the initial transparent setup.
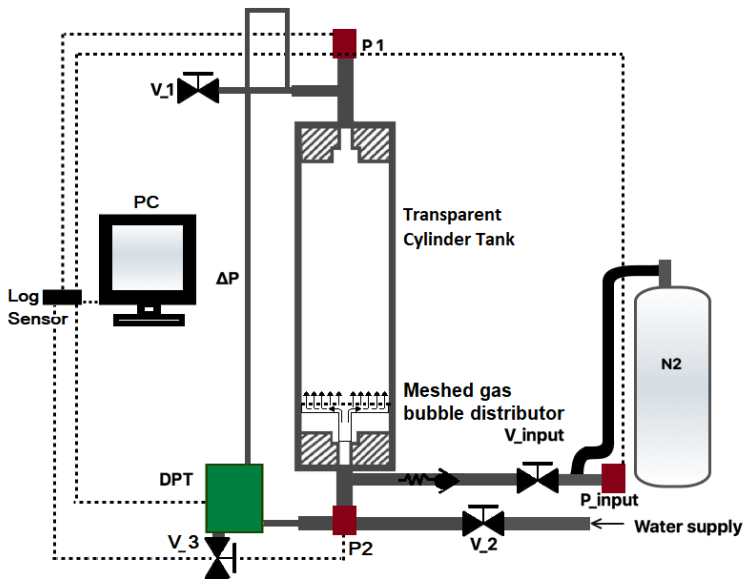
Figure 3.2: Schematic of the initial low-pressure transparent apparatus.

A	V_1	10.6	ml
B	ID_1	63	mm
C	ID_2	10.8	cm
D	OD	15.4	cm
E	L_1	25.5	mm
F	L_2	89.6	cm
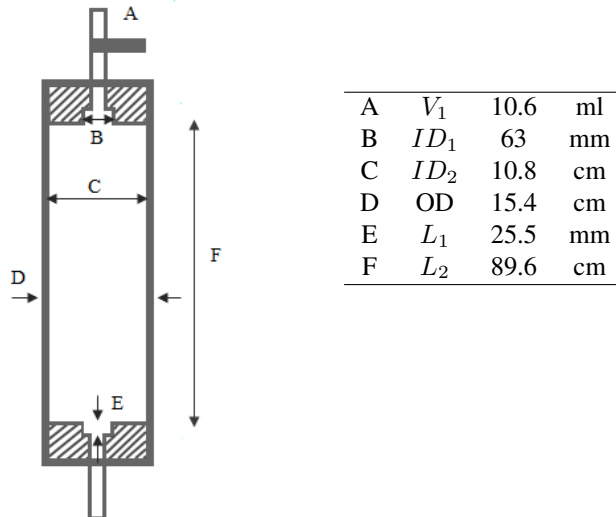
Figure 3.3: Schematic and dimension of the low-pressure transparent cylinder tank.

The experimental setup is equipped with three pressure sensors, P_1, P_2 and P_{inlet}, all having an operating pressure range of 0-6 $barg$. The low-pressure transparent pipe is

pressure-approved to 6 $barg$ unlike the high-pressure pipe, which could stand a pressure of 690 $bara$. Since the apparatus is connected to a nitrogen gas tank that can hold pressures up to 300 $bara$, the apparatus is equipped with a safety valve to avoid any incidents. This valve is located on the hose connecting the nitrogen tank and the valve, V_{inlet}. The relief valve allows a maximum gas inlet pressure of 3 barg to enter the transparent pipe.

The nitrogen gas is supplied through a 100 ml tube and the gas flow rate is controlled by two valves. The first valve is a ball valve called V_{inlet} that allows the injection of gas when opened. The second valve is a one-way-valve preventing water from entering the gas tube. This one-way-valve consists of a spring that needs some over-pressure to work. There is a pressure sensor, P_{inlet}, located on the gas tube so that it is possible to determine the pressure of the gas in the tube before injection. To get the desirable inlet pressure of the gas there is an adjustable regulator on the Nitrogen gas tank. The cylinder tank is supplied with water through a valve called V_2. Two pressure sensors determine the pressure in the cylinder tank. One is recording the pressure at the bottom of the tank, P_2, and the other records the pressure at the top of the tank, P_1. There is also a differential pressure transmitter, DPT, that gives the differential pressure between the bottom and the top of the cylinder. The differential pressure transmitter records pressure differences between 0-0.25 $barg$ with an accuracy of $\pm 0.075\%$ of the calibrated range. Two lines are connected to the DPT. The upper line is filled with air and measures the pressure at the top of the tank and the lower line is connected to the bottom of the tank and is filled with water. To prevent water from entering the upper line when performing the experiments, an elongation of the upper line was installed together with a U-tube. To be able to bleed the upper line of water there is a valve called V_3 on the DPT. During the experiments, a logging system receives the data from the pressure sensors and stores it as a txt.-file on a computer using a program called Lab-View. On top of the cylinder tank, there is another valve named V_1, which can equalize the pressure in the tank by releasing trapped gas and water to the atmosphere after finishing an experiment to reset the system.

3.2.1.1 Experimental Procedure

The low-pressure transparent pipe was filled with water by opening valve V_2 and allowing water from the water supply to flow into the cylinder. Valve V_1 was also open when filling the tank so that water could flow out from this valve and indicate when the cylinder tank was completely filled with water. Some air bubbles were still present in the tank, which made it possible for the Nitrogen gas to be injected into the tank at a later stage. The experiment was performed in a closed environment, so all valves (V_1, V_2, V_3 and V_{input}) were closed before allowing the gas tube to be filled with Nitrogen gas. Before opening the main valve on the gas tank, Lab-View was started and the pressure recordings were used to decide the inlet pressure in the gas tube. The regulator on the Nitrogen tank was adjusted to get the desired pressure of the inlet gas based on the recorded data. The gas tank was then closed and the experiment began by opening V_{input}. After the gas volume had migrated to the top of the tank and the experiment was finished, V_1 was opened to equalize the system.

The experiments were performed with a differential pressure of 0.9 $barg$ between the inlet

gas pressure, P_{inlet} and the bottom hole pressure in tank, P_2. For experiments performed with inlet pressure, P_{inlet}, higher than $1\ barg$, the transparent pipe was pressurized to maintain the differential pressure between the inlet gas and the tank. This was performed after filling the tank with water by opening V_{inlet} and using the regulator on the Nitrogen tank to get the desired pressure in the tank based on the pressure data presented in Lab-View. V_{input} was then closed and the gas tube was pressurized to the desired pressure before initiating the experiment by opening V_{inlet} and allowing the gas to enter the cylinder tank and migrate to the top.

Due to a transparent apparatus, it was possible to record the bubble migration with a video-camera and decide the time it took the bubbles to reach the top of the tank and the corresponding rise velocity by subsequent frame-by-frame analysis. These results were compared to the interpretation of the pressure response.

3.2.1.2 Pressure Response Principle for the Differential Pressure Transmitter

The differential pressure in the cylinder tank recorded by the differential pressure transmitter when the upper line is filled with air and the bottom line is filled with water is given by Equation 3.1.

$$\Delta P = P_{bottom} - P_{top} = (P_1 + \rho_w g h_w + \rho_g g h_g) - P_1 = \rho_w g h_w + \rho_g g h_g \qquad (3.1)$$

It is expected that the differential pressure when the bubble has reached the top of the tank and the system stabilizes is more or less equal to the differential pressure before the test started. The total pressure in the system will be higher after the injection of gas, but the differential pressure between the top and bottom should still be given by the water column. This is because the hydrostatic contribution from the gas on the hydrostatic pressure is almost negligible for the volume of gas that has been injected in this experiment.

3.2.1.3 Limitations and Modifications of the Setup

Even with the upper line of the DPT installed as a U-tube, water from the experiment was still influencing the differential pressure response, making it difficult to interpret when the gas bubbles had reached the surface based on the pressure data. Several attempts to avoid getting water into the upper line have been made. A solution to this problem was to fill the upper line with water and isolating it from the system with a three-way valve during the experiments and use it as a reference point. Figure 3.4 illustrates this solution.
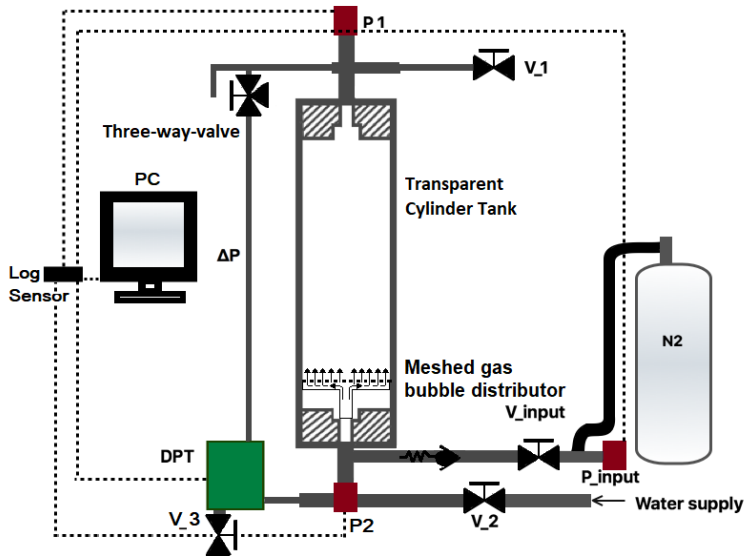
Figure 3.4: Schematic of the modified apparatus with upgraded DPT.

Since there now was water on both sides of the DPT, the only pressure difference before the initiating the experiment would be the difference in height of the water columns that they recorded. This is illustrated in Figure 3.5a. When performing the experiments, the pressure in the lower line would increase due to gas contributing to a higher pressure at the top of the tank, giving a higher differential pressure. An indication that the gas bubbles had reached the top of the tank should be given by a stabilization of ΔP at a higher pressure value than prior to the experiments. Equation 3.2 and 3.3 gives the differential pressure at t=0 and t=1, which is before and after the experiment, respectively. Figure 3.5a and 3.5b illustrate the scenario before and after the experiment.

$$\Delta P_{t=0} = P_{lower} - P_{upper} = \rho_w g(h_{lower} - h_{upper}) \tag{3.2}$$

$$\Delta P_{t=1} = P_{lower} - P_{upper} = P_1 + \rho_g g h_g + \rho_w g(h_{lower} - h_{upper}) \tag{3.3}$$

(a) Before experiment, t=0.   **(b)** After experiment, t=1.
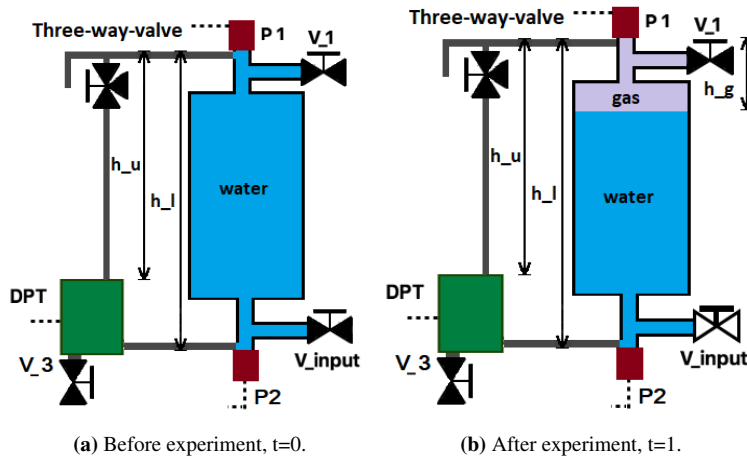
Figure 3.5: Illustration of what the DPT records before and after an experiment.

For tests performed with higher inlet pressures than 1 $barg$ which required a pressurized cylinder tank to keep the pressure margin at 0.9 $barg$, the three-way valve was opened so that the whole system including the upper-line of the DPT could be pressurized. This had to be done to avoid damage on the DPT cell which can only record pressure difference between 0-0.25 $barg$. Before injecting the inlet gas and performing the experiment, the three-way-valve was closed so that it could still be used as a reference point. When the experiment was finished, the system was equalized by opening V_1. To avoid damaging the DPT, the three-way-valve had to be opened before equalizing the system.

The DPT was calibrated and showed a stable and correct value of ΔP when the system was closed and the three-way-valve was opened so that it was communication between the upper and lower line. When the three-way-valve, on the other hand, was closed and the system was ready for an experiment, ΔP would not stabilize and fluctuated constantly. The diameter of the upper and lower lines was $1/8$". When the upper line was isolated from the rest of the system, the temperature was reduced and influenced the pressure recordings. A mitigating action to this problem was to increase the diameter of the lines to $1/4$", but the pressure recordings still fluctuated so the differential pressure transmitter was removed from the setup.

Deciding the rise velocity of the bubbles was instead performed by analyzing the pressure response from P_2. This relied on an accurate pressure sensor that was able to record the small changes in pressure response from the system. P_2 had initially a pressure range of 0-6 $barg$ and an accuracy of 0.2%, which corresponds to an error of $\pm$ 0.012 $barg$. To make sure the pressure response was recorded with P_2, this sensor was changed to a more accurate sensor with a pressure range from 0-2.5 $barg$. The new setup is illustrated in Figure 3.6.
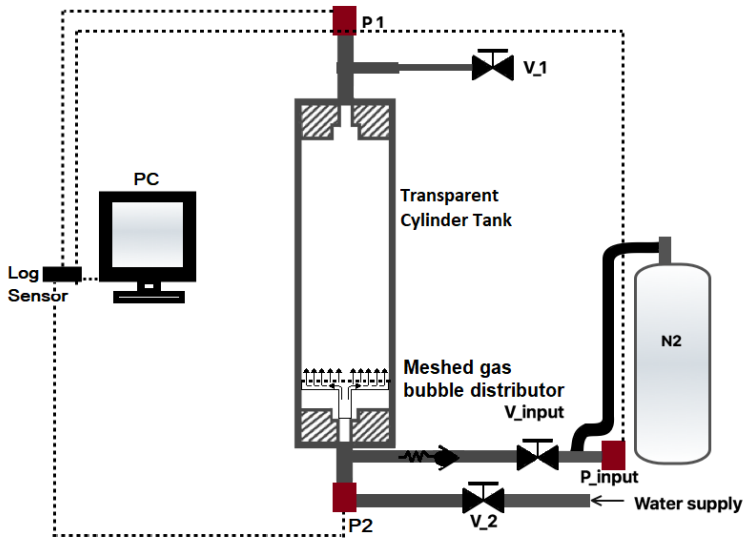
Figure 3.6: Schematic of the modified apparatus without DPT.

3.2.1.4   Pressure Response Principles

Figure 3.7a, 3.7b, 3.7c and 3.7d give a snapshot of the situation in the cylinder at differ-
ent times during the experiment. The pressure scenarios for the different situations are
described below. It is assumed that the pressure contribution from the gas column on the
hydrostatic pressure in the cylinder is neglected due to a very short gas column. $P_{gas_{influx}}$
is the pressure that the influx gas has when entering the cylinder.

(a) No influx.

(b) Gas influx in the bottom of the cylinder.

(c) Gas in the middle of the cylinder.

(d) Gas at the top of the cylinder.
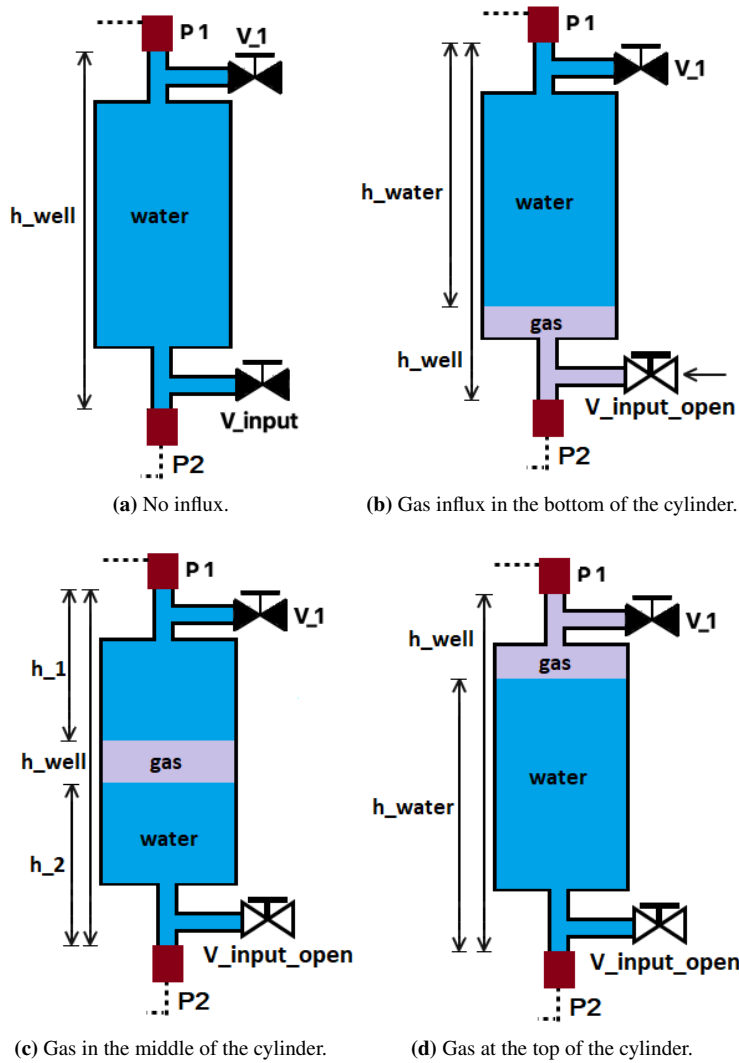
Figure 3.7: Snapshots of the situation in the cylinder at different times during the experiment.

Case a) Only water in the cylinder:

$$P_1 = 0$$

$$P_2 = \rho_{water} g h_{well}$$

Case b) Gas influx located at the bottom of the cylinder:

$$P_1 = P_{gas_{influx}} - \rho_{water} g h_{water}$$

$$P_2 = P_{gas_{influx}}$$

Case c) Gas influx has migrated to the middle of the cylinder

$$P_1 = P_{gas_{influx}} - \rho_{water}gh_1$$
$$P_2 = P_{gas_{influx}} + \rho_{water}gh_2$$

Case d) Gas influx has reached the top of the cylinder

$$P_1 = P_{gas_{influx}}$$
$$P_2 = P_{gas_{influx}} + \rho_{water}gh_{water}$$

3.2.1.5   Interpretation of Pressure Recordings

Figure 3.8 shows the pressure recordings from an experiment where the cylinder was pressurized so that P_2=1.1 $barg$ and P_{inlet}=2 $barg$ prior to the experiment. Figure 3.9 shows a close-up of the pressure response when the experiment was performed. This experiment was also recorded with video so that the time it took the bubbles to reach the top of the tank could be visually verified.
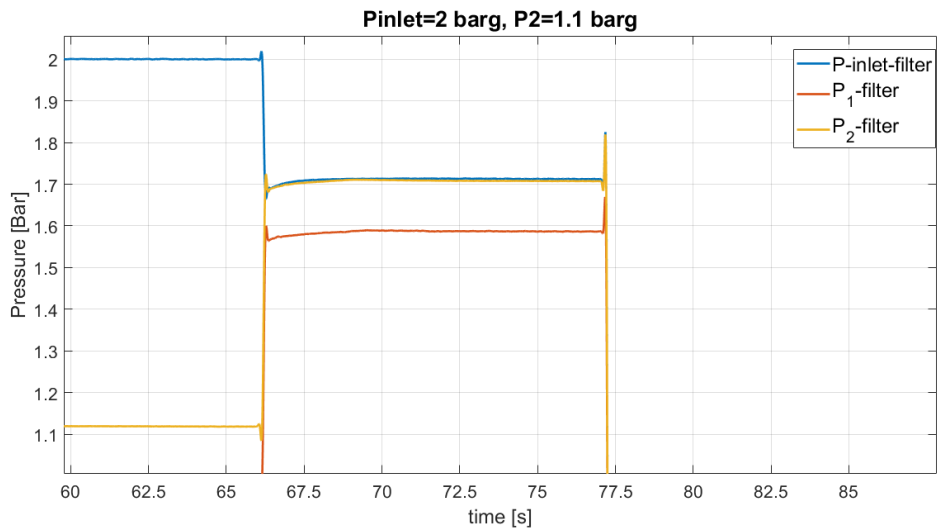
Figure 3.8: Pressure recordings from an experiment performed with P_{inlet}=2 $barg$ and P_2=1.1 $barg$.
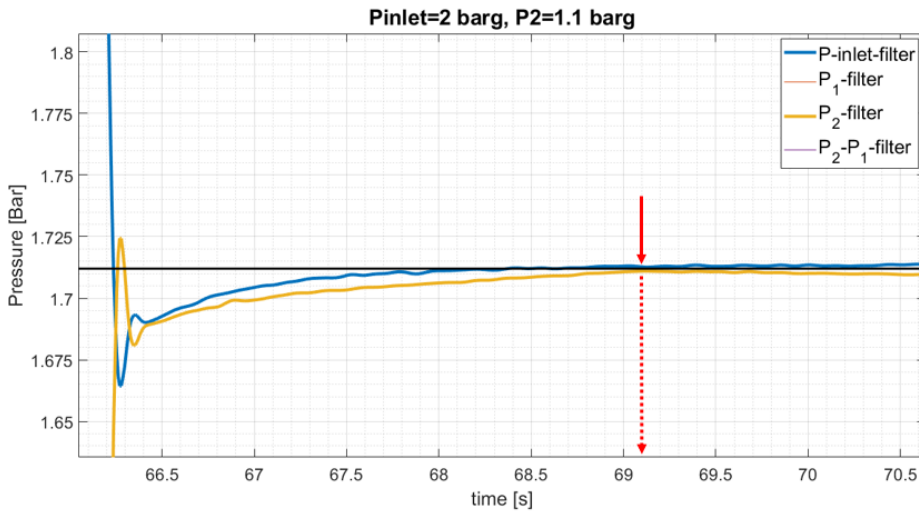
Figure 3.9: Close up of the pressure recording from an experiment performed with P_{inlet}=2 $barg$ and P_2=1.1 $barg$ showing the response of P_{inlet} and P_2.

P_{inlet}, which is illustrated as the blue line, have a drop at around 66 s, which indicates the time when V_{inlet} was opened and the experiment had started. Straight after, the blue line has a low point at the same time as the yellow line, which illustrates P_2, is at a maximum. This can be a response to when the one-way-valve between P_{inlet} and P_2 closes. P_2 is then greater than P_{inlet}. Due to stagnant conditions in the gas tube, P_{inlet} increases to a value greater than P_2 and the one-way-valve opens for a short period, which is indicated by the maximum for the blue line and the corresponding low point for the yellow line. The movement of gas between P_{inlet} and P_2 is stagnant from this point and forward. This is shown as a constant slightly higher value for P_{inlet} than for P_2. Figure 3.9 shows that P_2 increases gradually until a point where it is tangent to the black line. This corresponds to the time on the video when the first bubbles have reached the top of the cylinder tank. This corresponds to the theory presented earlier in 3.2.1.4. After this point, P_2 levels off with a slight decrease. This can be due to a thermal effect.

3.2.1.6   Future Work with the Initial Setup

The intention was to change over to the setup with the high-pressure non-transparent cylinder tank once the interpretation of the pressure response was verified. Due to limitations with this setup, it was difficult to trust the results from the pressure sensors and therefor also the interpretation of the pressure recordings. These limitations and suggestions to future improvements have been presented in this section. For this thesis, it was decided to not continue with experiments at higher pressures in the high-pressure non-transparent cylinder tank due to these uncertainties. Experiments were instead performed with the setup described in Section 3.2.2 for experiments with higher pressures and the results from these

experiments are presented in Chapter 4.

The pressure sensors used for the setup is not accurate enough for the pressure response that they are supposed to record. A more precise instrumentation is recommended for the setup. Since the experiment is supposed to be performed for varying pressure regimes, additional pressure sensors that are accurate for different pressure intervals are needed.

The height of the cylinder tank is $0.896\ m$, which corresponds to a hydrostatic pressure of $0.088\ barg$ recorded at the bottom of the tank with P_2. Injecting gas into this system will give a pressure response, but due to the short travel length for the bubbles, the pressure response will happen quite fast. With a taller cylinder tank, the length the bubble have to travel will increase and can result in a more distinct pressure response.

The pressure response measured by P_2 seems to be influenced by when the one-way-valve located between P_{input} and P_2 opens and closes. This valve only allows gas flowing from the gas tank to the system with some overpressure and stops water from entering the hose. A suggestion to a change in the setup for the injection of gas is presented with the illustrations in Figure 3.10. Figure 3.10a, 3.10b, 3.10c and 3.10d illustrate a snapshot of the setup at different times during the injection of gas. Figure 3.10a shows the setup when it has been filled with water. In Figure 3.10b, V_{new} and V_{input} is closed and V_2 is opened so that the volume of water between the valves can be drained. Figure 3.10c illustrates two closed valves and an open V_{input}, so that the gas can be supplied to the volume between the valves. V_2 and V_{input} is closed in Figure 3.10d and V_{new} is opened to allow gas to enter the cylinder tank and initiating the experiment.

The gas volume to be injected in the proposed new setup will start to compress when V_{new} is opened due to the water on top of the valve being subjected to gravity and pushing on the gas. After some time, the gas will start to rise due to density differences. The new setup would also neglect the jet-effect that the gas might be influenced by when V_{inlet} on the original setup illustrated by Figure 3.2 is opened.

(a) The cylinder has been filled with water and all valves are closed.

(b) The volume of water between V_{new} and V_2 is removed by opening V_2.

(c) Gas is supplied through V_{input} to the volume between V_{new} and V_2.

(d) V_{input} and V_2 is closed so that the experiment can be initiated by opening V_{new}.
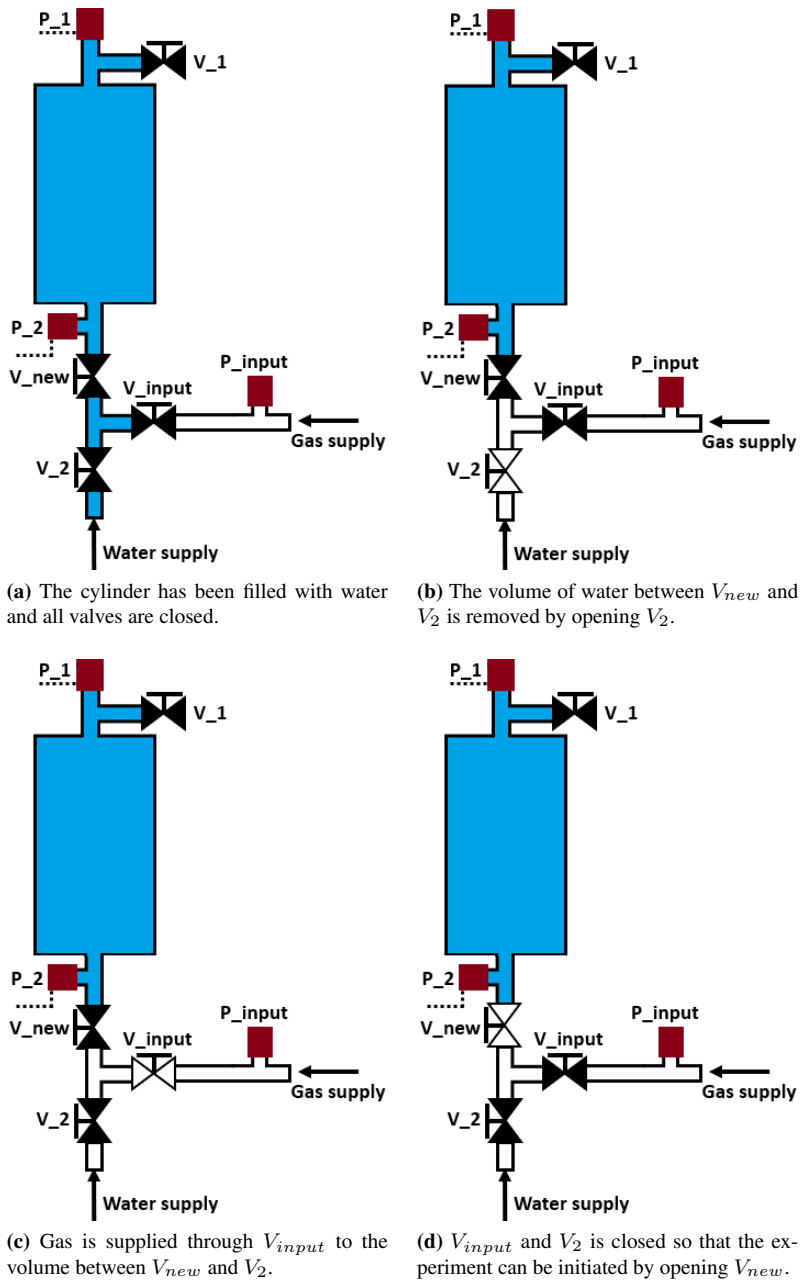
Figure 3.10: Snapshots of the setup at different times during the injection of gas.

3.2.1.7   Results from OLGA-WELL-KILL Simulations

AddWellFlow contributed with a gas migration velocity simulation using OLGA-WELL-KILL for different operating pressures for the setup presented in Section 3.2.1. Table 3.1 presents the results of the OLGA-WELL-KILL simulations provided by AddWellFlow.

The velocity values in Table 3.1 are based on when the first bubble has reached the top of the tank. OLGA-WELL-KILL assumed a distributed bubble flow. In the simulations, a closed one-way-valve separated the gas and the water. By opening this valve, gas was led into the system and the time it took the first bubble to reach the top of the tank was measured. The corresponding velocity could then be determined.

Table 3.1: Gas migration velocity at different cell pressures from simulations with OLGA.

Pressure $[barg]$	Gas Migration Velocity $[m/s]$
1	0.30
20	0.26
60	0.20

Due to limitations with the interpretation of the pressure response, it was not possible to perform experiments in the high-pressure non-transparent cylinder tank. Since the transparent apparatus had a pressure limitation of 3 $barg$, the simulated results for pressures of 20 and 60 $barg$ could not be compared with experimental ones.

A migration velocity of 0.30 m/s for a pressure condition of 1 $barg$ corresponds well with the results obtained for this setup.

The migration velocities presented in Table 3.1 shows that the gas migration velocity decreases for increasing pressure regimes.

3.2.2   High-Pressure Transparent Apparatus

The experimental setup is illustrated in Figure 3.11 and consists of a pressurized cell with an ID of 4 cm and a length of 24 cm. A gas tank that holds pressures up to 200 $barg$ supplies the cell with compressed Nitrogen gas. The gas flow through a flow controller, which detects the gas mass flow and presents it as a volume flow on a display. A back pressure regulator is used to adjust the pressure in the cell. The setup consists of different types of valves, which have been listed and described in Table 3.2. A high-speed imaging camera named Votron Ax 100 is used to image the bubbles and frame-by-frame analysis is used to determine the gas migration velocity. A LED light for high-speed imaging is placed behind the cell to be able to photograph the bubbles. A flow chart of the setup is presented in Figure 3.12 and the description of the different components are presented in Table 3.3.
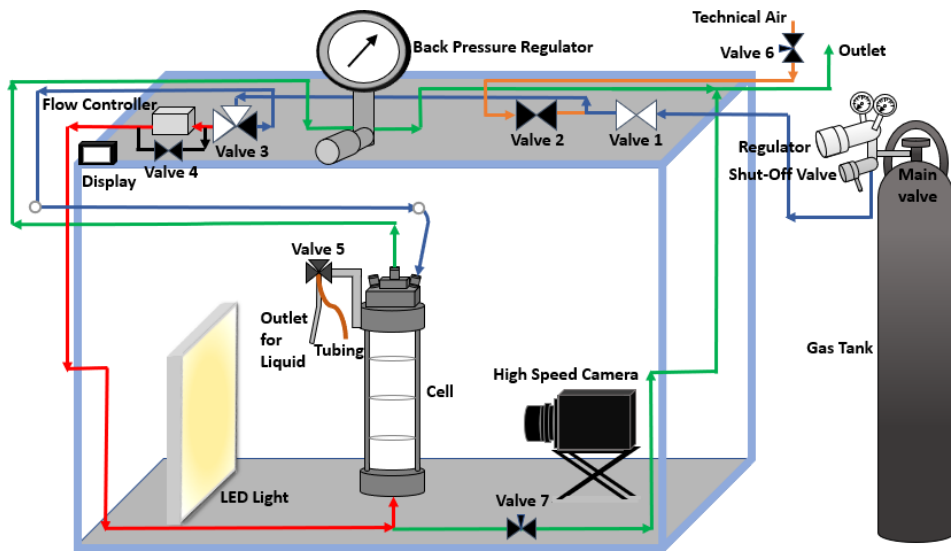
Figure 3.11: Illustration of the setup when gas is circulated through the bottom of the cell.

Table 3.2: A presentation of the different valves on the setup.

Name	Type	Description
Valve 1	Ball valve	Allows the flow of gas from the gas tank
Valve 2	Ball valve	Connected to the technical air system
Valve 3	Three-way-valve	Allows pressurizing of the cell or the supply of gas through the bottom of the cell
Valve 4	Ball valve	Bypass valve
Valve 5	Three-way-valve	For filling and emptying the cell of liquid
Valve 6	Needle valve	Regulates the flow of technical air
Valve 7	Needle valve	Depressurizes the gas supply line
Valve 8	Check valve	Allows flow in one direction
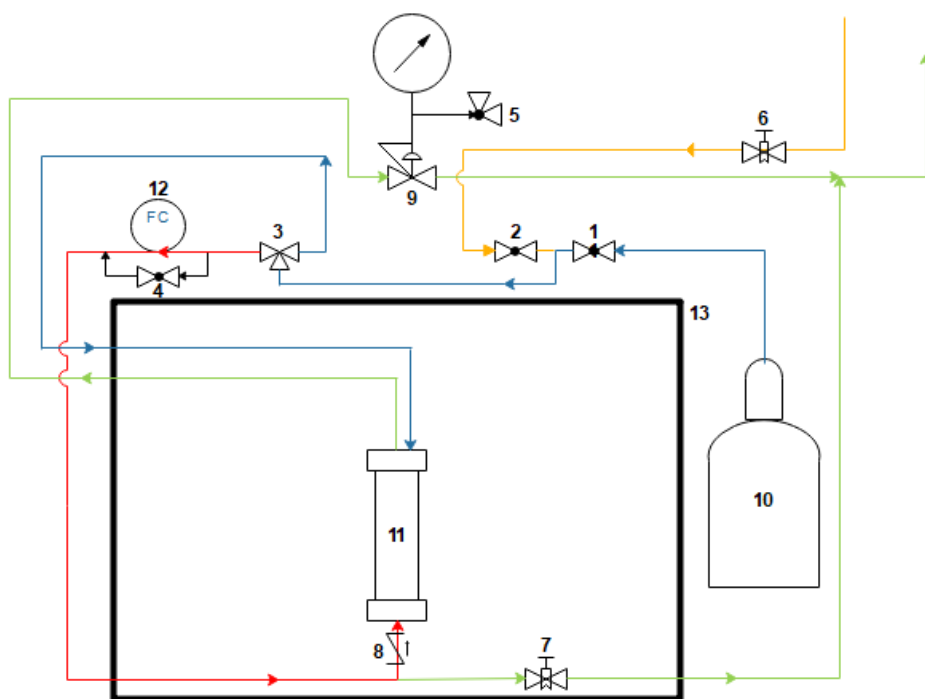
Figure 3.12: Flowchart of the setup.

Table 3.3: Description of the different flow chart components.

Number	Name
1	Valve 1
2	Valve 2
3	Valve 3
4	Valve 4
5	Safety relief valve
6	Valve 6
7	Valve 7
8	Check valve
9	Back Pressure Regulator
10	Gas tank
11	Cell
12	Flow controller
13	Oven

The blue line in Figure 3.12 describes the gas supply from the gas tank. This gas can either be used to pressurize the cell from the top or supply gas bubbles through the bottom of the cell. For both of these scenarios to occur, valve 1 needs to be open. Gas is then allowed to

flow towards valve 3, which is a three-way-valve. By turning valve 3 to the right, the top of the cell is pressurized. The backpressure regulator (BPR) is also connected to the cell via the green flow line and can regulate the pressure at the top of the cell to the desired test pressure. A safety relief valve is connected to the BPR and will start releasing pressure above 90 bara.

By turning valve 3 to the left, the gas will flow in the red flow line towards the bottom of the cell, either through the flow controller or via valve 4, which is a bypass valve. The check valve underneath the cell is a one-way-valve, making sure that there is only an upward flow from the red flow line.

Valve 7 is a needle valve which is closed during the experiments and only opened before the cell is being depressurized and cleaned. This flow line is linked up with the green flow line regulated by the BPR and this flow line ends at the outlet.

Valve 6 is also a needle valve that regulates the supply of technical air to the system, through the orange flow line. The technical air flow has to pass valve 2 before reaching valve 3 and either flow to the top of the cell with the blue flow line or flow to the bottom of the cell with the red flow line via the flow controller or valve 4.

3.2.2.1 Flow Controller

A high-performance mass flow controller for gases named EL-flow prestige FG-211-C have been used. The flow controller consists of an inlet port, an outlet port, a mass flow sensor and a proportional control valve. The input signal is compared to the value from the mass flow sensor and adjusted accordingly by using the control valve to get the required flow. It is suited for accurate measurement at operating pressures up to 100 $bara$ and flow ranges between 0.14-7 ml/min to 0.4-20 l/min. The flow controller measures the mass flow of gas and presents it on a display as a volume flow in ml/min. The conversion from mass flow to volume flow is given by Equation 3.4.

$$q = \dot{V} = \frac{\dot{m}}{\rho_{gas}} \tag{3.4}$$

The flow controller is calibrated for a pressure of 10 $barg$ and the corresponding Nitrogen density at this pressure. The flow controller measures the mass flow and converts it to volume flow by using a constant density. To account for the density difference, a correction factor is added to get the same volume flow condition for all experiments with different pressures. This means that the display will show different values of volume flow even if it is a constant volume flow. Since the flow controller is calibrated for a pressure of 10 $barg$, this is used as a reference point. The correction factor is given by Equation 3.5 and the corrected flow rate in ml/min is given by Equation 3.6. Table 3.4 shows the density of Nitrogen for different pressures and the corresponding density correction factor.

$$C_\rho = \frac{\rho}{\rho_{ref}} = \frac{\rho}{\rho_{P=10}} \tag{3.5}$$

$$q_{corrected} = q_{constant} \cdot C_\rho \tag{3.6}$$

Table 3.4: Nitrogen density at T=25°C for different pressures and density correction factor

Pressure [barg]	ρ_{N_2} $[kg/m^3]$	C_ρ.
0	1.10	0.09
5	6.24	0.53
10	11.70	1.00
15	17.16	1.47
20	22.61	1.93
25	28.07	2.40
30	33.52	2.87
35	38.98	3.33
40	44.44	3.80
45	49.89	4.26
50	55.35	4.73
55	60.80	5.20
60	66.26	5.66

3.2.2.2   Experimental Procedure

All valves on the experimental setup had to be closed before filling the cell with liquid. The cell was filled with liquid by removing a nut on the cell and insert a tubing down this outlet. Valve 5 was opened and the liquid was poured down the tubing through a funnel until $3/4$ of the cell contains water. The tubing was then removed and the nut was put back on the outlet. The nut was first manually screwed in place, followed by $1/5$ of a turn with an adjustable shifting spanner. Valve 5 was then closed.

The main valve on the gas bottle was opened slowly and then turned twice to make sure it was completely open. The regulator was used to adjust the pressure of the gas. This pressure should be 5 bars higher than the desired pressure in the cell. The shut-off valve on the gas bottle could then be opened. As a precaution, the doors were closed.

If the experiments were performed with pressures higher than 0 $barg$, valve 1 was opened and the backpressure regulator (BPR) was regulated to a higher pressure value than the pressure from the gas tank. Valve 3 was then opened to the right to allow the cell to be pressurized. The cell pressure was adjusted with the BPR to the desired one. Valve 3 was then closed. The flow rate in ml/min was set with the flow controller. Valve 3 could now be opened to the left to allow the gas to enter the cell from the bottom.

The high-speed camera was turned on and placed next to the cell on a marked spot. It was connected to a computer and to a power supply. The software Photron FASTCAM Viewer 4 was used for the high-speed digital imaging. The live feed from the camera was presented by the program on the computer. The camera settings were changed in the program. This included adjustment of frames per second and shutter speed. For the tests

performed in this project, the number of frames per second was set at 500 and the shutter speed was $1/40000$. To avoid overheating the camera, the camera fan was also turned on. To be able to get an image of the bubbles with the fast shutter speed, a LED light for high-speed imaging was turned on and placed behind the cell. The live feed on the computer showed the imaging of the bubbles. To get a better focus on the bubbles, the lens on the camera was adjusted. After adjusting the focus, the calibration button on the computer was pushed to include shading. The software was used to start and stop the imaging of the bubbles and the file was saved on the computer.

If the next test was performed with a different pressure, then valve 3 was closed before adjusting the pressure on the gas tank with the regulator. The shut-off valve on the gas bottle and valve 1 could remain open. The pressure was adjusted to 5 bars higher than the desired cell pressure. The procedure that has been described above was repeated. The flow rate could be changed during the experiments by adjusting the flow controller. For low flow rates and a high cell pressure, it was necessary to start with a higher flow rate to overcome the resistance in the system before the flow rate was lowered to the wanted value.

When testing was finished, the cell needed to be depressurized and cleaned. First, valve 3 was closed and valve 7 was opened a little for 10 seconds to make sure the flow line was depressurized. To depressurize the cell, valve 3 was open to the right and the BPR and the regulator on the gas tank were regulated simultaneously until 0 $barg$ was reached. The main valve on the gas tank was then closed together with the shut-off valve and valve 1.

To remove the liquid from the cell, the nut on the outlet of the cell was removed with an adjustable shifting spanner and the tubing was inserted. A nut on the tubing was used to tighten the tubing to the outlet to make sure the system was isolated. Valve 2 was then opened to allow the flow of technical air and valve 6 was used to regulate the flow. The BPR was adjusted and valve 3 was opened to the right. A bottle was placed underneath the outlet for the liquid and valve 5 was opened downward and allowing the removal of the liquid from the cell. When all the liquid was removed from the cell, valve 5 was closed together with valve 2. The pressure in the cell was decreased by adjusting the BPR until 0 $barg$ and the tubing could then be removed. The flow rate was set to 0 ml/min with the flow controller. Valve 2 and 4 was opened and valve 3 was opened to the left, allowing technical air to flow through the red line and into the cell from the bottom. The doors on the box were then closed and the oven temperature was set to $50°$C for a duration of 2 hours so that all remaining liquid in the cell would vaporize.

3.2.2.3   Solution of Glycerol and Water

Glycerol (or glycerine) 99.5 % have been used as a viscosifier in the experiments performed with the pressurized cell due to its suitable chemical and physical properties. It is transparent, have a high viscosity and is soluble in water. Some properties of Glycerol 99.5 % are listed in Table 3.5.

Table 3.5: Some chemical and physical properties of glycerol 99.5 %.

Appearance	No colour, transparent
Relative Density	1.25 g/ml
Water Solubility	Soluble
Viscosity @T=20 ° C	810 cP

Two solutions of glycerol with a viscosity of approximately 15 and 30 cP were used in the experiments in addition to water. Figure 3.13 shows the relationship between weight percent of glycerine/glycerol and temperature and what viscosity it corresponds to. The experiments were performed with a temperature ranging from 20-30°C. Two different weight percents have been emphasized with a red box and a green box in Figure 3.13. 67 wt% glycerol corresponds to a viscosity ranging from 17.7 to 11.3 cP for the operational temperature range. This information is emphasized by the red line. 75 wt% glycerol corresponds to a viscosity ranging from 35.5 to 21.3 cP for the operational temperature range and is emphasized by the green line.

Glycerine per cent weight	Temperatur e (°C)										
	0	10	20	30	40	50	60	70	80	90	100
0 [1]	1.792	1.308	1.005	0.8007	0.6560	0.5494	0.4688	0.4061	0.3565	0.3165	0.2838
10	2.44	1.74	1.31	1.03	0.826	0.680	0.575	0.500	–	–	–
20	3.44	2.41	1.76	1.35	1.07	0.879	0.731	0.635	–	–	–
30	5.14	3.49	2.50	1.87	1.46	1.16	0.956	0.816	0.690	–	–
40	8.25	5.37	3.72	2.72	2.07	1.62	1.30	1.09	0.918	0.763	0.668
50	14.6	9.01	6.00	4.21	3.10	2.37	1.86	1.53	1.25	1.05	0.910
60	29.9	17.4	10.8	7.19	5.08	3.76	2.85	2.29	1.84	1.52	1.28
65	45.7	25.3	15.2	9.85	6.80	4.89	3.66	2.91	2.28	1.86	1.55
67	55.5	29.9	17.7	11.3	7.73	5.50	4.09	3.23	2.50	2.03	1.68
70	76	38.8	22.5	14.1	9.40	6.61	4.86	3.78	2.90	2.34	1.93
75	132	65.2	35.5	21.2	13.6	9.25	6.61	5.01	3.80	3.00	2.43
80	255	116	60.1	33.9	20.8	13.6	9.42	6.94	5.13	4.03	3.18
85	540	223	109	58	33.5	21.2	14.2	10.0	7.28	5.52	4.24
90	1310	498	219	109	60.0	35.5	22.5	15.5	11.0	7.93	6.00
91	1590	592	259	127	68.1	39.8	25.1	17.1	11.9	8.62	6.40
92	1950	729	310	147	78.3	44.8	28.0	19.0	13.1	9.46	6.82
93	2400	860	367	172	89	51.5	31.6	21.2	14.4	10.3	7.54
94	2930	1040	437	202	105	58.4	35.4	23.6	15.8	11.2	8.19
95	3690	1270	523	237	121	67.0	39.9	26.4	17.5	12.4	9.08
96	4600	1580	624	281	142	77.8	45.4	29.7	19.6	13.6	10.1
97	5770	1950	765	340	166	88.9	51.9	33.6	21.9	15.1	10.9
98	7370	2460	939	409	196	104	59.8	38.5	24.8	17.0	12.2
99	9420	3090	1150	500	235	122	69.1	43.6	27.8	19.0	13.3
100	12070	3900	1410	612	284	142	81.3	50.6	31.9	21.3	14.8

[1] Viscosity of water taken from "Properties of Ordinary Water-Substance." N.E. Dorsey, p. 184. New York (1940)

Figure 3.13: Viscosity of Aqueous Glycerine Solutions in $cP/mPas$ (Association et al., 1963).

A volume of 700 mL of solution was required in the experiments. The amount of glycerol that was required to get the desired viscosity of the solution is based on the calculations below. Equation 3.7 gives the relationship between the volume of the solution and the mass of the two components.

$$V_{total} = V_{glycerol} + V_{water} = \frac{m_{glycerol}}{\rho_{glycerol}} + \frac{m_{water}}{\rho_{water}} \qquad (3.7)$$

To get a viscosity of 15 cP, 67 wt% of glycerol was required:

Assumed m_{tot}=100 g

$$m_{glycerol} = 100g \cdot 67\% = 67g$$

$$m_{water} = 100g \cdot (100 - 67)\% = 33g$$

This corresponded to a total volume of:

$$V_{total} = \frac{67g}{1.25g/mL} + \frac{33g}{1g/mL} = 86.6mL$$

Since V_{wanted}= 700 mL, a correction factor was needed:

$$\frac{V_{wanted}}{V_{total}} = \frac{700mL}{86.6mL} = 8.083$$

This corresponds to a solution with a total wanted mass of:

$$m_{wanted} = 100g \cdot 8.083 = 808.3g$$

To get a solution with a volume of 700 mL with a weight percent of 67, the required mass of glycerol and water was:

$$m_{glycerol} = 67 \cdot 808.3 = 541.6g$$

$$m_{water} = 33 \cdot 808.3 = 266.7g$$

The same calculation was performed for the solution with a weight percent of 75. The amount of glycerol and water that was required to get a total volume of 700 mL was:

$$m_{glycerol} = 75 \cdot 823.5 = 617.7g$$

$$m_{water} = 25 \cdot 823.5 = 205.9g$$

It was important to determine the exact viscosity of the two solutions. Since the operating temperature could vary from 20 to 30 ° C, it was necessary to get a viscosity profile for this

temperature range. A rheometer was used for this purpose. A sample of each solution was put in a cup and bob measuring system. The relationship between the viscosity and the temperature is presented in Figure 3.14 and 3.15 for 67 wt % and 75 wt %, respectively.
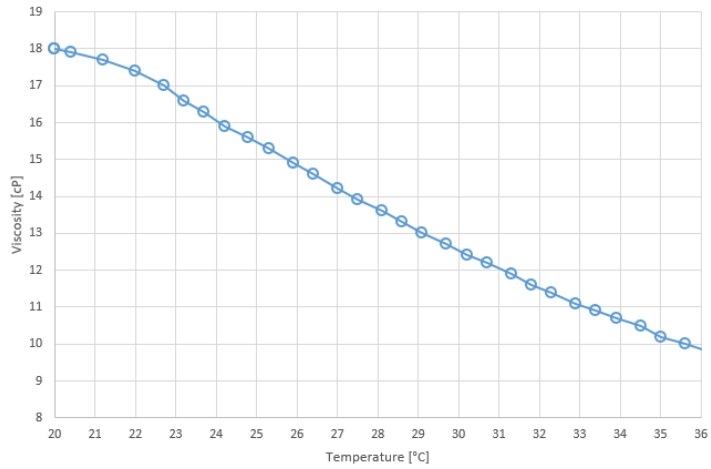

Figure 3.14: Viscosity profile as a function of temperature for glycerol-water solution with 67 wt % glycerol.
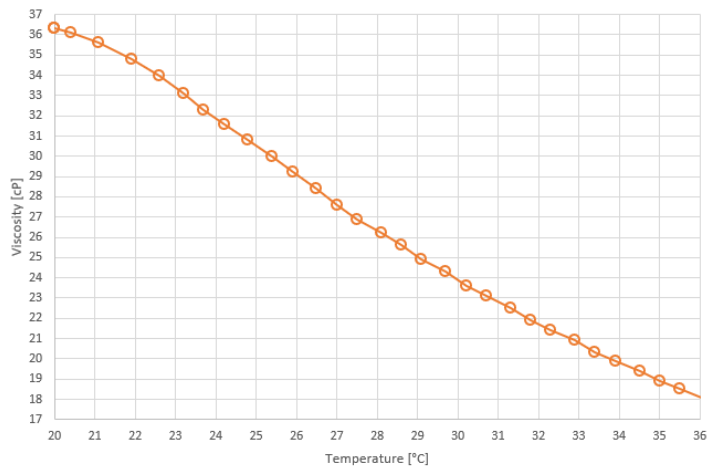

Figure 3.15: Viscosity profile as a function of temperature for glycerol-water solution with 75 wt % glycerol.

3.2.2.4   Test Conditions

The experiment has been performed for three different liquids; water, glycerol-water 67 wt% and glycerol-water 75 wt%. There is a thermometer on the oven showing the test temperature. Table 3.6 presents the properties of the test fluids, including the viscosity during the tests based on the test temperature and Figure 3.14 and 3.15. The surface tension of the viscous liquids is based on a weight percentage mix of the surface tension of distilled water and the surface tension of 100wt% glycerol at the test temperature.

Table 3.6: Properties of the test fluids

Liquid	T=test [°C]	μ_{liquid} @ T=test [cP]	ρ_{liquid} [kg/m^3]	σ_{liquid} @ T=test. [N/m]
Distilled water	30	0.79	1000	$71.2 \cdot 10^{-3}$
Glycerol-water 67 wt%	30.5	12.3	1155	$65.7 \cdot 10^{-3}$
Glycerol-water 75 wt%	32	21.5	1177	$65.1 \cdot 10^{-3}$

When the glycerol-water solutions were made, it was assumed that the test temperature would be 25°C. Since the test temperature was higher, the viscosity of the solutions was less than expected.

The experiment have been performed for two different flow rates, q_1=60 ml/min and q_2=20 ml/min, for pressures ranging from 10-60 $bara$. Since the flow controller converts mass flow to volume flow by using a constant Nitrogen density, the flow rate set on the display has been adjusted based on the information given in Table 3.4 and by using Equation 3.6. Table 3.7 shows the corrected flow rate. The results from the tests are presented and discussed in chapter 4. C_ρ is the density correction factor presented in Table 3.4.

Table 3.7: Flow rate corrected for changes in density.

Pressure [barg]	ρ_{N_2} [kg/m^3]	C_ρ	$q_{1corrected}$ [ml/min]	$q_{2corrected}$ [ml/min]
0	1.10	0.09	5.6	1.9
5	6.24	0.53	32.0	10.7
10	11.70	1.00	60.0	20.0
15	17.16	1.47	88.0	29.3
20	22.61	1.93	116.0	38.7
25	28.07	2.40	143.9	48.0
30	33.52	2.87	171.9	57.3
35	38.98	3.33	199.9	66.6
40	44.44	3.80	227.9	76.0
45	49.89	4.26	255.9	85.3
50	55.35	4.73	283.9	94.6
55	60.80	5.20	311.8	103.9
60	66.26	5.66	339.8	113.3

Table 3.8 presents what depth in the well the different operating pressures corresponds to based on the density of the different test liquids.

Table 3.8: Pressure in the cell and what depth it corresponds to in a well containing the different test liquids.

Cell Pressure [barg]	Depth [m]		
	ρ_{water}	$\rho_{\mu=12.3cP}$	$\rho_{\mu=21.5cP}$
10	101.9	88.3	86.6
15	152.9	132.4	129.9
20	203.9	176.5	173.2
25	254.8	220.6	216.5
30	305.8	264.8	259.8
35	356.8	308.9	303.1
40	407.7	353.0	346.4
45	458.7	397.2	389.7
50	509.7	441.3	433.0
55	560.7	485.4	476.3
60	611.6	529.5	519.6

The maximum operating pressure that this experiment has been performed with is 60 $barg$. This corresponds to a well depth of 611.6 m if distilled water is used as the drilling fluid. If 67wt% glycerol-water solution is used as the drilling fluid, the maximum well depth is 529.5 m. For 75wt% glycerol-water solution, the maximum well depth is 519.6 m.

According to Drilling and Solutions (2015), the average water depth for subsea wells on the NCS is 280 m. The maximum well depth according to Table 3.8 is then located 331.6 m, 249.5 m and 239.6 m below the seabed when using distilled water, 67wt% glycerol-water solution and 75wt% glycerol-water solution, respectively. This corresponds to a well depth where there could be shallow gas.

4 | Results and Discussion

4.1 Analysis of Experiments with the High-Pressure Transparent Cell

The experiments that have been performed with the high-pressure transparent cell is assumed to simulate gas migration downhole in a closed environment. 3/4 of the cell is filled with liquid and the air gap on top is pressurized. The differential pressure between the bottom and the top of the cell is minimal due to the short cell, so it is assumed that expansion of the gas bubble when migrating to the top of the cell can be neglected. The size of the bubbles can still change, but most likely due to coalescence with other bubbles.

The flow regime in the high-pressure transparent cell is a dispersed bubble flow consisting of a variation of small-sized bubbles. Related to well conditions, gas enters a well downhole through pores in the formation, so it is assumed that the flow regime in this experiment can simulate the flow regime downhole where the gas influx enters the wellbore. How the bubbles develop when they migrate ut the wellbore due to decreasing pressure have not been tested. Neither has the effect of solubility of gas into the liquid phase or flashing of gas from the liquid phase.

4.1.1 Interpretation of Images

The migration velocity of several bubbles of the same size has been monitored with frame-by-frame analysis of the images recorded during the experiments. The bubbles have been followed from the bottom of the image to the top of the image and the travel time has been determined with Equation 4.1.

$$t = \frac{f_{end} - f_{start}}{fps} \tag{4.1}$$

where, f_{end} is the frame number when the bubble has reached the top of the image, f_{start} is the frame number when the bubble enters the bottom of the image and fps is the number of frames per second, which is a camera setting.

Equation 4.2 has been used to calculate the corresponding velocity in m/s. The height of the image represents a length-interval of 4.1 cm of the cell.

$$v = \frac{0.041}{t} \tag{4.2}$$

Figure 4.1a, 4.1b, 4.1c and 4.1d is an example of a frame-by-frame analysis of a bubble travelling from the bottom of the image to the top of the image.
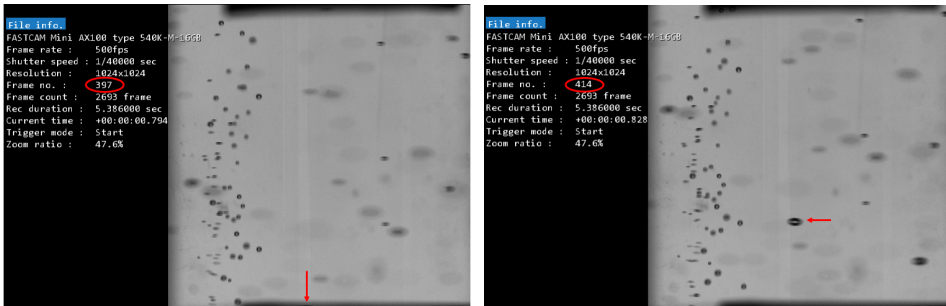
(a) A bubble enters the image at frame number 397, hence f_{start}=397.

(b) At frame number 414, the bubble has travelled 1/3 of the image.
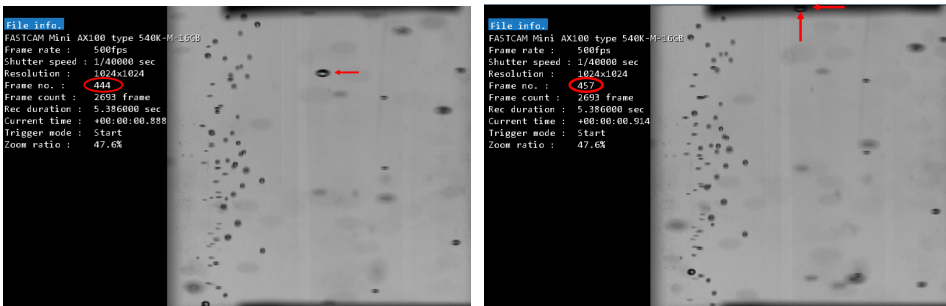
(c) At frame number 444, the bubble is getting closer to the top of the image.

(d) At frame number 457, the bubble has reached the top of the image, hence f_{end}=457.

Figure 4.1: Frame-by-frame analysis of the migration velocity of a bubble.

4.1.1.1   Limitations with Frame-by-Frame Analysis

The velocity profile of a cylinder is greater in the middle of the cross-section than near the walls. This means that the position of the bubbles that are being investigated, is of importance. The image covers the entire cross-section of the cell, so the bubbles that have been investigated have been positioned in the center or close to the center of the image. This is to minimize the variation in the velocity profile for the bubbles. It is on the other hand difficult to determine the depth location of the bubbles, which can be a source of error. The curvature of the glass and the refraction index can also influence the analysis of the bubbles and be a source of error.

4.1.2   The Effect of Initial Flow Rate on the Gas Migration Velocity

When comparing migration velocities of identical gas bubbles under the same pressure condition but with different flow rates, it is obvious that the flow rate and volume of bubbles affect the initial migration velocity. It could look like a "flying start". This means that the velocities determined with these experiments could not just be the terminal rise velocity, but could also be a function of the initial flow rate, q.

Figure 4.2a and 4.2b show two similar bubbles in distilled water for two different flow rates, 20 ml/min and 60 ml/min, respectively, and with the same pressure condition of 10 $barg$. By using frame-by-frame analysis and Equation 4.1 and 4.2, the migration velocities of these bubbles were determined. For the bubble in Figure 4.2a, the velocity was 0.197 m/s and for the bubble in Figure 4.2b, the velocity was 0.31 m/s. The only factor that has changed is the flow rate and the volume of gas entering the system, hence these factors seem to affect the migration velocity. The same tendency has been seen for bubbles of the same size migrating in the viscous liquids at different flow rates.
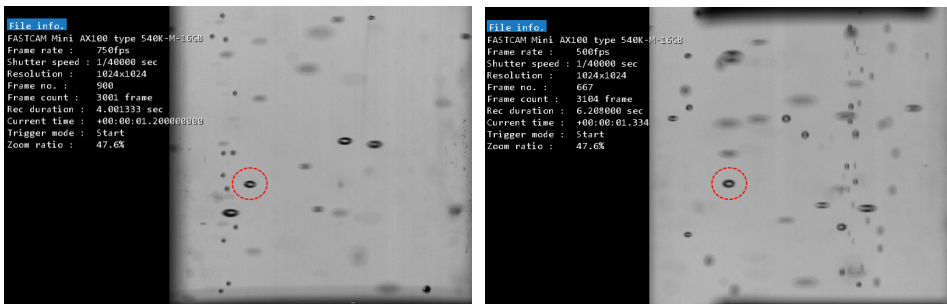
(a) Bubble with a diameter of 1.49 mm, q=20 ml/min at p=10 $barg$

(b) Bubble with a diameter of 1.49 mm, q=60 ml/min at p=10 $barg$

Figure 4.2: Two bubbles of the same size for the same pressure condition, but with two different initial flow rates.

How the flow rate affects the movement of the bubbles through the liquid is hard to determine. A higher flow rate will give an increase in the volume of gas in the system. An increase in the density of bubbles can alter the properties of the mixture.

A larger volume of gas might reduce the density in a part of the cross-section. This might cause an increase in buoyancy for the gas bubbles in this part relative to the surrounding liquid that is not in the same degree affected by the same reduction in density.

A larger flow rate of the gas can on the other hand also affect the viscosity of the mixture. If the viscosity reduces, the drag force on the gas bubble reduces, which reduces the resistance to flow and increases the gas migration rate.

A larger volume of gas in the system might also affect how the gas bubbles choose to move through the liquid. The gas bubbles tend to gather and migrate together if possible in an upward-rising channel where the velocity is higher.

The effect of migrating in a channel, reduction of viscosity in this channel, and increased buoyancy force could explain the increase in gas migration velocity.

Since the gas migration velocity for the same bubble size for two different flow rates varies with approximately 0.10 m/s, it is difficult to not include that the flow rate the gas bubbles have when they enter the system also can have an effect on the migration velocity. This means that the gas migration velocity that is determined with these experiments is a function of the terminal rise velocity of the bubbles, but also a function of the flow rate.

It is still possible to determine how the terminal rise velocity is influenced by higher pressure conditions by keeping the flow rate constant. A change in the migration velocity will then insinuate a change in the terminal rise velocity.

4.1.3   Analysis of Experiments with Distilled Water

Bubbles of the same size have been compared for the different pressure conditions at constant flow rate. The size and density of the bubbles depend on the chosen flow rate. For $q_1 = 60ml/min$, there has been a higher density of 1.86 mm bubbles for tests under the different pressure conditions compared to the tests performed with $q_2 = 20ml/min$. Bubbles with a diameter of 1.1 mm have generally been present in the tests performed with a flow rate of 20 ml/min for the pressures ranging from 25-60 $barg$.

The results from the interpretation of bubbles with size 1.86 mm for pressures ranging from 10-60 $barg$ is presented in Table 4.1 and Figure 4.3. The average velocity in m/s is presented together with the population standard deviation (SD), which is given by Equation 4.3. The velocity is based on 4-6 different bubbles from the same test. The type of trendline that best suited the results was a linear one, which is included in Figure 4.3 along with its adequate equation which is given as a function of the y-axes.

$$SD = \sqrt{\frac{1}{N} \sum_{i=1}^{N} (x_i - \bar{x})^2} \qquad (4.3)$$

where SD is given in m/s, N is the number of bubbles investigated, x_i is the gas migration velocity for a given bubble and $\bar{x}$ is the average gas migration velocity based on N.

Table 4.1: Average gas migration velocity for bubbles with a diameter of 1.86 mm for pressures ranging from 10 to 60 $barg$ for a flow rate of 60 ml/min.

Pressure [$barg$]	Average Gas Migration Velocity [m/s]	Standard Deviation [m/s]
10	0.344	0.00284
15	0.336	0.00000
20	0.332	0.00400
25	0.340	0.00472
30	0.335	0.00235
35	0.322	0.00401
40	0.287	0.00666
45	0.296	0.00573
50	0.277	0.00416
55	0.276	0.00773
60	0.269	0.00419
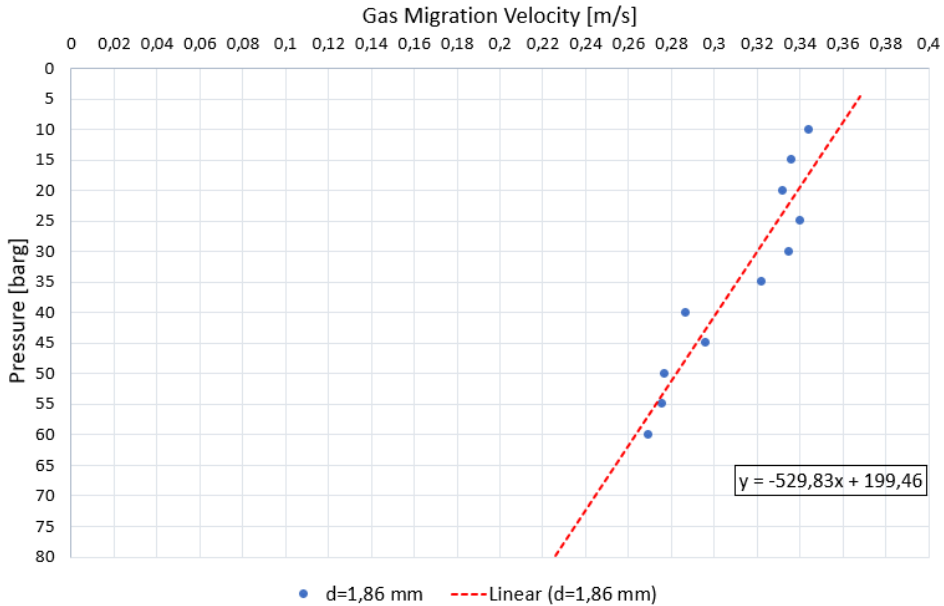
Figure 4.3: Gas migration velocity for a bubble of size 1.86 mm for experiments performed in water with constant q=60 ml/min for varying pressure regimes.

The results from the interpretation of bubbles with a diameter of 1.1 mm for a flow rate of 20 ml/min for pressures ranging from 25-60 $barg$ is presented in Table 4.2 and Figure 4.4. The type of trendline that best suited the results was a linear one, which is included in Figure 4.4 along with its adequate equation which is given as a function of the y-axes.

Table 4.2: Average gas migration velocity for bubbles with a diameter of 1.1 mm for pressures ranging from 25 to 60 $barg$ for a flow rate of 20 ml/min.

| Pressure [$barg$]	Average Gas Migration Velocity [m/s]	Standard Deviation [m/s]
25	0.291	0.00770
30	0.294	0.00170
35	0.262	0.00485
45	0.262	0.00389
55	0.264	0.00148
60	0.260	0.00827

Figure 4.4: Gas migration velocity for a bubble of size 1.1 mm for experiments performed in water with constant q=20 ml/min for varying pressure regimes.

The results presented in Figures 4.3 and 4.4 show that the gas migration velocity starts to decrease for increasing operating pressures over 30 $barg$. This result coincides with the theory presented in Section 2.4.4 by Krishna et al. (1994). Krishna et al. (1994) found that the effect of pressure on the terminal rise velocity of a bubble is neglected for gas densities over the interval of 0.1-30 kg/m^3. This corresponds to pressures ranging from 0-30 $barg$ for Nitrogen gas, see Table 3.4 in Section 3.2.2.1.

Reynolds number for the two different bubble sizes for different pressure levels have been calculated using Equation 2.7 and the gas migration velocity obtained from the experiments. Reynolds number varies from 710-562 for a bubble size of 1.86 mm for pressure conditions ranging from 0-60 $barg$. For a bubble size of 1.1 mm, Reynolds number varies

from 420-332 for pressure conditions ranging from 0-60 $barg$. For Reynolds number less than 2300, the flow is laminar (ToolBox, 2004). This means that the velocity profile is highest in the middle of the cross-section and reduces towards the edge of the cross-section .

4.1.4   Analysis of Experiments with Viscous Liquids

The bubbles are subjected to a buoyancy force, a drag force and a gravity force. Introducing a liquid with a higher viscosity than water involves a higher resistance to flow for the gas bubbles. The density of the liquid has also increased, causing a greater buoyancy force on the gas bubbles. Figure 4.5 presents the gas migration velocity for bubbles of size 1.49 mm in liquids with different viscosity from experiments performed with a constant flow rate of 20 ml/min and varying pressure regimes. The experiments performed with a constant flow rate of 60 ml/min introduced a high density of bubbles, which made the analysis more difficult. The results of the experiments with this flow rate for the viscous solution have therefore not been presented.
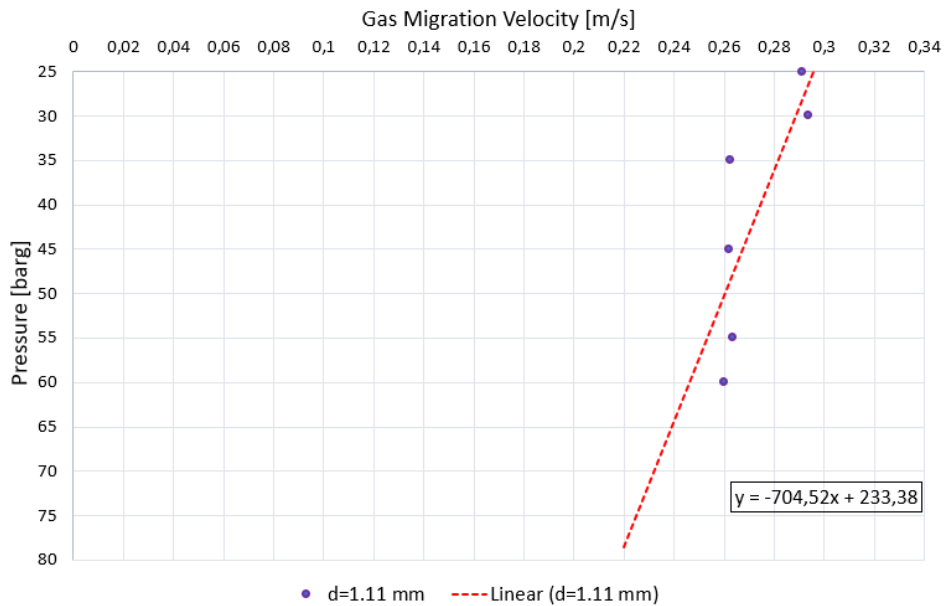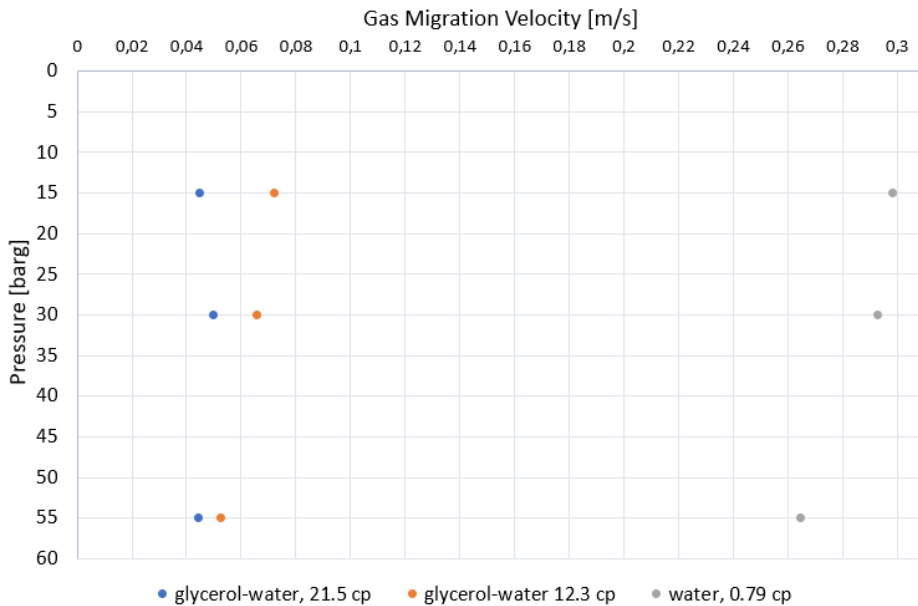

Figure 4.5: Gas migration velocity for a bubble size of 1.49 mm for experiments performed with constant q=20 ml/min for different pressures and different liquid viscosity.

As Figure 4.5 shows, the viscosity has a big impact on the rise velocity of the bubbles. The velocity is between 4-5 times higher in the experiments performed with distilled water with a viscosity of 0.79 cP for a flow rate of 20 ml/min compared to the experiments performed with a glycerol-water solution of 12.3 cP for the same flow rate. The velocity

is between 1-1.6 times higher for the glycerol-water solution with a viscosity of 12.3 cP compared to the more viscous solution of 21.5 cP for the same flow rate conditions. This indicates that even if the buoyancy force has increased due to the increase in liquid density for the glycerol-water solutions, the increased friction resistance caused by the viscosity dominates and decreases the gas migration velocity independent of the pressure level.

For the experiments with the two glycerol-water solutions, there are more factors affecting the behaviour of the bubbles compared to the experiments performed with distilled water. For most of the tests performed with the viscous liquids, a more dense bubble swarm is formed due to the reduced gas migration velocity. The location of the bubble swarm in the cross-section also affects the migration velocity. The bubbles also tend to take a more spherical shape for the experiments with the viscous solutions probably due to the increase in viscosity and change in surface tension of the liquid.

Figure 4.6a, 4.6b and 4.6c illustrate how the bubble shape and the number of bubbles change for different liquid viscosity at the same pressure and flow rate conditions.
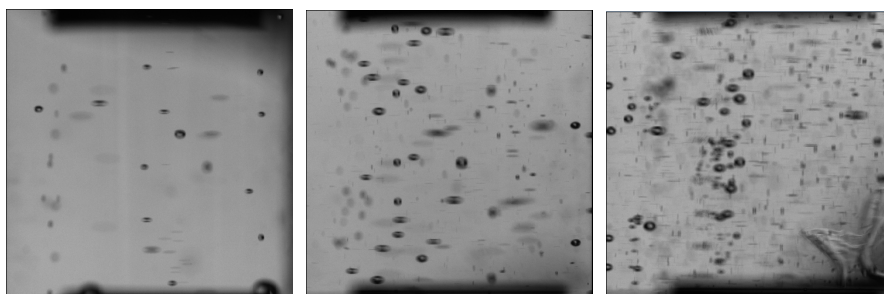
(a) Bubbles in distilled water with μ=0.79 cP, at P=55 $barg$ and q=20 ml/min.

(b) Bubbles in 67 wt% glycerol-water solution with μ=12.3 cP, at P=55 $barg$ and q=20 ml/min.

(c) Bubbles in 75 wt% glycerol-water solution μ=21.5 cP, at P=55 $barg$ and q=20 ml/min.

Figure 4.6: How bubble shape and density of bubbles change with viscosity.

Figure 4.6a shows a snapshot of bubbles migrating in water. The bubble size differs, and the density of the bubbles are less when compared to Figure 4.6b and 4.6c. For the bubbles migrating in 67 wt% glycerol-water solution at 12.3 cP, illustrated in Figure 4.6b, the bubbles tend to take a more spherical shape and the density of them have increased substantially compared to the bubbles in distilled water in Figure 4.6a. Figure 4.6c shows a snapshot of bubbles migrating in 75 wt% glycerol-water solution at 21.5 cP. The bubbles in Figure 4.6c also tend to be spherical and they are closer to each other compared to the bubbles in the 67 wt% glycerol-water solution at 12.3 cP. As Figure 4.5 showed, the gas migration velocity decreases for increasing liquid viscosity. This means that with a constant supply of gas, gas bubbles will accumulate more in the images representing a higher liquid viscosity than for lower liquid viscosity. This is primarily due to a lower migration velocity of the bubbles. This can be one of the causes why the density of bubbles increases with increasing liquid viscosity. Viscosity will influence the shape of the

bubbles by a change in the Reynolds number. A decrease in the surface tension for the viscous solutions gives an increase in Eötvös number, which also influences the shape of the bubbles, see Section 2.4.2.

There is also more background noise for the viscous solutions. When gas bubbles travel upwards, and especially if they travel close to each other in groups, they can also drag and push liquid with them in an upward channel. This could probably create a natural circulation in the y-axes of the pipe. This could simulate liquid from higher layers flowing downward to replace the liquid in lower layers, resulting in a circulation of liquid. This has been observed as small gas bubbles travelling downward in the wrong direction along the pipe wall.

It is assumed that this can be one of the causes why there seems to be a canalization of the gas bubbles in the cross-section. Most of the gas bubbles gather in an upward-rising channel. Independent gas bubbles in the outer edge of the channel are influenced by the downward circulation of liquid and seem to stand still or move very slowly downwards. The gas bubbles with the highest velocity are the ones migrating together in the upward-rising channel or gas bubble swarm. Due to the high density of gas bubbles in this area, the mix density and viscosity in this area will probably also decrease, resulting in an increased gas migration velocity for the gas bubbles travelling in the channel compared to the gas bubbles outside the channel.

The distribution of the bubble swarm in the cross-section differs for tests with different pressures. It can therefore be challenging to compare the gas migration velocity for gas bubbles flowing in a bubble swarm located at different places in the cross-section. Gas bubbles moving to close to the wall will be subjected to a wall effect, reducing the gas migration velocity.

Figure 4.7 presents snapshots of the location of the gas bubble swarm for experiments performed with 75wt% glycerol-water solution at different pressures, but for a constant gas flow rate of 20 ml/min. The bubble swarm is located to the left of the center of the cross-section for experiments with 15 and 30 $barg$, which is shown in Figure 4.7a and 4.7b. For experiments with pressures at 60 $barg$, the location of the bubble swarm tends to move towards the center of the cross-section, presented in Figure 4.7c.
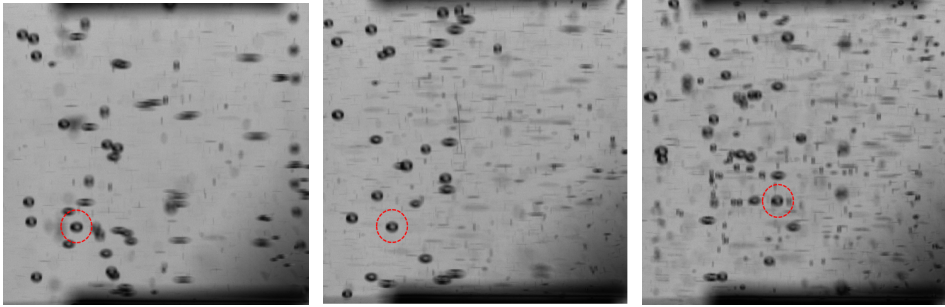
(a) Location of bubble swarm in 75 wt% glycerol-water solution with μ=21.5 cP, q=20 ml/min with p=15 $barg$.

(b) Location of bubble swarm in 75 wt% glycerol-water solution with μ=21.5 cP, q=20 ml/min with p=30 $barg$.

(c) Location of bubble swarm in 75 wt% glycerol-water solution with μ=21.5 cP, q=20 ml/min with p=60 $barg$.

Figure 4.7: Location of bubble swarm in 75 wt% glycerol-water solution with μ=21.5 cP for different cell pressures.

Table 4.3 presents the gas migration velocity for gas bubbles with a diameter of 1.49 mm for the two viscous solutions at a constant gas flow rate of 20 ml/min for different pressure regimes. Figure 4.8 illustrates the results presented in Table 4.3. The trend line that best fitted the results has been added together with the adequate equations which are given as a function of the y-axes.

Table 4.3: Average Velocity for bubbles with a diameter of 1.49 mm for pressures ranging from 10 to 60 $barg$ for a flow rate of 20 ml/min for 67 wt% glycerol-water solution with μ=12.3 cP and for 75 wt% glycerol-water solution with μ=21.5 cP.

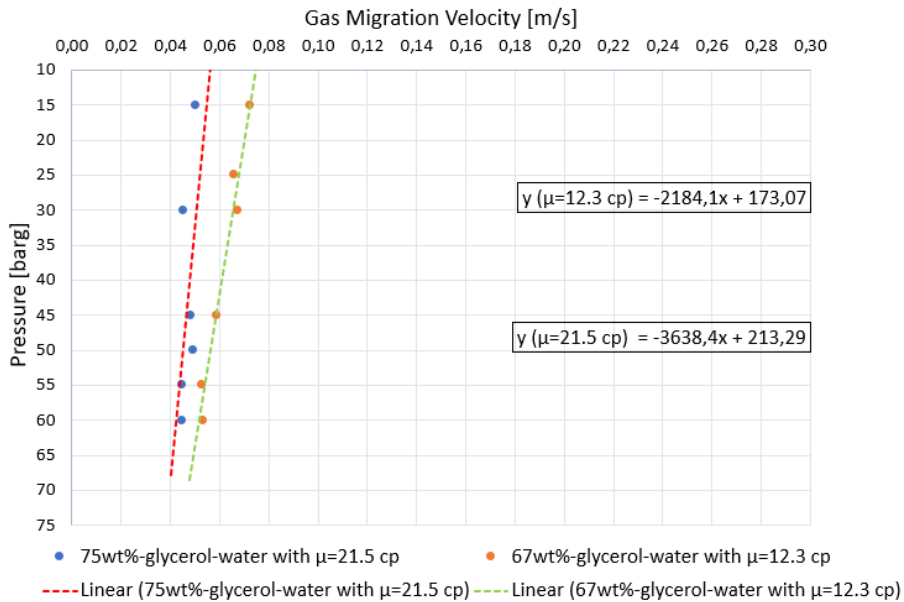| Pressure [$barg$]	v_{avg} [m/s] μ=12.3 cP	SD	v_{avg} [m/s] μ=21.5cP	SD
15	0.072	0.00259	0.045	0.00234
25	0.056	0.00229	N/A	N/A
30	0.066	0.00186	0.050	0.00299
45	0.059	0.00445	0.048	0.00161
50	N/A	N/A	0.049	0.00345
55	0.053	0.00219	0.045	0.00326
60	0.053	0.00039	0.044	0.00142

Figure 4.8: Gas migration velocity for a bubble size of 1.49 mm for glycerol-water solution with μ=12.3 cP and μ=21.5 cP for different pressure regimes at constant flow rate of 20 ml/min.

As can be seen in Figure 4.8, there are some results missing from the plot. These results have not been included due to poor experimental testing which has led to non-comparable results.

According to Figure 4.8 there is a slight decrease in gas migration velocity for increasing pressure level, but as the standard deviation in Table 4.3 presents, there are variations in the gas migration velocity for gas bubbles of the same size in the same pressure regime. The reason for this could be small differences in the interpretation of gas bubble shape or size of the investigated gas bubbles. Another cause can be the location of the investigated gas bubble in the bubble swarm in the cross-section. For the tests at higher pressure regimes, the gas bubble swarm tend to be in the middle of the cross-section, differing from the tests performed at lower pressures, where the gas bubble swarm was located in the left part of the cross-section.

Reynolds number have been calculated for a bubble size of 1.49 mm for the viscous solutions based on the gas migration velocity obtained from the experiments presented in Table 4.3 and Equation 2.7. For the 67 wt% glycerol-water solution with μ=12.3 cP, Reynolds number varies from 10-7.4 for pressure levels ranging from 0-60 $barg$. For the 75 wt% glycerol-water solution with μ=21.5 cP, Reynolds number varies from 4-3.5 for pressure levels ranging from 0-60 $barg$.

4.1.5   Discussion

According to the results presented in Section 4.1.3 and 4.1.4, the gas migration velocity of a gas bubble decrease with increasing pressures over 30 $barg$, especially for distilled water, but also slightly for the solutions with 67wt%-glycerol-water at 12.3 cP and 75wt%-glycerol-water at 21.5 cP. The gas migration velocity is considerably lower for the cases with the viscous liquids compared with the distilled water case.

The glycerol-water solutions are meant to represent drilling fluid in terms of viscosity. Both water- and oil-based drilling fluids have normally a viscosity level in the range of 10-30 cP, and have a shear-thinning effect. This means that the viscosity decreases when applied to a shear force or shear stress like during circulation of the fluid and/or rotation of the drill pipe. The cases that have been investigated in this thesis is how gas migrates in stagnant liquid for a given length-interval under pressurized conditions. This can relate to gas migration over a given length-interval downhole in a closed well without the presence of a drill pipe and without circulation.

Drilling fluid also contains weighting materials like barite and other additives, which can deviate from the glycerol-water solutions that have been used in these experiments with respect to rheology conditions and characteristics.

A limitation with the experiment performed in this thesis is the absence of a pipe, which could simulate a drill pipe. If there was a pipe present in the middle of the cross-section, the distribution of the bubble channel would probably be different. This can affect the gas migration velocity of the gas bubbles. If there was a pipe present that was rotating, it could result in a higher migration velocity due to a shear-thinning effect of the liquid and therefore an apparent reduction in viscosity.

The trend line that matched the experimental results presented in Figure 4.3, 4.4 and 4.8 were a linear one. This indicates that there is a linear relationship between pressure and the gas migration velocity. The slope of the trend line was not the same for the different cases.

Figure 4.9, 4.10 and 4.11 compares the gas migration velocity obtained from the experiment with the terminal rise velocity calculated with equations from the theory presented in Section 2.4. The equations that have been compared includes Equation 2.14, 2.16, 2.18, 2.32 and 2.36 for the three different test liquids at different pressures. The motivation for using these equations has been to compare with the experimental results, since they are referring to the same gas bubble size and flow regime.

Equation 2.14 gives the terminal rise velocity for small bubbles with Re<2. Reynolds number varies from approximately 550-720 for distilled water, 7-10 for the 67wt% glycerol-water solution at 12.3 cP and 3-4 for the 75wt% glycerol-water solution at 21.5 cP. Equation 2.14 has been used for comparison with the experiments performed with the viscous solutions.

Equation 2.16 is valid for $d_e > 1.3$ mm and low viscous liquids. The diameter of the gas bubbles investigated in this experiment have ranged from 1.1-1.86 mm for the experiments performed with distilled water. The results that are compared with Equation 2.16 in this section are for bubbles with diameter of 1.86 mm for the experiments with distilled water.

Equation 2.18 gives an expression for the terminal rise velocity for a gas bubble flow. This equation takes surface tension and all of the fluid densities into account but neglects the effect of viscosity. The terminal rise velocity obtained from Equation 2.18 was compared for the velocity obtained from the water experiments due to a higher Froude number, which gives a higher terminal rise velocity. Equation 2.36 also estimates the terminal rise velocity for a gas bubble flow, but uses a different Froude number. Since Equation 2.36 has the lowest Froude number, the terminal rise velocity calculated with this equation was used to compare to the gas migration velocity obtained from the viscous solutions.

The Fan-Tscuchiya correlation presented in Equation 2.32 includes among many factors the gas and liquid density, the liquid viscosity, surface tension and the size of the gas bubble. An example presented by Lin et al. (1998) of the terminal rise velocity calculated with Equation 2.32 for a bubble size of 1.5 mm in an experiment with a paratherm NF heat transfer liquid is presented in Figure 2.26. The velocity ranges from 0.07 m/s for 1 bara to 0.03 m/s for 194 bara at 27°C. This example using Equation 2.32 correlates well with the experimental results for the viscous liquids presented in this thesis. Equation 2.32 has been included in the comparison with the results obtained for the three test liquids.

An overview of the equations that have been compared to the migration velocity obtained from the different experiments are listed in Table 4.4.

Table 4.4: Overview of the equations presented in Section 2.4 that have been used in comparison with the results obtained from the experiments of the different test liquids

Test Liquid	Results from Experiment Compared with:				
	Eq. 2.14	Eq. 2.16	Eq.2.18	Eq. 2.36	Eq. 2.32
Distilled Water		✓	✓		✓
67wt% glycerol-water solution	✓			✓	✓
75wt% glycerol-water solution	✓			✓	✓

Figure 4.9 compares the terminal rise velocity calculated with equations presented in Table 4.4 with the results obtained from the experiments performed with distilled water.
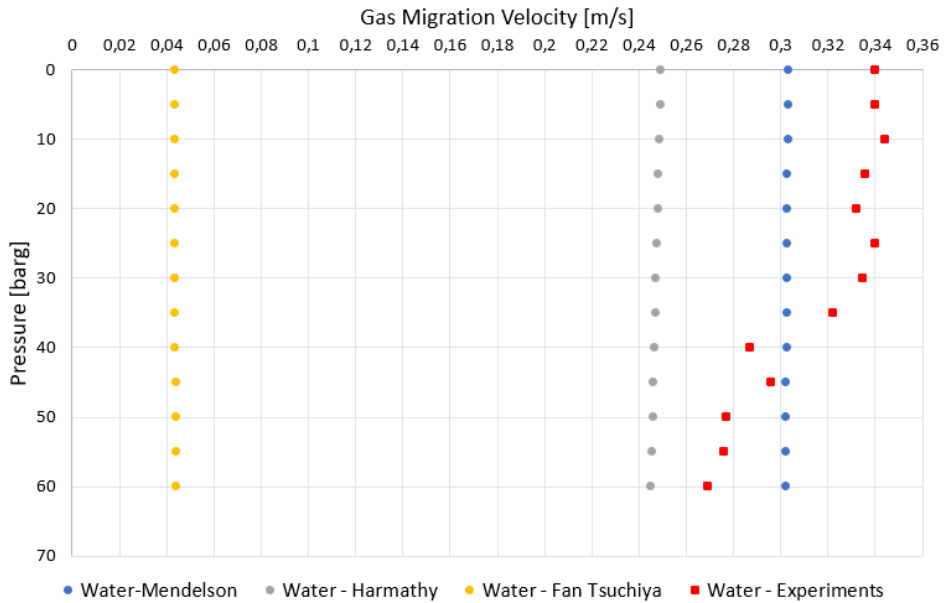
Figure 4.9: Comparison of gas migration velocity obtained from experiments with distilled water and calculated with Equation 2.16 by Mendelson, 2.18 by Harmathy and 2.32 by Fan Tsuchiya.

The experimental results show a more distinct reduction in gas migration velocity compared with the terminal rise velocity calculated using Equation 2.16, 2.18 and 2.32. The terminal rise velocity calculated with Equation 2.32 is obviously not applicable for gas migration experiments performed with distilled water. The velocity obtained from Equation 2.16 gives the closest approximation but does not correlate perfect with the experimental results.

Figure 4.10 presents the comparison of the results obtained from the experiments with the 67wt% glycerol-water solution at 12.3 cP viscosity with the terminal rise velocity calculated with equations from the theory.

Figure 4.10: Comparison of gas migration velocity obtained from experiment with 67wt% glycerol-water solution at 12.3 cP viscosity and calculated with Equation 2.14 by Stokes, 2.36 by Malnes and 2.32 by Fan Tsuchiya.

The closest approximation is the one given by Equation 2.32, but the decrease in terminal rise velocity for higher pressures has some deviations. The adjusted correlation was achieved by adding 0.024 m/s to the terminal rise velocity calculated with Equation 2.32. The terminal rise velocity calculated with Equation 2.14 and 2.36 does not correlate at all with the experimental results.

Figure 4.11 presents the results from the experiments with the 75wt% glycerol-water solution at 21.5 cP viscosity and compares it to the terminal rise velocity calculated with Equation 2.14, 2.32 and 2.36.
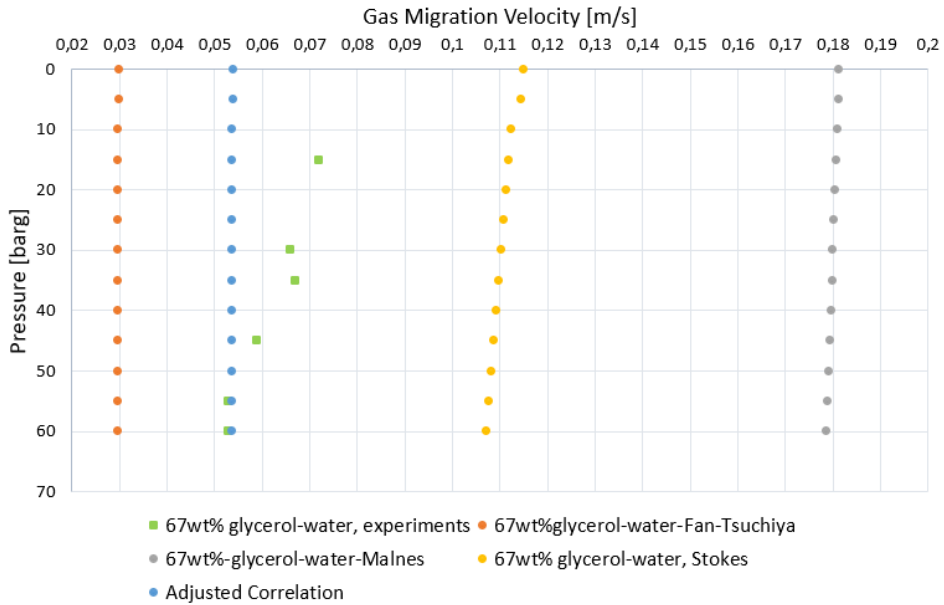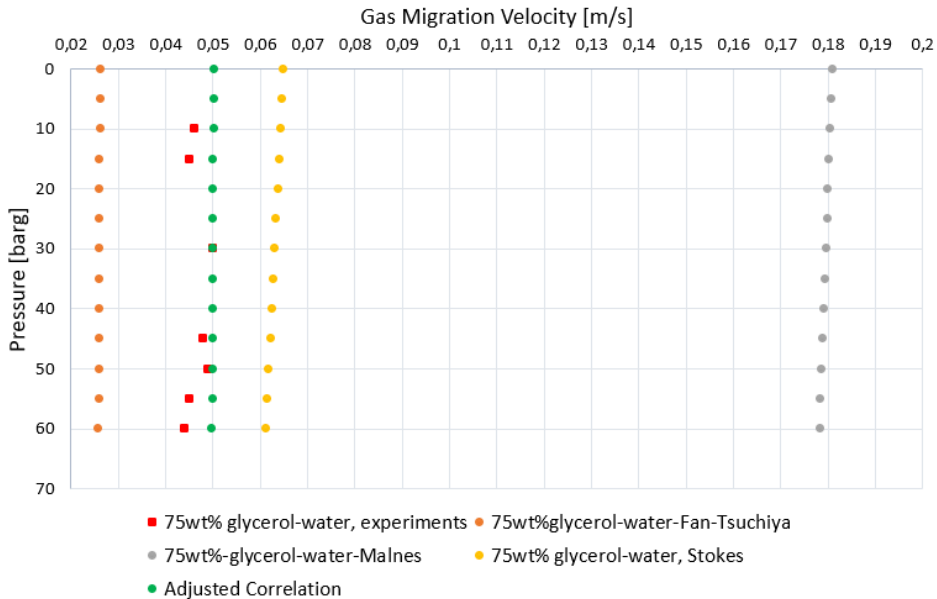
Figure 4.11: Comparison of gas migration velocity obtained from experiment and calculated with Equation 2.14, 2.36 and 2.32 for 75wt% glycerol-water solution at 21.5 cP viscosity.

The terminal rise velocity calculated with Equation 2.32 seems to correlate well with the gas migration velocity obtained from the experiments with the 75wt% glycerol-water solution at 21.5 cP viscosity as can be seen in Figure 4.11. The adjusted correlation is given by adding 0.024 m/s to the velocity value obtained from Equation 2.32 for different pressures. This correlation overlaps with the gas migration velocity from the experiment. The contribution of 0.024 m/s corresponds to 80-90% increase in velocity compared to the initial velocity calculated with Equation 2.32. The reduction in terminal rise velocity for the experiment with the 75wt% glycerol-water solution was a better correlation and more precise than it was for the 67wt% glycerol-water solution.

It was mentioned in Section 4.1.2, that the migration velocity obtained from the experiment most likely was a function of the terminal rise velocity and the initial start flow rate that the gas bubbles had when fed into the cell. It could be a probable approximation that this inlet flow rate of gas can contribute with 0.024 m/s to the gas migration velocity. Hence, Equation 2.32 could be a good estimate and approximation for the terminal rise velocity of a gas bubble travelling in viscous liquids.

4.1.5.1 Future Work

Future experiments should be performed with fluids that might simulate a drilling fluid better than the ones used in the experiments presented in this thesis. This could include adding weighting materials like barite and other additives like lubricants, solvents, dispersants or shale control inhibitors.

The experiment could also be performed with a pipe present in the cylinder cell to simulate the presence of a drill pipe. The pipe could be located at different parts of the cross-section to simulate how different locations of the drill pipe could affect the movement of the gas bubbles. If this pipe could rotate, then the effect of rotation on the gas migration velocity could be investigated.

The highest pressure regime that has been used in the experiments in this thesis corresponds to a depth of 500-600 m downhole, depending on the test liquid density. Performing tests with higher pressure regimes to simulate the situation further down in the well should be a priority for future work on this topic.

5 | Conclusion

A thorough evaluation of theory about gas migration velocity and terminal rise velocity of gas has been done as basis for the experiments performed. Industrial use and benefits of a better estimate of gas migration velocity and terminal rise velocity of gas has been discussed, especially related to CML and CMCD applications.

- The gas migration velocity is a function of the terminal rise velocity of the gas when there is no circulation in the well and the drilling fluid is stagnant. The terminal rise velocity, as presented in the reviewed literature, is a function of buoyancy, drag and gravity forces acting on the gas bubbles. Parameters that affect these forces is the density difference between the liquid and the gas, surface tension, liquid viscosity, pipe diameter and the bubble shape and size.

- The test apparatus that was intended to be used in the experiments was a high-pressure non-transparent steel cylinder tank. Observation and interpretation of the pressure response during the experiment should be used to determine the gas migration velocity. Due to limitations with the instrumental setup, the interpretation of pressure response was insufficient and inadequate, which resulted in a change of the experimental setup to a high-pressure transparent cylinder cell.

- The gas migration velocity for small dispersed gas bubbles that has been obtained from the experiments with the high-pressure transparent cylinder cell, seems to be a function of the terminal rise velocity of the gas bubbles, but also a function of the initial start flow rate of the feed into the cell with a continuous gas volume. By keeping the flow rate of gas constant, a change in gas migration velocity for higher pressure levels will insinuate a change in the terminal rise velocity.

- The experiments showed that the viscosity level of the stagnant liquid has a big impact on the terminal rise velocity of gas bubbles. An increase in liquid viscosity led to a significant reduction in gas migration velocity. For a pressure of 15 $barg$ for gas bubbles with a diameter of 1.49 mm, the gas migration velocity varied from 0.30 m/s for distilled water at 0.79 cP, down to 0.074 m/s for the 67 wt% glycerol-water solution with a viscosity of 12.3 cP and down to 0.042 m/s for the 75 wt% glycerol-water solution with a viscosity of 21.5 cP. The velocity is between 4-5 times higher in the experiments performed with distilled water compared to the 67 wt% glycerol-water solution for experiments performed with constant flow rate of 20 ml/min. This indicates clearly that the increased friction-resistance caused by the increased viscosity level dominates the other forces affecting the gas migration velocity.

- Results obtained from experiments with distilled water showed that the gas migration velocity starts to decrease for increasing pressures over approximately 30 $barg$.

The greatest reduction in gas migration velocity for increasing pressures was given for a bubble with a diameter of 1.86 mm in distilled water. The gas migration velocity was reduced from 0.34 m/s to 0.26 m/s for pressures ranging from 0-60 $barg$. There was also a slight decrease in gas migration velocity for increasing pressures for the viscous solutions as well, but not as significant as for distilled water.

- The trend line that matched the gas migration velocity obtained from the experiments for all three test liquids was a linear one. This indicates that there is a linear relationship between pressure level and the gas migration velocity. The slope of the trend line was however not the same for the different cases.

- The gas migration velocity obtained from the experiments with distilled water deviated some from the correlations from the reviewed literature. The terminal rise velocity presented by Lin et al. (1998) correlated fairly well with the gas migration velocity obtained from the experiments with the viscous liquids. By adding 0.024 m/s as a constant to the correlation, the correlation overlaps with the gas migration velocity from the experiments.

- Future recommended work on the high-pressure transparent cell includes upgrading the setup so that the experiments can be performed with higher pressure regimes. Future experiments should include test liquids with properties which are more similar to the properties of drilling fluid.

- Using instrumentation with higher measurement accuracy is recommended for the setup with the high-pressure non-transparent apparatus so that the gas migration velocity can be obtained from interpretation of the pressure response.

Bibliography

Acona, 2017. Boring i karbonatformasjoner med karst og åpne sprekker.

Alcantara Santos, O. L., et al., 2017. Technology focus: Well integrity and well control. Journal of Petroleum Technology 69 (01), 59–59.

Association, G. P., et al., 1963. Physical properties of glycerine and its solutions. Glycerine Producers' Association.

Bendiksen, K. H., 1984. An experimental investigation of the motion of long bubbles in inclined tubes. International journal of multiphase flow 10 (4), 467–483.

Bendiksen, K. H., Maines, D., Moe, R., Nuland, S., et al., 1991. The dynamic two-fluid model olga: Theory and application. SPE production engineering 6 (02), 171–180.

Bradley, N. D., Low, E., Aas, B., Rommetveit, R., Larsen, H. F., et al., 2002. Gas diffusion-its impact on a horizontal hpht well. In: SPE Annual Technical Conference and Exhibition. Society of Petroleum Engineers.

Brennen, C. E., 2005. Fundamentals of multiphase flow. Cambridge university press.

Bysveen, J., Fossli, B., Stenshorne, P. C., Skärgård, G., Hollman, L., et al., 2017. Planning of an mpd and controlled mud cap drilling cmcd operation in the barents sea using the cml technology. In: IADC/SPE Managed Pressure Drilling & Underbalanced Operations Conference & Exhibition. Society of Petroleum Engineers.

Clift, R., Grace, J. R., Weber, M. E., 2005. Bubbles, drops, and particles. Courier Corporation.

Colbert, J. W., Medley, G., et al., 2002. Light annular mudcap drilling-a well control technique for naturally fractured formations. In: SPE Annual Technical Conference and Exhibition. Society of Petroleum Engineers.

Collins, R., 1967. The effect of a containing cylindrical boundary on the velocity of a large gas bubble in a liquid. Journal of Fluid Mechanics 28 (1), 97–112.

Damon, K., Angelo, J., Park, R., 1966. A simple technique for photographing liquid drops. Chemical Engineering Science 21 (9), 813.

Darby, R., Haque, M., 1973. The dynamics of electrolytic hydrogen bubble evolution. Chemical Engineering Science 28 (5), 1129–1138.

Davies, R., Taylor, G., 1950a. The mechanics of large bubbles rising through extended liquids and through liquids in tubes. Proceedings of the Royal Society of London A: Mathematical, Physical and Engineering Sciences 200 (1062), 375–390.

Davies, R., Taylor, G. I., 1950b. The mechanics of large bubbles rising through extended liquids and through liquids in tubes. Proc. R. Soc. Lond. A 200 (1062), 375–390.

Drilling, Solutions, W., 2015. Olga-well-kill.

Dumitrescu, D. T., 1943. Strömung an einer luftblase im senkrechten rohr. ZAMM-Journal of Applied Mathematics and Mechanics/Zeitschrift für Angewandte Mathematik und Mechanik 23 (3), 139–149.

Elahifar, B., et al., 2017. Successful deep water drilling mpd, early kick detection and performing managed pressure cementing with cml controlled mud level system in gom and north sea. In: SPE/IADC Drilling Conference and Exhibition. Society of Petroleum Engineers.

Encyclopedia, o. t. E., 2019. The mechanisms of karstification.

Energy, A., 2019. Olga-well-kill.

Fan, L.-S., 1998. Gas-liquid-solid fluidization engineering.

Fossli, B., Stave, R., et al., 2014. Drilling depleted reservoirs using controlled mud level technology in mature subsea fields. In: SPE Bergen One Day Seminar. Society of Petroleum Engineers.

Godhavn, J.-M., Gaassand, S., et al., 2016. How to apply controlled mud level systems in deep water drilling. In: SPE/IADC Managed Pressure Drilling and Underbalanced Operations Conference and Exhibition. Society of Petroleum Engineers.

Goodwin, B., Nauduri, S., Medley, G., et al., 2014. Mudcap drilling: New variations, drivers, limitations, and lessons learned—case histories. In: SPE/IADC Managed Pressure Drilling & Underbalanced Operations Conference & Exhibition. Society of Petroleum Engineers.

Halle, S., 2001. Brønnkontroll for VK1 brønnteknikk. Vett viten.

Harmathy, T. Z., 1960. Velocity of large drops and bubbles in media of infinite or restricted extent. AIChE Journal 6 (2), 281–288.

Hasan, A. R., Kabir, C. S., Rahman, R., et al., 1988. Predicting liquid gradient in a pumping-well annulus. SPE Production Engineering 3 (01), 113–120.

Hauge, E., 2013. Automatic kick detection and handling in managed pressure drilling systems.

International, S., 2015. Kicks. https://petrowiki.org/Kicks.

International Association of Drilling Contractors, o., 2015. Well control procedures. In: IADC Deepwater Well Control Guidelines, 2nd Edition. International Association of Drilling Contractors (IADC), pp. 1–3.

Jeyachandra, B., Gokcal, B., Al-Sarkhi, A., Sarica, C., Sharma, A., et al., 2012. Drift-velocity closure relationships for slug two-phase high-viscosity oil flow in pipes. SPE Journal 17 (02), 593–601.

Johnson, A., White, D., et al., 1991. Gas-rise velocities during kicks. SPE drilling engineering 6 (04), 257–263.

Joseph, D. D., 2003. Rise velocity of a spherical cap bubble. Journal of Fluid Mechanics 488, 213–223.

Kataoka, I., Serizawa, A., 2010. Bubble flow. `http://www.thermopedia.com/content/8/DOI:10.1615/AtoZ.b.bubble_flow`.

Kjølaas, J., Shmueli, A., Morin, A., Belt, R., et al., 2017. Improvement of ledaflow for churn flow in vertical pipes. In: 18th International Conference on Multiphase Production Technology. BHR Group.

Koetsier, W., Van Swaaij, W., Van der Most, M., 1976. Maximum gas holdup in bubble columns. Journal of Chemical Engineering of Japan 9 (4), 332–333.

Krishna, R., 1992. Gas hold-up in a 0.63 m diameter bubble column. Tech. rep., Internal Report, Dept. of Chemical Engineering, University of Amsterdam . . . .

Krishna, R., De Swart, J. W., Hennephof, D. E., Ellenberger, J., Hoefsloot, H. C., 1994. Influence of increased gas density on hydrodynamics of bubble-column reactors. AIChE journal 40 (1), 112–119.

Krishna, R., Urseanu, M., Van Baten, J., Ellenberger, J., 1999. Rise velocity of a swarm of large gas bubbles in liquids. Chemical Engineering Science 54 (2), 171–183.

Laird, A., Chisholm, D., 1956. Pressure and forces along cylindrical bubbles in a vertical tube. Industrial & Engineering Chemistry 48 (8), 1361–1364.

Lando, J., Oakley, H., 1967. Colloid interface science. Chemical Engineering Science 25, 526–530.

Liang-Shih, F., Tsuchiya, K., 2013. Bubble wake dynamics in liquids and liquid-solid suspensions. Butterworth-Heinemann.

Lin, T.-J., Tsuchiya, K., Fan, L.-S., 1998. Bubble flow characteristics in bubble columns at elevated pressure and temperature. AIChE Journal 44 (3), 545–560.

Linga, H., Bjørkevoll, K. S., Skogestad, J. O., Saasen, A., et al., 2017. Gas influx into drilling fluids during flow check operations as affected by gas absorption characteristics of the drilling fluid. In: SPE/IADC Drilling Conference and Exhibition. Society of Petroleum Engineers.

Linga, H., Torsvik, A., Saasen, A., et al., 2016. Kick detection capability of oil-based muds in well control situations. In: SPE Bergen One Day Seminar. Society of Petroleum Engineers.

Lyons, W. C., Carter, T., Lapeyrouse, N. J., 2015. Formulas and Calculations for Drilling, Production, and Workover: All the Formulas You Need to Solve Drilling and Production Problems. Gulf Professional Publishing.

Malnes, D., 1979. Slip relations and momentum equations in two-phase flow. Institutt for Energiteknikk, Kjeller, Norway.

Maneri, C. C., 1995. New look at wave analogy for prediction of bubble terminal velocities. AIChE Journal 41 (3), 481–487.

Mendelson, H., 1967. The motion of an air bubble rising in water. AI Ch. E. Journal 13, 250.

NGU, 2015. Karbonatmineraler. https://www.ngu.no/fagomrade/karbonatmineraler.

Nicklin, D., 1962. Two-phase flow in vertical tubes, trans. Inst. Chem. Engr. 40 (1), 61–68.

O'Bryan, P., Bourgoyne Jr, A., et al., 1987. Swelling of oil-base drilling fluids due to dissolved gas. In: SPE Annual Technical Conference and Exhibition. Society of Petroleum Engineers.

Patrick Leon, O., 1985. The experimental and theoretical study of methane solubility in an oil-base drilling fluid. Ph.D. thesis, Louisiana State University, Baton Rouge.

Rader, D. W., Bourgoyne Jr, A., Ward, R., et al., 1975. Factors affecting bubble-rise velocity of gas kicks. Journal of Petroleum Technology 27 (05), 571–584.

Rygg, O., Smestad, P., Wright, J., et al., 1992. Dynamic two-phase flow simulator: a powerful tool for blowout and relief well kill analysis. In: SPE Annual Technical Conference and Exhibition. Society of Petroleum Engineers.

Shi, M., Qi, M., Yi, C., Liu, D., Zhang, K., 2017. Study on drag coefficient of rising bubble in still water. In: IOP Conference Series: Materials Science and Engineering. Vol. 231. IOP Publishing, p. 012093.

Skalle, P., Podio, A., Tronvoll, J., et al., 1991. Experimental study of gas rise velocity and its effect on bottomhole pressure in a vertical well. In: Offshore Europe. Society of Petroleum Engineers.

Skogestad, J. O., Linga, H., Bjørkevoll, K. S., Saasen, A., et al., 2017. Predicting gas loading capability in oil-based drilling fluids. In: SPE/IADC Drilling Conference and Exhibition. Society of Petroleum Engineers.

Smaaskjar, G., Bergseth, E., Hollman, L., Arseneault, L., Leggett, C., Fossli, B., Claudey, E., et al., 2018. Managing losses with controlled mud level drilling. In: IADC/SPE Asia Pacific Drilling Technology Conference and Exhibition. Society of Petroleum Engineers.

Stokes, S. G. G., et al., 1901. Mathematical and physical papers.

Sørskår, S. K., 1984. Trykk-kontroll 2 - Innstrømning og Prosedyrer for Utsirkulering. NKI-forlaget.

Talaia, M. A., 2007. Terminal velocity of a bubble rise in a liquid column. World Academy of Science, Engineering and Technology 28, 264–268.

Tangen, G. I., Smaaskjaer, G., Bergseth, E., Clark, A., Fossli, B., Claudey, E., Qiang, Z., et al., 2019. Experience from drilling a horizontal well in a naturally fractured and karstified carbonate reservoir in the barents sea using a cml mpd system. In: IADC/SPE Managed Pressure Drilling and Underbalanced Operations Conference and Exhibition. Society of Petroleum Engineers.

Tomiyama, A., 1995. Drag coefficients of bubbles (1 st report, drag coefficients of a single bubble in a stagnant liquid). Nihon Kikaigakkai Ronbunshu 61, 2357–2364.

ToolBox, T. E., 2004. Laminar, transitional or turbulent flow.

Torsvik, A., Skogestad, J. O., Linga, H., et al., 2016. Impact on oil-based drilling fluid properties from gas influx at hpht conditions. In: IADC/SPE Drilling Conference and Exhibition. Society of Petroleum Engineers.

Tung, K. W., Parlange, J.-Y., 1976. Note on the motion of long bubbles in closed tubes-influence of surface tension. Acta Mechanica 24 (3), 313–317.

Tønnessen, T. G., 2018. An experimental study of gas migration in pressurized fluids.

Viana, F., Pardo, R., Yánez, R., Trallero, J. L., Joseph, D. D., 2003. Universal correlation for the rise velocity of long gas bubbles in round pipes. Journal of Fluid Mechanics 494, 379–398.

Waldeland, J. O., 2016. Inclusion of mass transfer terms in the ausmv transient flow model. Master's thesis, University of Stavanger, Norway.

Wichterle, K., Smutná, K., Vecer, M., 2009. Shape and rising velocity of bubbles. In: 36 International Conference of SSCHE Slovikia. Vol. 90.

Wilkinson, P. M., 1991. Physical aspects and scale-up of high pressure bubble columns. Ph.D. thesis, Rijksuniversiteit Groningen.

Wilson, A., et al., 2014. Combining pressurized-mud-cap-drilling and early-kick-detection techniques. Journal of Petroleum Technology 66 (10), 145–147.

Zuber, N., Findlay, J., 1965. Average volumetric concentration in two-phase flow systems. Journal of heat transfer 87 (4), 453–468.